Distant Hemodynamic Impact of Local Geometric Alterations in the Arterial Tree

by

Yoram Richter

B.S. Physics and Computer Science
Tel Aviv University, 1997

M.Sc. Electrical Engineering and Computer Science
Massachusetts Institute of Technology, 2000

Submitted to the Harvard-MIT Division of Health Sciences and Technology
on May 14, 2003 in Partial Fulfillment of the Requirements for the Degree of

DOCTOR OF PHILOSOPHY IN
MEDICAL ENGINEERING AND MEDICAL PHYSICS
AT THE
MASSACHUSETTS INSTITUTE OF TECHNOLOGY

JUNE 2003

Signature of Author _____
Division of Health Sciences and Technology
May 14, 2003

Certified by _____
Elazer R. Edelman
Thomas D. and Virginia W. Cabot Professor
Division of Health Sciences and Technology
Thesis Supervisor

Certified by _____
Martha L. Gray
Edward Hood Taplin Professor of
Medical Engineering and Electrical Engineering
Director, Health Sciences and Technology

Distant Hemodynamic Impact of Local Geometric Alterations in the Arterial Tree

by

Yoram Richter

Submitted to the Harvard-MIT Division of Health Sciences and Technology
on May 14, 2003 in Partial Fulfillment of the Requirements for the Degree of
Doctor of Philosophy in Medical Engineering and Medical Physics

ABSTRACT

Hemodynamics has long been identified as a major factor in the determination and localization of atherosclerotic lesions. While the precise mechanism by which different hemodynamic factors act is not yet clear, the fact that they correlate highly with atherogenesis suggests that local disturbances in flow through blood vessels can promote arterial disease. These issues have become increasingly acute as physicians seek to alter the pathological arterial anatomy with bypass grafting or endovascular manipulations such as angioplasty or stenting.

We proposed that local vascular interventions might cause previously unforeseen effects elsewhere in the arterial tree. As an example of these interactions, manipulation of one branch of a bifurcation might adversely affect the contralateral branch of the bifurcation. The goal of this work was to study the distant impact of local flow alterations, as well as to classify and evaluate the different parameters that determine their severity.

Dynamic flow models of the arterial system were developed that allowed for the continuous alteration of model geometry in a controlled fashion to simulate the healthy and diseased states as well as the entire range in between. Moreover, these models permit simulation of different strategies of clinical intervention. Flow through the models was investigated using both qualitative and quantitative tools. Boundary layer separation and vascular resistance in one location of the arterial tree varied with geometrical alterations in another.

In-vivo models were developed that allowed investigation of the effect of side branch occlusion or dilation on the acute and chronic outcome of main branch stenting in a bifurcation. Chronic side branch occlusions were protective of main branch stenting as reflected by a reduction in in-stent neo-intimal hyperplasia. This protective influence was mediated by an acute modulation of monocyte adhesion and accumulation on the lateral wall of the main branch, correlating with the location of flow disturbance demonstrated by the flow models. Chronic main branch vascular remodeling plays a major role in achieving this beneficial effect.

The results of this study could have important implications for the diagnosis, treatment and long-term follow-up of the large number of patients who suffer from complex arterial diseases and undergo vascular interventions. In clinical manipulation of one arterial site one may well need to consider the hemodynamic impact on vascular segments at a distance.

Thesis Supervisor: Elazer R. Edelman
Title: Thomas D. and Virginia W. Cabot Professor, Division of Health Sciences and Technology
Thesis Committee: Elazer R. Edelman
Roger D. Kamm
Morris J. Karnovsky
Donald S. Baim

Acknowledgements

After having been accepted to graduate school at MIT I debated whether spending the next 5-7 years of my life performing research on some obscure topic that very few people would ever see and even less would understand was the best use of my time. Ultimately, someone I trusted told me that the actual research was by no means the principle reason to pursue a Ph.D. That the people I would meet, the schools of thought I would be exposed to, the methods of work and problem solving and the general atmosphere would serve me for life and would make this experience well worth the effort.

Elazer Edelman has been the embodiment of this promise. His passion for the work that he does is surpassed only by his passion for the people he works with. His unique method of problem solving forced me to continuously think 'what would Elazer do here?' in the beginning, and has hopefully been engrained in me at least to some extent towards the end. His exceptional talents as a teacher are exemplified by the unique research environment that is his lab and by the outstanding courses that he has developed. Most importantly, his devotion to his family and friends is nothing short of awe inspiring. I am truly blessed to consider myself as one of these and were it only for that, the entire experience would have been worthwhile.

The person giving the advice mentioned above was my father. As always, he was right. Thanks dad.

There is not a single achievement of mine, academic, professional, personal or otherwise that cannot be traced directly back to the confidence, the wisdom, the work ethic and the ideals instilled in me by my mother. She taught me negative numbers when I was four, and continues to teach me to this very day.

To my wife and daughter.

All I need is you.

Table of Contents

List of Figures

1. Introduction

The coupling of hemodynamic forces and atherosclerotic lesion development and progression has been examined for some time. The hallmark of atherosclerotic vascular disease, the gradual occlusion of a blood vessel's cross section, is altered flow. As atherosclerotic vascular disease is the leading cause of mortality and morbidity around the world, many have sought to understand how atherosclerotic lesions, form, grow and destabilize based on fundamental fluid dynamics. This work proposes an alternative means of analyzing the types of fluid dynamic interactions that could contribute to atherosclerotic disease.

1.1. Relationship of Atherosclerosis to Fluid Mechanics

Early workers in the field of atherosclerosis research noticed a unique phenomenon: Despite the systemic factors such as tobacco abuse, hypertension, and diabetes that place patients at risk of developing atherosclerosis, the distribution of atherosclerotic lesions is neither random nor uniform and often predictably localized to specific regions of the arterial tree[1]. Regions in and around bifurcations[2] and bends in the arterial tree have a considerably higher atherosclerotic plaque burden than other locations, even those only one or two vessel diameters away. These observations, have led to a school of thought that attributes at least part of the disease to fluid mechanic stimuli[3]. The properties of flow patterns change quite considerably over the relevant length scales. Thus, it seems appropriate to attribute the genesis and progression of disease to the interplay of forces and flows between the blood flowing in the arteries and the arterial wall.

Whatever the flow pattern in the vessel is, the actual transduction of force to the vessel wall is through the shear stress, the force per unit area exerted by the fluid on the vessel wall. It is thus reasonable to define potentially deleterious flow patterns as those that produce abnormalities in shear stress[4]. The importance of shear stress is further reinforced by the concentration of atherosclerotic plaque in regions of the vascular bed that have abnormally high and low shear stress[5], e.g. bifurcations[6,7].

Several characteristics of flow have been proposed over the years as a stimulus for the development of atherosclerotic disease[8]. It was initially proposed that abnormally high

shear stress may cause disruption damage and denudation of the endothelial cell layer[1,9]. Flow-mediated endothelial dysfunction is a primary factor in the initiation and propagation of atherosclerotic lesions[10-12]. Yet, examination of the bifurcations themselves showed that the 'high shear stress' theory was unlikely. Bifurcations possess regions of abnormally low and high shear stress, the highest values being found around the flow divider region. However, it is the high shear regions of bifurcations that are typically spared of the common elements of atherosclerosis including lipid deposits, inflammatory cells, fibrosis, etc.

Thus, rather than a specific shear event, turbulent flow patterns[13-15] were thought to explain the observed localization of lesions, through damage to the endothelium as well, and deposition of different blood-borne products onto the vessel wall. The difficulty is that it is rare to encounter conditions under which laminar flow becomes turbulent within the arterial bed. Arterial flow rates do vary but in general the Reynolds numbers[i], are well below the upper critical value at which laminar flow can be expected to turn turbulent, and are typically less than the lower critical Reynolds number at which turbulence is expected to die out and revert to laminar flow. Thus, while turbulence might exist at very specialized locations, for example immediately downstream from heart valves and in some locations in the ventricles, as a general rule turbulence would not be expected to prevail in the arterial bed, and certainly not to the extent that would explain the wide distribution of atherosclerotic disease[16].

Given these facts, the focus has shifted from high shear regions to low shear regions[17-19]. Low shear can abrade the endothelium and directly affects gene expression patterns and the function of endothelial cells[20,21]. A bifurcation can exhibit several regions of lower shear stress. Most prominent of these are the two regions of boundary layer separation that exist in the lateral angles of the bifurcation[22]. Stretching from stagnation point to point of reattachment, these two areas are ones in which the shear stress is abnormally low throughout. This has led several workers to suggest a direct link between localization of atherosclerosis and regions of boundary layer separation[23]. Other features of the flow in separated regions have also been proposed as possible promoters for

---

[i] See subsequent discussion of dimensionless parameters.

atherogenesis, these include both reverse and pulsatile (non-uniform) shear stress and have been shown to correlate with the localization of atherosclerotic plaques in vivo[24]. The importance of low shear stress is consistent with the evolving view of atherosclerosis as an inflammatory process[25], wherein the progression of atherosclerosis is governed by a series of reactions between the vessel wall and a multitude of blood-borne inflammatory cells, particles and proteins. The characterization of these reactions and the factors that determine their progression is a complex science. However, one must keep in mind that the interaction of the inflammatory cells with the vessel wall does not happen in a vacuum. Rather, throughout these events the inflammatory cells and the vessel wall itself are subject to dynamic forces that are dependent on arterial architecture and blood flow. These forces will determine to a large extent the state of the endothelial lining to which the inflammatory cells must adhere and through which they must traverse[26].

This view well relates fluid mechanical phenomena, particularly low shear stress and boundary layer separation, to atherogenesis and the progression of atherosclerotic disease. The process of inflammatory cell penetration of the endothelial cell layer is not instantaneous. Rather, it is a gradual, multi-stage process that takes place over numerous cycles of flow. Throughout this process, cells are subject to forces exerted on them by the vessel wall, adjacent cells and flowing blood. Cell adhesion to the vessel surface is initially passive and weak. Thus, cell binding and penetration through the vessel wall is governed by the balance of forces that enhance cell adhesion with those forces that tear cells away. These latter forces, which retard penetration of the vessel wall, are no more than an expression of the shear stress, and as such are reduced in regions where shear stress is abnormally low. Furthermore, regions of boundary layer separation, which include re-circulating and sluggish flows, would increase residence times for the inflammatory agents near the vessel wall. As residence time increases more time is provided for the reactions to occur and to progress to an active, migratory nature.

Other more detailed models of the interactions of flow with the arterial wall have focused on oscillatory, bi-directional and spatially and temporally alternating flow patterns[24]. One could easily link atherogenesis with any altered flow pattern. Endothelial cells have been shown to adapt to the local flow conditions they encounter. One example of this type of adaptation is the morphologic appearance of these cells[27]. Cells that are subject to

high, yet physiologic, flows tend to have an elongated appearance when viewed *en-face*, with the long axis oriented along the direction of flow. Conversely, cells that are subjected to more static conditions tend to be more rounded[27]. In a system as intricately evolved as this, it seems reasonable to assume that endothelial cells are specifically suited to whatever the flow conditions at their location happen to be. Assuming this to be the case, one would expect that any alteration in the flow pattern cells normally experience and to which they are conditioned, be it direction, velocity, or shear stress would have a negative effect on endothelial cell function.

Whatever the mechanism of action, one cannot ignore the simple phenomenological correlation between regions of boundary layer separation and development of atherosclerotic disease. Some studies[28] have extended the one-to-one correlation in the localization of these two factors, to a striking resemblance in the physical shape of the region of separation and the subsequent atherosclerotic lesion that develops. This resemblance is so extensive, especially around bends and bifurcations, that one is led to think of mechanisms whereby boundary layer separation triggers atherogenesis, and the lesion develops until it fills the entire original space taken up by the separated flow. It is these observations that prompted us to focus on boundary layer separation as a primary stimulus effecting neo-intimal hyperplasia. Rather than track a virtually limitless number of possible parameters; in the remainder of this work we assume that processes that tend to reduce the extent of boundary layer separation are beneficial, whereas ones that tend to enlarge it are deleterious in their effect.

1.2. Modalities of Treatment

The end result of the long course of vascular disease will in most cases be luminal occlusions that jeopardize organ perfusion to such an extent as to necessitate corrective or bypass procedures. It is worthwhile noting that these luminal occlusions need not be complete, or nearly complete, to exert a significant effect on the organ perfused by the effected artery. One explanation for this fact lies in an appreciation of the fluid mechanic principles involved. As will be discussed later, the resistance to flow of an arterial

segment[ii] is under ideal situations inversely related to the fourth power of the diameter of the segment. Thus, even a modest decrease in diameter can have a drastic effect on the resistance to flow of the artery, and hence the amount of blood which it delivers. A second explanation has to do with the morphology and natural history of atherosclerotic lesions. Some lesions may, at certain points become unstable and rupture, exposing cells and tissues and releasing agents to the circulation with dramatic effects. There is evidence that the unstable lesions that rupture are less likely to be the ones that present a substantial luminal occlusion or reduction in cross-sectional area.

Corrective procedures might take many forms. Bypass grafting, creates an alternative flow channel[iii] that diverts flow from a point upstream or proximal to the lesion to a point on the vessel that is downstream or distal to the lesion. During angioplasty, the lesion of interest in acted upon directly and the artery is dilated to approximate its original dimensions in an attempt to restore flow downstream. Today both of these classes of procedures can be performed minimally invasively and even percutaneously, hence the term Percutaneous Transluminal Angioplasty (PTA).

The long term efficacy and benefit of these procedures is a topic of intense investigation and debate. The relative advantages and disadvantages of one procedure over the other are of tremendous clinical importance but also in many cases unclear. Regardless, the most common mode of failure of these two treatment modalities is similar – accelerated occlusion of the new flow channel. In the case of bypass grafting this is commonly referred to as graft occlusion, whereas in the case of angioplasty this is known as restenosis. Both of these modes of failure are mediated by a complex, multi-stage cellular process called intimal hyperplasia. Briefly, arterial injury leads to endothelial disruption and dysfunction. The altered luminal surface promotes platelet adhesion and activation which leads to initial thrombosis. Immediately following this, leukocyte adhesion, accumulation and transmigration occurs in several waves (first polymorphonuclear cells

---

[ii] The resistance to flow is inversely related to the amount of flow going through the segment in a parallel circuit such as the arterial tree.

[iii] The sources for this channel are numerous and include the saphenous vein from the leg, the radial artery from the arm and the internal mammary artery from the chest, as well as research efforts into artificial sources.

and then monocyte/macrophages). Ultimately, this inflammatory cascade promotes smooth muscle cell migration and proliferation in the intimal layer which leads to re-occlusion of varying parts of the luminal cross-section.

1.3. Prior Work

A large body of experimental evidence has been assembled regarding the flow in different parts of the arterial tree and especially that which exists in and around arterial bifurcations[29]. This prior work includes analytical analysis, modeling by use of mock circulation systems as well as numerical analysis. Each one of these approaches has its advantages and its limitations:

Analytical work is the most precise and can give perhaps the most insight and intuition into a problem. Unfortunately, the full Navier-Stokes equation that governs flow in the relevant regime of intermediate Reynolds numbers is complex and can only be solved analytically for a handful of highly simplified geometries. This leaves the latter two methods – numerical analysis and physical modeling. Of these two, numerical analysis is clearly the more flexible as it allows for changing of the parameters that characterize the problem repeatedly, incrementally and virtually instantly. However, numerical analysis is of lesser accuracy at the singular points of flow unsteadiness and separation[30]. Since these are the points at which the phenomena of interest here occur, this presents a limitation to the applicability of the results. Additionally, the proper characterization and implementation of an accurate numerical model is highly complex and would constitute an entire project in and of itself beyond the scope of what is practical in this particular work that seeks to combine several other aspects including the biological response.

Physical modeling has been used for years precisely in cases where numerical analysis is restricted. Physical modeling is a highly refined method dating back at least 1872 when William Froude built the first towing tank to test the resistance of ocean vessels. Such modeling however is not without its own limitations; the major ones being the fact that it is inherently inflexible, the relative difficulty associated with altering the parameters modeled and the inherent inaccuracies stemming from physical limitations of the modeling apparatus.

Analytical[31], numerical[30,32-34] and physical modeling[28,35-38] methods have all been employed for the analysis of flows and lesion localization in arterial bifurcations. Typical sites examined have included bifurcation of the aorta and left main coronary[32], carotid [37], and pulmonary [39] arteries. Experiments typically map different flow parameters in the region such as flow vectors, pressure gradients, shear rates and shear stresses along the artery wall as well as others. While extensive, these models all share several common characteristics, and as a result a shared set of limitations.

Past models have all been similar in that they:

a) Usually simulate conditions in healthy arteries, that is, before lesions have actually formed[32].
b) Have attempted to re-create a specific arterial geometry faithfully and with a high level of detail[36]. To mimic the specific case in question input flow parameters, such as flow rate and pressure profile, and the physical properties of the model, e.g. relative diameters, bifurcation angles, wall motion, etc. are determined as precisely as possible[28,30,36,40].
c) Concentrate on what has been perceived as the "causal" effects, i.e. the effects distal to the site of intervention in one specific vessel.
d) Are "static", modeling the system at one point in time, and do not allow for the long term remodeling of the system that occurs in the natural case[35].

These common features also provide a set of respective limitations to their applicability:

a) While providing valuable insight into the process of atherogenesis, and helping to explain areas of high risk, clinical applicability and treatment inferences are limited. High-risk areas may be identified but clinical intervention in healthy arteries, before significant lesions have occurred, is unlikely.
b) Since each actual clinical case is unique, the applicability of a highly specialized model is severely limited[29]. That is to say that the chances in any one clinical setting that the geometrical attributes of a patient's disease will coincide with a case which has been modeled are extremely remote. For this reason, the knowledge gained has had a limited effect on the practices of clinicians presented with a wide range of specialized cases but no concise set of general guidelines. Furthermore, the attempt to provide a precise description to highly specialized case may very well obscure

more generalized insights into the inherent nature of the interaction between vascular repair and fluid dynamics.

c) Models that examine only down-stream vessels ignore the potential impact on the larger and possibly more clinically important proximal vessels.

d) Static systems ignore the long-term dynamic nature of the arterial system, which enables it to respond to ever changing conditions by continuously re-modeling itself.

Significant work has gone into describing the formation and characteristics of lesions in animal models. This includes both the formation of lesions *de-novo* and as a response to vascular interventions such as stenting – the so called process of 'restenosis'. Some of this work has sought to correlate between these *in-vivo* lesions and geometrical and/or flow patterns. Most of this work, however, has been associative in nature i.e. showing a retrospective correlation between *in-vivo* neo-intimal hyperplasia and the physical conditions that existed in the vessel. Despite the success of these types of associations, few if any workers have attempted to make *a-priori* predictions based on flow patterns and then to verify these in an *in-vivo* model. As discussed later, the difficulty in making these predictions is due to the inherent difficulties in translating flow-based bench-top data to *in-vivo* end organ effects, because of a multitude of factors, including:

a) Uncertainty surrounding the relative role of flow pattern within the numerous other factors that affect *in-vivo* results.

b) Difficulty in accurately modeling a specific *in-vivo* geometry accurately and/or in predicting the effect of deviations from the prototype.

c) Difficulty in precisely describing the three dimensional geometry of an *in-vivo* or *ex-vivo* lesion.

1.4. Time Course of Disease and Response to Treatment

It is important to appreciate the time course of the different processes involved in atherosclerotic disease. The progression of the disease itself is quite slow. Precursors of atherosclerotic lesions can readily be identified in healthy individuals in their early twenties. Observations have been made of fatty streaks, the earliest form of atherosclerotic lesions, in children as young as two to four years of age. However,

normal adults[iv] do not typically become symptomatic until their mid to late fifties[v]. The natural progression of atherosclerotic lesions is a slow and gradual one, taking anywhere from thirty to fifty years and perhaps even longer to develop.

The changes in the arterial wall imposed by bypass or angioplasty are entirely different however. These changes take place over the course of what amounts to minutes to hours. The response of the tissue to these rapid changes can be expected to vary greatly from that to the disease itself. A system that has been designed to deal with events that occur over the course of many years in an optimal manner can be expected to react in a sub-optimal and perhaps even deleterious manner to changes on this vastly shorter time scale[41]. As an example, while the geometry of a vessel prior to the initiation of atherogenesis can be vastly different from the geometry after a fully developed atherosclerotic lesion is present, the incremental changes in geometry are small. Thus the artery is always in a 'quasi-steady' state and the biological response is controlled and slow. On the other hand, the incremental change imposed by vascular intervention over the course of seconds can be much larger. Within seconds the vessel geometry changes by the same amount as it normally would over decades. Because of this rapid change, the biological system is thrust far away from its equilibrium point and as a result responds in a sub-optimal manner, manifest as the rapid progression of restenosis.

1.5. Interactions Between Different Sites in the Arterial Tree

In the clinical setting, lesions in individual arteries have typically been treated as separate and independent events. While the presence of lesions in multiple sites is certainly an indication for choosing one type of treatment modality over another, the continued progression of lesions in segments that were not manipulated has not been attributed to interactions between these sites, but rather to the underlying systemic disease manifesting itself in several locations. Similarly, the occurrence of lesions, either *de-novo* or as a progression of prior ones, over time has typically not been attributed to a causal

---

[iv] By normal here we mean ones that do not suffer from diabetes mellitus or any other form of genetic or environmentally caused disease that predisposes them to accelerated atherosclerosis at a young age.

[v] The average age for presentation with a myocardial infraction is 58.5 in men and 64.5 years in women.

relationship between them or to a result of an intervention but rather further symptoms of an already established disease.

Consequently, the treatment of lesions has been on an individual basis with little regard to the effects that treatment of one site might have on another. Furthermore, the long-term follow-up of patients who were treated with one form of intervention or another has focused on the site at which the intervention was performed. A demonstration of this point is the fact that one of the most common criteria for the evaluation of efficacy of a treatment modality over time is the rate of "target lesion revascularization".

The basis of this thesis is the assertion that this view is an oversimplification of the problem. The reasons for this assertion can be broken down into three main factors:

1. We first examine a vastly oversimplified analogy for a fluid flow circuit – that of a completely passive electrical circuit (fig. 1-01).

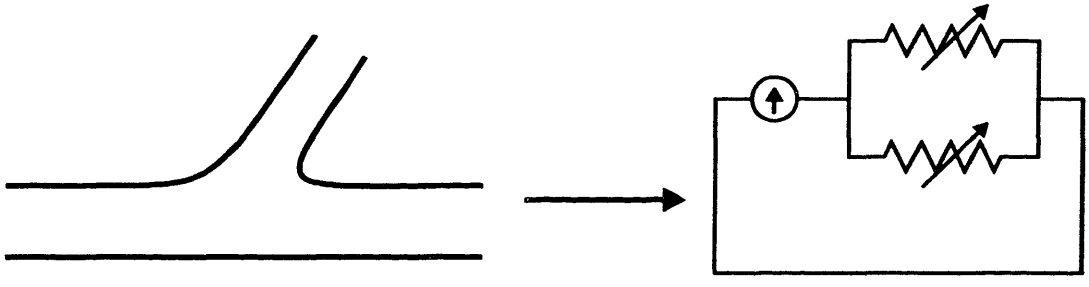

Figure 1-01: Simple Electric Analogy for Flow Bifurcation. The input to the bifurcation can be modeled as a current source. Varying the resistances simulates occlusions in one of the two vessels.

In this analogy, a lesion in a branch is simulated by raising the resistance of the appropriate resistor. Re-adjusting the value of the resistance down towards its original value simulates dilation of this lesion. Clearly, any change in the resistance on one branch will have an effect on not only the flow in that branch but also on the flow through the contra-lateral one.

2. In the case given above, each flow branch is modeled by an entirely passive circuit element. In reality, the case is much more complex: Each vessel segment posses a fluid dynamic impedance, which is a generalized dynamic resistance taking into account the compliance of the vessel, the inertia of the fluid and the frequency of oscillations. This impedance is different from the circuit above in that while electrical resistors have a set

impedance regardless of the circuit they are placed in, the impedance of a vessel is dependant on the flow patterns it is subjected to. Any change in one part of such a circuit will necessarily effect a change in the flow patterns through other parts of the circuit and hence change the impedance of these other channels thus altering the flow patterns further. In this manner, a complex interaction is set up between any part of the flow circuit and all other parts.

3. Real arteries are composed of living tissue and are not simply solid tubes. They have the capacity to adapt and react to changing flow conditions. It is the assumption of this work that under normal conditions, these adaptations optimize the entire flow system from the perspective of some crucial parameter such as energy consumption or tissue perfusion. Under abnormal conditions there could be a derailment of these adaptive mechanisms and adverse results.

Regardless of what guides these adaptations, the end result is that intervention on one site might under certain conditions set off a host of adaptive responses in other sites. As the effects are fluid dynamic, the impact may be observed downstream from the site of intervention, upstream from it, or in a parallel flow channel. Some of these interventions might trigger a problem of considerably larger implications than that which they attempted to solve, for example if an intervention in one site has an adverse effect on a more proximal vessel. In other, less extreme cases, the type of intervention and the manner in which it is performed would surely benefit from a more complete understanding of the interactive processes involved so as to produce a more favorable long term result.

1.6. Experimental Scenario

To demonstrate this approach, a specific clinical scenario was outlined to simulate the progression of disease, the clinical intervention performed and the possible long-term outcomes. It is crucial to note that this scenario in no way attempts to model the most prevalent clinical situation. Nor does it attempt to model precisely any specific type of intervention. In fact, no attempt has been made to accurately model any real-world situation at all. The sole purpose of the scenario is to provide a framework through which the range of different types of interactions discussed can be examined individually

and their impact precisely analyzed and rigorously demonstrated. This scenario is the backbone of the set of experiments performed in this thesis:

1.6.1. Basic Bifurcation Geometry

The basic geometry of a bifurcation includes an inherent fluid mechanics problem. On a theoretical basis alone one would expect two regions of boundary layer separation to form (see fig. 1-02). The first region forms in the ostium of the side branch. Intuitively, this would seem to be the result of inertia. That is to say that the blood flowing down the main branch simply cannot negotiate the sharp bend on the lateral wall of the bifurcation. The second region of separation forms in the main branch facing the ostium of the side branch. This can be understood in several ways: One is to think of it as a result of the take-off of blood into the side branch that diverts all streamlines away from the wall. This is however somewhat misleading as it predicts that at a zero degree angle of bifurcation – the case in which one channel simply divides into two parallel channels – one would not see this region of separated flow – a result that is false[31]. A more rigorous treatment shows that both regions of boundary layer separation are in fact due to the same cause – flow against an adverse pressure gradient[42]. In the case of an arterial bifurcation, the adverse pressure gradient is due to two factors:

1. The total cross sectional area increases at an arterial bifurcation (by an average factor of 1.4:1) and thus the mean rate of flow must decrease. As the rate of flow decreases, the pressure increases (by Bernoulli) thus creating an adverse pressure gradient.
2. Irrespective (and even in the absence of) the increase in total cross sectional area, an adverse pressure gradient is created by the imposition of a new boundary layer – that which forms along the flow divider.

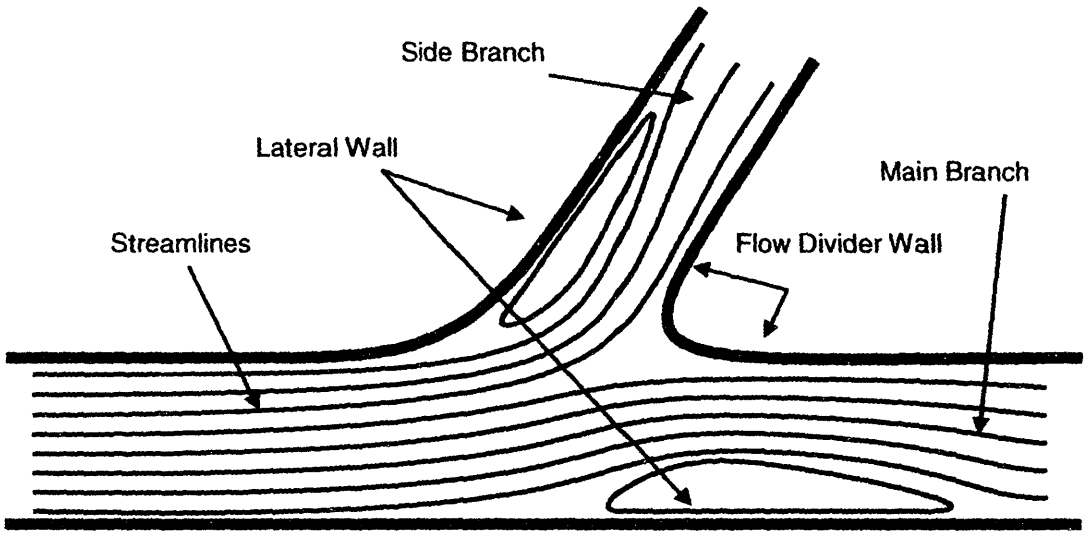

Figure 1-02: Flow Through a Simple Bifurcation. Figure depicts predicted flow through a simple idealized bifurcation prior to any optimization. Note the regions of boundary layer separation on the lateral walls of both the main branch and the side branch.

1.6.2. Tapered Bifurcation

In reality, major bifurcations[vi] do not normally appear as in fig. 1-02. Rather, most bifurcations include a tapering of the lateral wall of the mother branch from approximately the point that faces the ostium of the daughter branch. This is demonstrated in fig. 1-03.

[vi] The term "major" refers to those bifurcations where the diameter of the daughter branch is not insignificant with respect to the diameter of the mother branch.

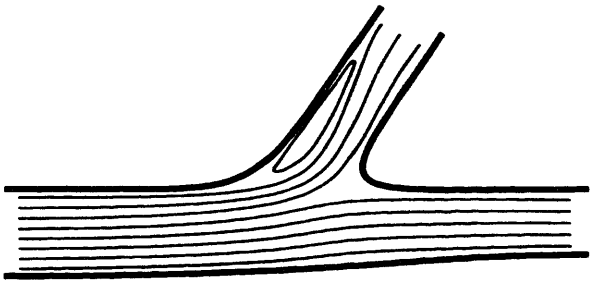

Figure 1-03: Flow Through a Tapering Bifurcation. Predicted flow through a bifurcation that has been 'optimized' by tapering the distal main branch. The angle of tapering has been exaggerated here for demonstration purposes. Note the reduction/disappearance of the boundary layer separation in the main branch.

One possible explanation for the benefit of this geometry is that by approximating the curvature of the streamlines with the vessel wall itself, the artery reduces or perhaps eliminates the region of boundary layer separation in the main branch. This is just one example of optimization of arterial geometry from the point of view of minimization of flow disturbance. Note however that the region of separation in the side branch still exists. Indeed, approximating the streamlines with the vessel wall at this point would severely reduce the diameter of the side branch. In fact, this region of disturbance in the side branch is where many of the initial lesions in bifurcations actually occur.

1.6.3. Lesion in the Side Branch

Boundary layer separation in the ostium of the side branch will in many cases lead to the formation of an atherosclerotic lesion. Because the progression of disease is very gradual, the system has time to react adaptively to the slow occlusion of the side branch. This can be done in a number of ways including alterations in the downstream resistance i.e. the vascular bed, development of collateral circulation (see fig. 1-04) as well as shifting of the input flow patterns to the system itself (by shunting flow away from other sites for example). Whatever these adaptations turn out to be, the original cause of boundary layer separation in the mother vessel, take-off of flow at the bifurcation, is greatly reduced or perhaps even no longer exists. The tapering of the mother vessel now serves no advantageous role and is actually detrimental as it needlessly increases the resistance to flow of the mother branch. It is reasonable to assume then that the system

will adapt in such a way as to eliminate this tapering. The precise mechanism for this adaptive remodeling can come from a number of stimuli. For example, previous work[43] has shown that an increase in shear stress, such as would be expected to occur in the main branch as a result of side branch occlusion, induces an outward remodeling of the vessel until shear stress values return to baseline.

Figure 1-04: Flow Through a Bifurcation with a Lesion in the Side Branch. Note the development of collateral circulation. Note also the remodeling of the main branch relative to fig. 1-03.

It is important to note that in this new configuration boundary layer separation in the main branch is minimal (perhaps even eliminated), despite the absence of taper. There is of course still a perfusion problem to the region that was served by the daughter vessel.

1.6.4. Dilation of the Side Branch

The assumption made when dilating a lesion is that one is returning the system to its original configuration. If however we take into account the fact that the system has adapted to the changing conditions over the course of the disease as it has here, it becomes clear that by dilating the lesion one actually creates a completely new configuration. In this new configuration, the other parts of the system are no longer optimized for the conditions with which they are presented and one possible manifestation of this could be the re-establishment of a region of boundary layer separation in the main branch (fig. 1-05). In other words, restoration of the original anatomy or vascular architecture may not restore the initial or optimal flow conditions.

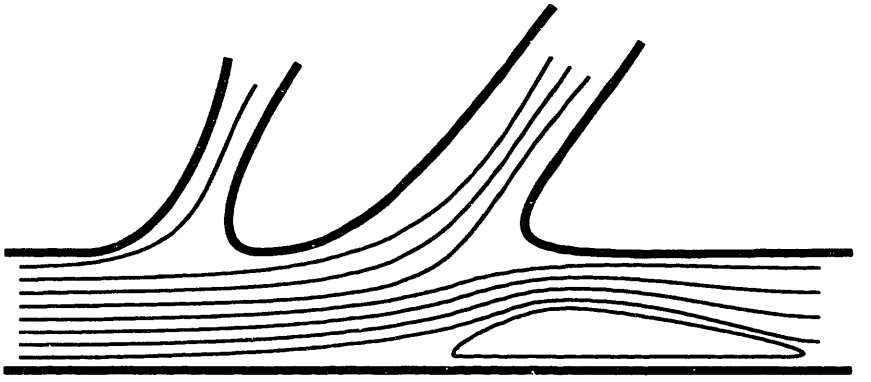

Figure 1-05: Flow Through a Dilated Bifurcation. The side branch has been dilated, however the main branch and the global conditions have remained the same as those as in fig. 1-04. This non-optimized geometry leads to the formation of a new region of boundary layer separation in the main branch.

At this point, we re-consider the previous discussion of time scales. A system which normally reacts to changes in the flow regime that take place over the course of years to decades, is now presented with a vast alteration in flow over the course of minutes to hours. The biological reaction to such a change can be expected to be different from the controlled normal reaction. Rather, the system might react in an uncontrolled manner to produce a lesion in the main branch rather than stopping at a mild taper.

The experiments outlined in this thesis track this general scenario and demonstrate the properties of flow at each stage. Flow is analyzed using several different tools to both verify the theoretical predictions made above, and to attempt to predict what their implications might be. This is done in a manner that does not attempt to be true to any specific set of parameters measured in a real case, or even those indicated by taking an average of all cases. Rather, it is performed in a generalized manner so as to attempt to tease out the underlying qualitative rules that govern these processes regardless of the data pertaining to the individual case. The theoretical and model predictions are then verified and validated in an *in-vivo* model of vascular disease. Finally, the predicted adverse effect of dilation of a side branch is tested *in-vivo* as it relates to main branch stenting.

Chapter 2 outlines the methods by which the flow model was built and analyzed. Chapter 3 presents the experiments performed and analyzes the results obtained. Chapter 4 outlines the animal model and the methods by which data were obtained and analyzed. Chapter 5 presents the chronic *in-vivo* experiments and analyzes the results. Chapter 6 presents the acute *in*-vivo experiments and analyzes the results. Chapter 7 contains general conclusions and discussion of future work.

2. Bench-Top Materials and Methods

This chapter will discuss the common methods used for all the bench top modeling experiments described in this thesis. The next chapter, which deals with specific experiments, will discuss the methods unique to each experiment and its result. Part one of this chapter will describe the fabrication of the physical flow model and its operation. Part two will discuss the instrumentation used to perfuse record and analyze flow through this model. Part three will deal with the general method for visualization of flow. Part four deals with dimensionless analysis and how it relates to the experiments performed here.

2.1. Fabrication and Operation of Mock Circulation

The flow model is formed in a Plexiglas container filled with a clear silicone compound, into which cavities in the shape of different geometries in the arterial tree have been formed. Fluid is perfused through these cavities to simulate blood flow. Adjacent to these cavities are pneumatic spaces that can be inflated and deflated to compress adjacent flow channels. The silicon plungers function as pneumatic "pusher-pullers", so as to enable a dynamic alteration in flow channel geometry to simulate different disease states and/or clinical intervention schemes.

Figure 2-01: Flow Model. The emptied flow model shows the bifurcating cavities. The pneumatic 'pusher-pullers' are shown at the bottom in their 'neutral' pressure.

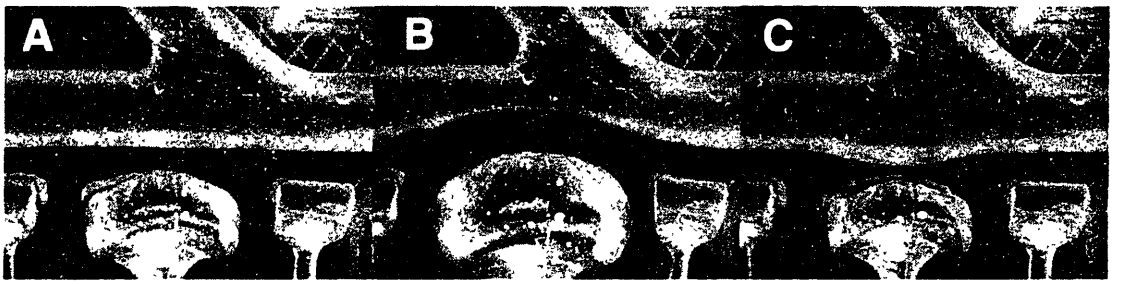

Figure 2-02: Pneumatic 'Push-Pull Plungers'. Operation of the plungers allows dynamic contiguous control over model geometry to obtain a straight vessel (A), tapered vessels (not shown), lesions (B) or aneurism (C)

The flow model is created in three main steps:

1. Creation of a solid cast of the flow channels and pneumatic spaces.
2. Fixation of the solid cast in a container and embedding in silicone.
3. Melting of the cast out of container to create flow channels/pneumatic spaces, and connection to external flow/pressure channels

2.1.1. Creation of the Solid Cast

The material for the solid cast must possess two important properties: It must be pliable enough to be shaped into smooth, non-obstructive flow models that are similar to arteries in their geometry and internal properties. Additionally, it must allow melting out of the silicone block without affecting its essential properties, such as optical clarity for flow imaging. Unfortunately, these properties are difficult to reconcile in one material. Initially wax was embedded directly into the silicone and melted out. Unfortunately, the petroleum present in wax reacts with the silicone when heated causing it to become opaque. Thus, a staged process was used that included first formation of the initial cast from wax, then formation of a polyurethane mold and finally cast pouring.

2.1.1.1. Formation of Initial Cast from Wax

Sculptor's microcrystalline wax was used to create the cast as it is soft and pliable when heated, allowing molding into virtually any shape. When cooled, it becomes hard and smooth and the shape can be retained. Small pieces of the wax were heated to 75°C for

approx. 4 minutes, and after slight cooling could then be rolled and kneaded into the required shapes. Bifurcations were formed by joining two cylinders of wax and filling in the creases. Push-pull plungers were formed by connecting a small cylinder or hemi-cylinder to a long stem (fig. 2-03). Final shaping was performed when the wax had cooled completely to achieve as smooth a finish as possible.

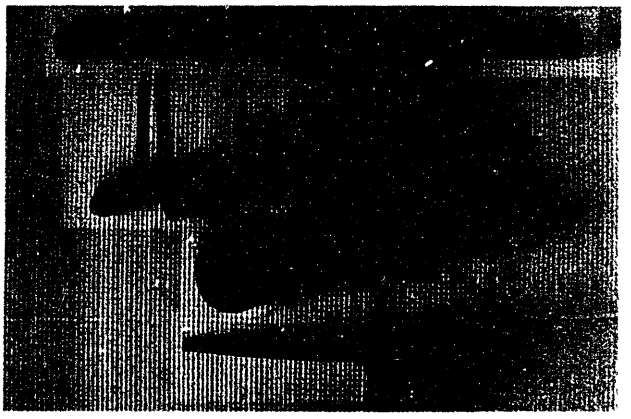

Figure 2-03: Wax Casts. Virtually any smooth geometry can be created from sculptors' microcrystalline wax. Bifurcation form is shown on top, together with a semi-circular, a concentric and a large and small push-pull device.

2.1.1.2. Formation of Polyurethane Mold

Since wax cannot be melted out of the silicone without altering its optical properties and the PEG that is ultimately placed in the silicone can be poured but not shaped, a mold is required to transfer the cast from one material to the other. The material for formation of this mold was a two part polyurethane compound (Smooth-On PMC-121/30 Dry - the 'dry' version was used since the normal PMC-121/30 compound exudes a mold release material that dissolves the wax). A container for holding the wax and polyurethane was assembled and sealed. The wax piece was suspended inside the container and aligned along a horizontal plane that passes through the entire wax piece (fig. 2-04). Long pieces were supported from below to prevent sagging.

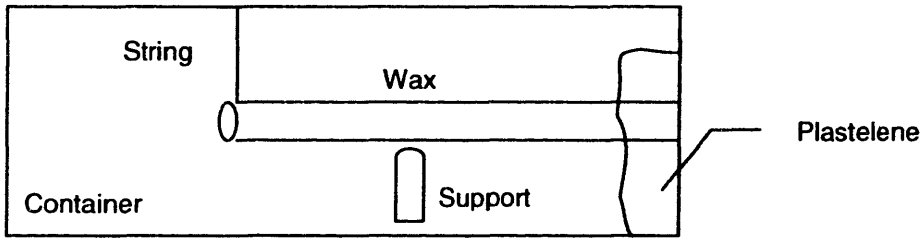

Figure 2-04: Creation of Polyurethane Mold. The wax cast is supported by insertion into plastelene on one end, a string support on the other, and a plastic rod from the bottom to prevent bowing. Polyurethane is then poured into the container, first up to the middle of the wax piece to create the bottom half, and then (after hardening) the top half.

Polyurethane was mixed and poured into the container up to halfway up on the wax piece and then allowed to set partially. Plastic cylinders of approx. ½cm diameter and 6cm length were halfway submerged in the partially cured polyurethane. These cylinders would ultimately be used in aligning the two halves of the polyurethane mold. Once the bottom half of the mold was fully cured, a layer of Teflon spray (Smooth-On Mold Release) was sprayed on the top face and allowed to dry. The second half of the polyurethane mold was poured into the container and allowed to cure. The mold was removed from the container, opened and the wax piece removed. The two halves were re-assembled using the plastic cylinders as guides for alignment.

2.1.1.3. Pouring Final Cast

The final cast was made of Poly(Ethylene Glycol) (PEG). The molecular weight of the PEG must be between 1000-1500 for the cast to be solid and smooth, but not brittle at room temperature. The PEG was melted and poured into the polyurethane mold created previously. Once the PEG cooled, the mold was opened and the PEG carefully removed. The end properties of the PEG piece are highly sensitive to the temperature at which the melting was done. To produce a smooth non-brittle piece, the temperature cannot greatly exceed the melting temperature of the PEG. For the 1500 molecular weight PEG this should be no higher than 60°C.

2.1.2. Fixation of Cast and Embedding in Silicone

A clear Plexiglas container for the model was built and sealed using silicone sealant. The bifurcation cast and all of the push-pull plungers were then fixed in the container. A gap of at least 3 cm between the container and outer most PEG piece is required to prevent bursting of the model from the imposed pressure. The PEG pieces were interfaced to the outside tubing through the container walls using specially built glass tubes. The details of the design of these tubes are crucial to their function (fig. 2-05).

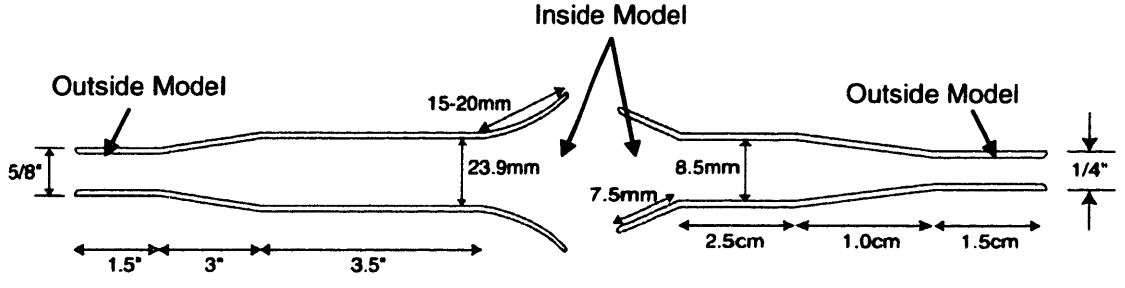

Figure 2-05: Glass Interface Pieces. The glass binds to the silicone on the inside of the model and connects to tubing on the outside. A large piece for the bifurcation arm (left) and a small piece for the push-pullers (right) are shown.

The inner diameter of the internal end was slightly oversized relative to the external diameter of the PEG piece. The flaring out of the internal end of both pieces creates an O-ring effect that seals off the interface between the silicone cavity and the glass when the model is pressurized (fig. 2-06).

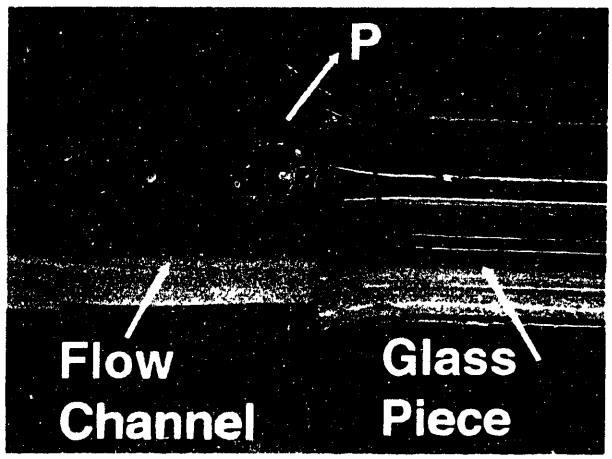

Figure 2-06: O-Ring Effect. In this image of the finished model, the top arrow indicates the direction in which the force is applied on the cavity by the pressure. This force presses on the inside of the flared glass segment and seals the connection against leaks.

The mid portion of each glass tube was plugged by pouring molten PEG into it. The glass tube was then held vertically with the internal end facing up and the end of the PEG cast was inserted down to the plug (fig. 2-07). The narrow space between the PEG piece and the glass was sealed by injection of molten PEG.

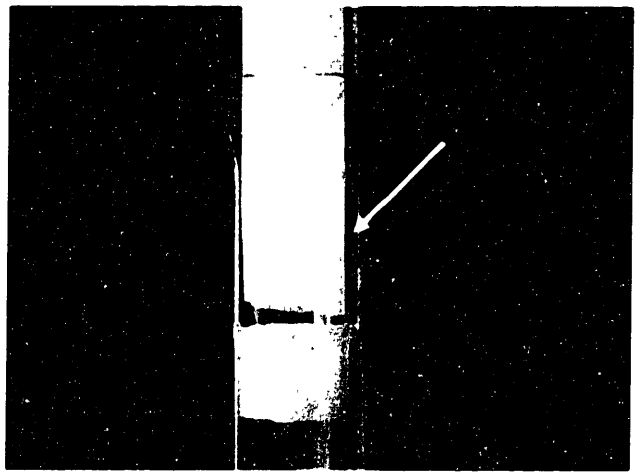

Figure 2-07: Interface Sealing. Image shows one arm of the bifurcation PEG cast inside the glass interface piece prior to sealing. PEG is injected into the space denoted by the arrow to create the seal.

Holes were drilled in the walls of the Plexiglas container for the glass interface pieces. The interface pieces were then threaded through the holes, sealed using silicone sealant

and fixed in place with a ring of epoxy cement that surrounded the glass and bound it to the Plexiglas.

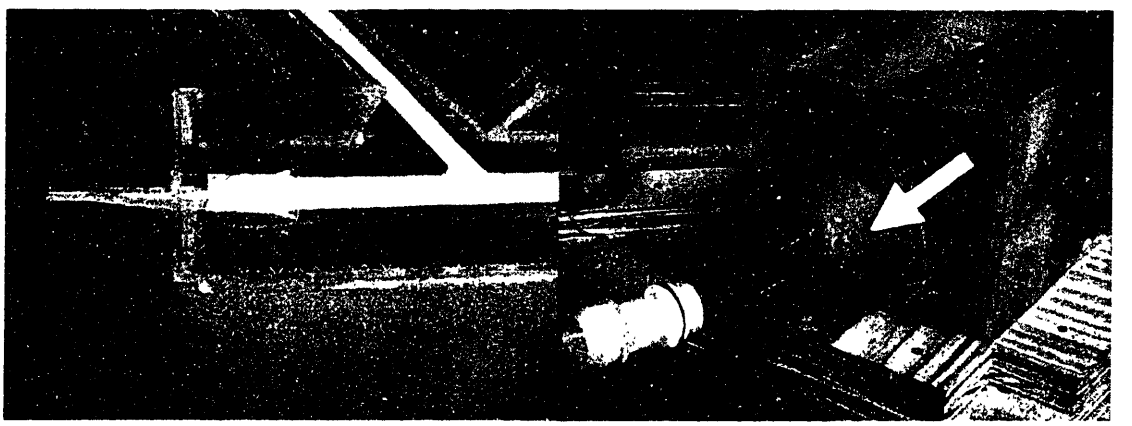

Figure 2-08: Fixation of PEG Cast. The interface pieces are threaded through holes in the model container cleft and then fixed in place with an epoxy ring (arrow on right)

If needed, push-pull plungers can be stabilized from above prior to the initial pouring of silicone. After the bottom half has hardened and prior to pouring of the top half, these supports can be removed as the pusher-pullers are now stabilized by the silicone. Clear silicone rubber (GE Silicones RTV 6166) was mixed at a ratio of 1:2 part A to part B respectively (rather than the classic 1:1 ratio) so as to increase the stiffness of the model. For models of depth greater than approx. 8cm it is preferable to pour the silicone in two halves, allowing the bottom half to cure before pouring the top half. This two part process allows air bubbles in each half to escape to the surface before the material is fully cured.

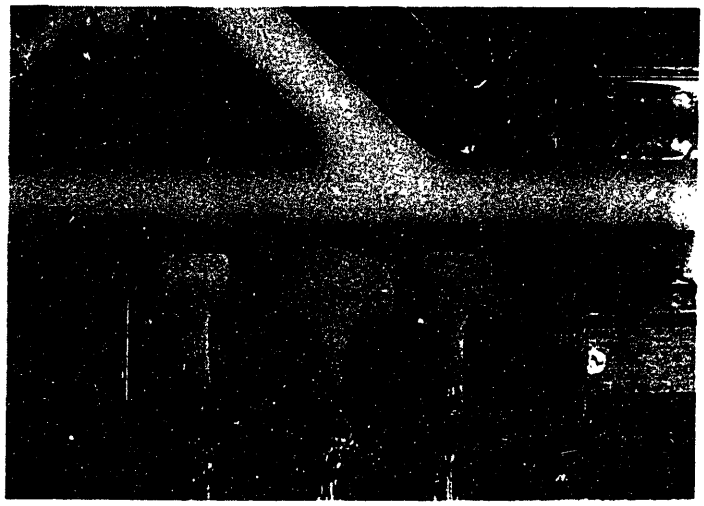

Figure 2-09: Model After Curing of Silicone. The bifurcation is seen on top, three push-pull one-sided plungers on the bottom and a concentric push-puller at top left. The silicone itself is transparent and cannot be seen.

2.1.3. Melting and Connections

The final step in fabrication of the flow model involves melting the cast out of the silicone. The container with the silicone was mounted onto a wood support and placed vertically in an oven heated to 70 C. This temperature is sufficient to melt the PEG but not high enough to warp the Plexiglas. Complete melting of the PEG takes several hours and any residual PEG in the flow channels can be cleared by running hot water inside the model. Tubing from the pump was fitted onto the external part of the glass interfaces. Smaller diameter tubing was fitted onto the external part of the interfaces for the push-pull plungers and then connected to syringes to impose the pressure differences that inflate/deflate the plungers. The entire container was mounted to slope upwards from proximal to distal to ensure that no air bubbles would be trapped within the model segment during an experiment.

2.2. Instrumentation and Analysis

2.2.1. Flow Circuit

The silicone model was placed inside of a flow circuit which was comprised of:

1. Lower reservoir and tubing – a container with a spout at the bottom. Filled with the perfusing fluid prior to running the model.
2. Pump – For most experiments, a mechanically controlled pump was used (Harvard Apparatus Pulsatile Blood Pump model 1423). This model provides independent control over stroke volume, frequency and systole/diastole ratio. Some of the latter experiments were duplicated using a computer driven pump (Ismatec ISM 404) that allowed finer control of the input flow waveform.
3. Proximal tubing and ports – 5/8" PVC tubing was used to connect the pumps to the model. At different locations within the circuit, glass connection ports were inserted to allow access to the flow (fig. 2-10). These include: collateral take-off port, pressure-wire insertion port, proximal differential pressure sensor tubing port and particle injection port. A 3/8" PVC tube was used for take-off of collateral flow. The middle segment of this channel was made of silicone tubing to allow flow constriction and modulation. This channel ran directly from the pump to the upper reservoir.
4. Flow model – described previously.
5. Distal tubing, ports and resistors – 5/8" PVC tubing was connected to both branches of the model and used to mount flow sensors. Distal to the flow sensors, ½" silicone tubing was used up to the reservoir. On this stretch of tubing, mechanical resistors were mounted to simulate distal bed resistance. Main branch tubing could be fitted with pressure port for distal differential pressure sensor tubing in the same way as proximal port was done.

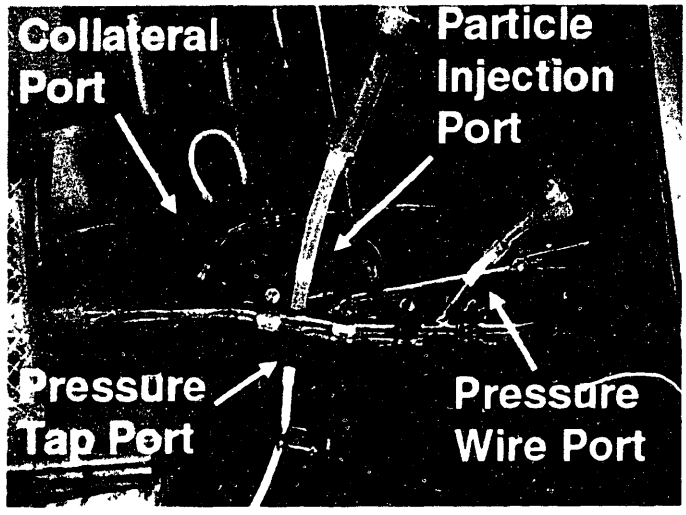

Figure 2-10: Proximal Ports. The collateral port bypasses the entire bifurcation. The particle injection port is used for visualization and the two pressure ports used to measure either differential pressure (second port located distal to the bifurcation) or point pressure (using a pressure wire).

6. Upper reservoir and tubing – second container with spout at bottom and holes for insertion of distal tubing coming from model and collateral at top. The bottom spout was connected via tubing to top of lower reservoir.
7. Perfusing fluid: 40% aqueous glycerol solution with a measured kinematic viscosity of $\nu = 0.027$ Stokes and a specific gravity of 1.1.

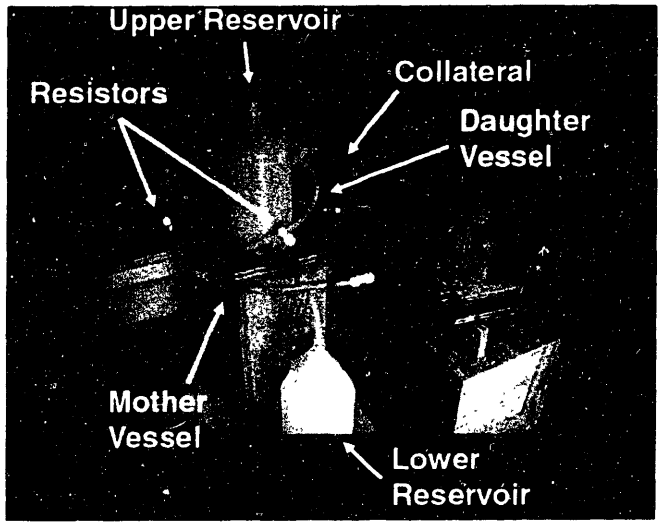

Figure 2-11: Distal Tubing and Reservoirs.

2.2.2. Flow Waveform Acquisition

Ultrasonic flow sensors (Transonic C-series clamp-on) were interfaced into a controller unit (Transonic T-206) and mounted on the distal ends of both the main branch and the side branch (fig. 2-12) to generate continuous flow-rate waveforms. These particular sensors provided two important advantages: first, as they were not placed within the tubing they did not affect flow. Second, they measure the flow across the entire cross-section of the tube and hence are not affected by the shape of the flow profile. The output signal from the sensors' controller was fed into an A/D board (National Instruments DAQ-Pad 1200, working at bipolar (±5V) reference single ended mode). Data was displayed and recorded using National Instruments LABView software at a sampling rate of 100Hz. The total flow in the collateral, where relevant, was determined from the difference between the sum of the integrated flows in the two branches with the collateral open and when occluded. Since the pump characteristics remain the same, the difference was assumed to be the flow in the collateral channel.

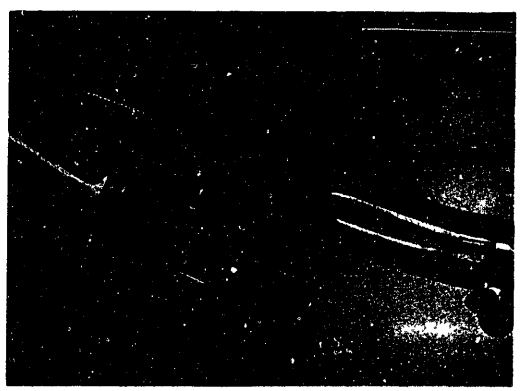

Figure 2-12: Flow Sensor. Transonic clamp-on ultrasonic flow sensor shown mounted on tubing distal to the main branch. A second sensor was mounted distal to the side branch to give the total flow.

2.2.3. Pressure Waveform Acquisition

Two options were available for generation of pressure waveforms: differential pressure between two locations and referenced pressure at a point.

2.2.3.1. Differential Pressure

A differential pressure sensor (fig. 2-13) was fabricated using a Motorola MPX10DP differential pressure sensor (pressure range = 1-1.5 psi). For a description of the amplification circuits and operation see appendix A. Pressure input to this sensor was connected via two silicone tubes leading from the pressure tap in the flow tubing on one end, to the port on the differential pressure sensor on the other. The positive and negative terminals on the sensor were connected to the proximal and distal pressure taps respectively. The tubes themselves were air filled and thus avoided contact of fluid with sensor interior.

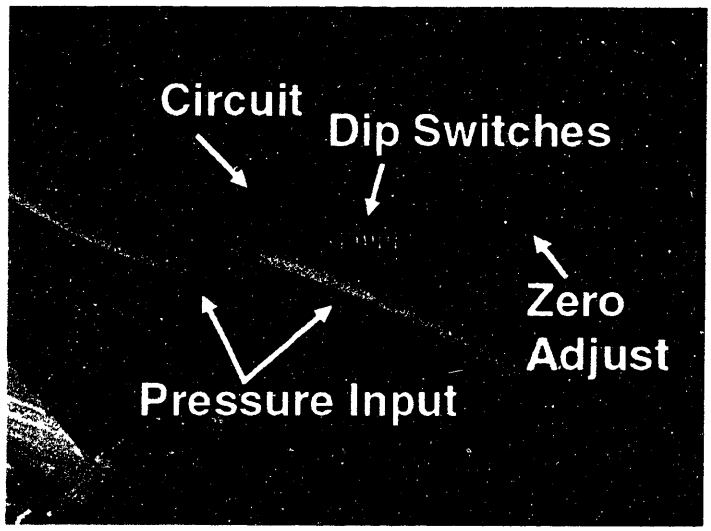

Figure 2-13: Differential Pressure Sensor. The Motorola MPX10DP sensor is embedded within the conditioning and amplification circuit.

2.2.3.2. Point Pressure

Two different methods were used to obtain pressure at a given point as opposed to differential pressure. For points outside of the silicone model, a pressure tap was connected to the positive pressure terminal of the differential pressure sensor, with the negative terminal connected to a fixed, know hydrostatic column (fig. 2-14).

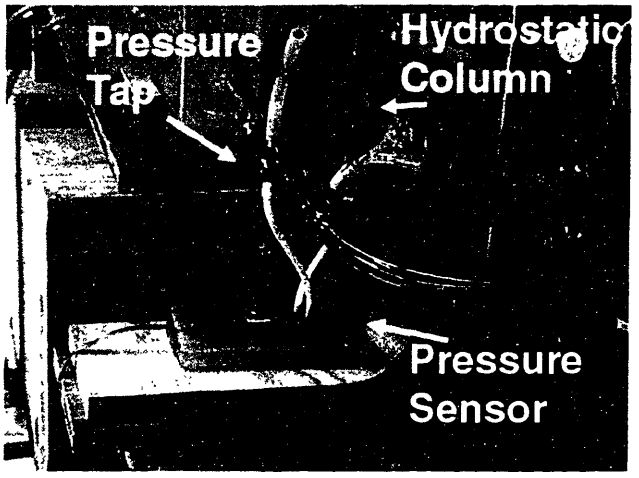

Figure 2-14: Proximal Pressure Measurement. The differential pressure sensor is connected to the proximal port and referenced to a hydrostatic column.

For pressure at points inside the silicone model, a pressure wire (RADI Medical PressureWire) was inserted via the pressure wire port (fig. 2-15) and advanced to the point at which pressure was to be measured. The port opening was then sealed off.

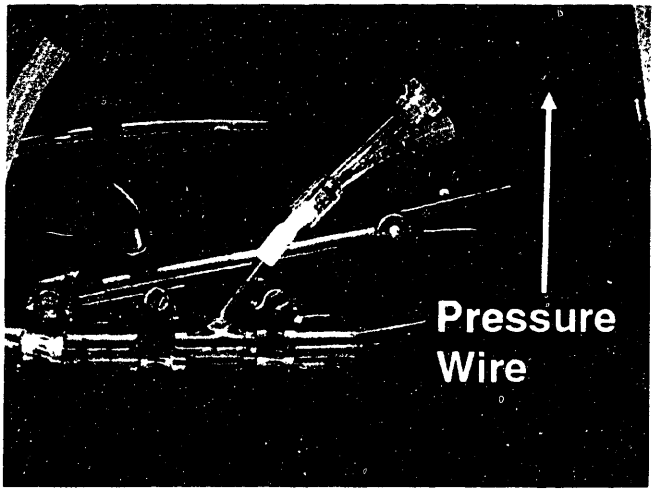

Figure 2-15: Pressure Wire Measurement. Internal pressure was measured by inserting a RADI pressure wire through the proximal port and advancing into any location within the model.

The RADI controller was fed into an amplification circuit (see appendix A) and the amplified signal was fed into the A/D board for on-line recording.

2.2.4. Waveform Conditioning and Synchronization

Once recorded, pressure and flow waveforms were loaded into MATLAB for offline analysis. Most of these waveforms was noisy and were digitally filtered (see appendix B) using a low-pass filter with a cutoff frequency of 1Hz. to preserve at least the first 10 harmonics of the fundamental frequency. For experiments that included both waveform and visualization (discussed in part III of this chapter), the waveform and video timeline needed be synchronized. The method for synchronization is was follows:

1. At the end of the experiment the pump was turned off abruptly during mid systole.
2. Flow was allowed to subside for approx. 30 seconds and the pump was turned back on.
3. Steps 1&2 were repeated 3 or 4 times.
4. The instant at which the pump was turned off could be identified on the pressure waveform as a discontinuous fall in pressure. Similarly, the instant at which the pump was turned back on could be identified on the pressure waveform.
5. The same on/off events could be identified on the video timeline by using video editing software (Adobe Premiere 5.1) to search for the loud clicking sound of the pump switch on the audio line (fig. 2-16).
6. The difference between these two timelines was averaged for several on/off cycles and the waveform timeline was shifted accordingly so that both timelines coincided in time.

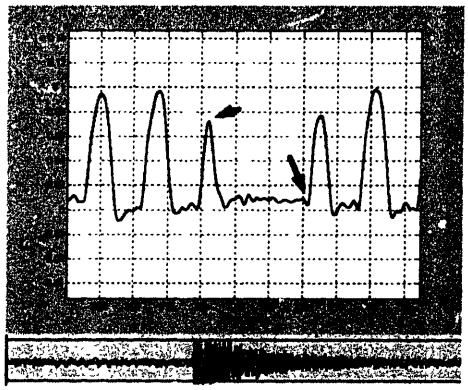

Figure 2-16: Waveform Synchronization. Arrows (top panel) indicate points on the pressure waveform at which the pump was turned off and then back on. The audio waveform (bottom panel) shows a sharp clicking sound created by the pump switch.

2.3. General Flow Visualization

Generation of flow visualization was performed by a two part process. Initially, enhanced still frame images of the flowing media were produced. These images were then processed by different methods to produce a description of the flow pattern. This section will describe the common process up to generation of the still frames. Conversion of these frames to images of flow visualization will be described in sections 3.3.1.1 & 3.3.1.2. Generation of still frames is comprised of three aspects:

2.3.1. Formulation of Tracer Particles

Polymeric microspheres were custom-made to serve as tracer particles for the flow model. The technique employed allowed for control of particle size, buoyancy and color. The fabrication procedure is described below. Each batch of spheres produced approx. 800 microspheres of median size approx. 1.3mm, adequate for performing one stage of visualization. Fabrication of one batch was as follows:

1. Polymer solution: 4gr. Polymer mixture of poly(styrene) and poly(methyl methacrylate) at a mixture ratio of 7:3 respectively in 15cc Methylene Chloride. The ratio could be varied slightly in either direction to produce slightly heavier (less styrene) or lighter (more styrene) particles. The polymer was allowed to dissolve while stirring overnight.
2. Surfactant solution: 300cc of 1% w/v poly(vinyl alcohol) in water.

3. The surfactant solution was spun in a 500cc beaker using an overhead stirrer at a rate of 300 rpm.
4. The polymer solution was loaded into a 1cc syringe and dropped at a rate that maintained individual drops into the spinning surfactant solution through a 26G needle. This was performed a total of 4 times.
5. The particles spun for 30 minutes and were then emptied into a second beaker spun with a stirrer bar overnight. Steps 4&5 were repeated until the entire 20cc of polymer mixture was consumed.
6. The particles was washed of the surfactant and placed in the perfusing mixture of water and glycerin. Over the first 24 hours the particles gradually become lighter, after this period they achieve steady state.

2.3.2. Filming and Image Acquisition

1. Lighting: Optimal lighting was achieved using ambient light while surrounding the model itself with a cotton cloak to create an indirect diffuse lighting effect.
2. Contrast: Maximal contrast between particles and background was achieved by placing dark colored cardboard beneath the bottom of the Plexiglas box.
3. Filming: Filming was performed using an off the shelf 3CCD digital video camera (Sony TRV-9000) mounted above the flow model perpendicular to the plane of the bifurcation. The camera has an inherent rate of 30fps and resolution of 720X480. Shutter and exposure were set to automatic and the focus was allowed to set automatically and then frozen on manual to prevent fluctuations in focus.
4. Acquisition: Movie files were digitally acquired using a Sony PCG-XG9 Laptop with an i-link 1394 FireWire interface. The movies were then imported into Adobe Premiere and still frames exported for the relevant flow phases.

2.3.3. Image Enhancement

The goal of image enhancement was to produce maximal contrast between particles and background with minimal noise. This greatly improved the quality of the ultimate flow visualization both by streamline visualization and Particle Image Velocimetry (discussed later). Enhancement was performed using Adobe Photoshop as follows:

1. A binary mask image was prepared containing an outline of the channels of flow shaded in with one color and everything else shaded in with a different color.
2. The mask image was pasted onto the original image as a second layer.
3. The background shade was selected using the magic wand tool.
4. The mask image layer was cleared.
5. The selected area was filled uniformly with black.
6. The image levels were adjusted using the autolevels command.
7. The Magic wand tool with a tolerance of 2 was used to select one of the particles in the image. The select similar command was used repeatedly to expand this selection to all of the particles. The command was repeated as many times as possible without including the background in the selection.
8. The selection was inverted and the background was filled uniformly with black.
9. The image mode was converted to grayscale. Image levels were adjusted using the autolevels command.
10. Noise was reduced using the despeckle filter.

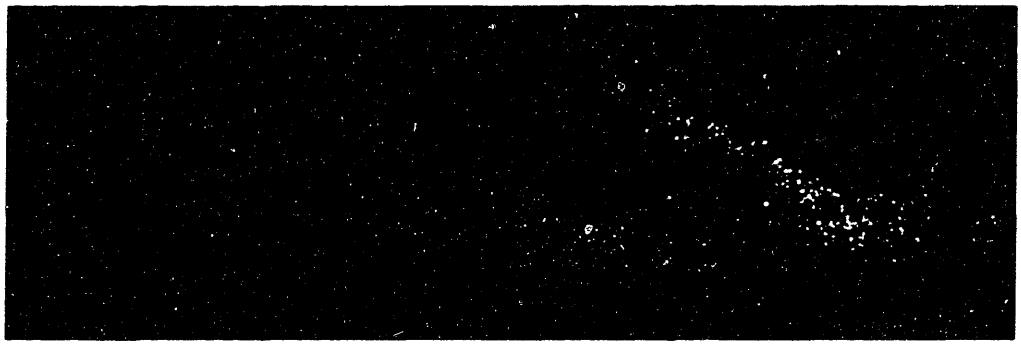

Figure 2-17: Image Enhancement. Left panel shows the original still image derived from digital video. Right panel shows the same image after enhancement to maximize contrast between particles and background.

2.4. Dimensional Analysis

Many engineering problems exist for which a rigorous analytical solution to the governing equations simply cannot be achieved. These problems are often examined with physical modeling; so it is with the scenarios investigated in this work. The building of physical models is complicated by many factors, several of which are discussed in this

thesis, of which the issue of length scales is perhaps the most obvious. Models that test large structures like aircraft or ships are typically reduced in scale. On the other hand, models that test small prototypes, such as flow in the arterial tree, are typically enlarged in scale to make the measurements and observations easier to perform. Dimensionless analysis provides a mathematical framework that allows one to correctly interpret the results obtained in testing of a scaled model to the expected data in the prototype.

The basis for dimensional analysis is the concept of *dynamic similarity* and can in a simplified form be understood as a scaling factor for differences between the prototype and model systems. For any system, in our case a flow field, a set of dimensionless parameters can be defined, which describe the interaction and relative weight of forces acting on the flow. Each parameter is a function of the dimensions of the model (e.g. length, diameter, etc.), the properties of the fluid (e.g. viscosity, density, etc.), the properties of the flow field (e.g. velocity, frequency of pulsatility), the properties of the environment (e.g. temperature) and others. Maintaining dynamic similarity between a model and a prototype implies that all of these dimensionless parameters are kept at exactly the same values. For example, in order to maintain the well known Reynolds number constant, if the length of the model is scaled up by a factor ten but the viscosity remains the same, the velocity must be scaled down by a factor ten in order to maintain dynamic similarity. Under these conditions, the flow field can be expected to be geometrically similar i.e. have the same shape as the one in the prototype.

To achieve dynamic similarity all relevant dimensionless parameters of fluid flow must be kept constant. Some examples of dimensionless groups that arise in various situations include: Reynolds number, Strouhal number, Weber number, Womerseley number, Froude number, Cavitation number, Mach number, Prandtl number, Nusselt number, the steady and unsteady pressure coefficients as well as many others. In practice, as many of these parameters can be expressed as combinations of the others, maintaining some parameters constant ensures that at least some of the others will remain constant as well. Practical considerations and limitations however, typically limit the number of coefficients that can be kept constant in an experimental model. Since the number of properties that make up the dimensionless parameters is finite, often times in a scaled model maintaining one dimensionless parameter constant will actually directly contradict

maintaining some other dimensionless number constant. This problem necessitates defining of the most relevant dimensionless parameters that affect the given problem of interest, rating these in order of importance and then maintaining as many of the important parameters as possible.

We proceed then to analyze the dimensionless parameters that are most relevant to the problem of the shape of the flow field within arteries:

2.4.1. The Reynolds Number

Definition: $\mathrm{Re} = \frac{\rho V L}{\mu}$

Where ρ is the density of the fluid, V is the characteristic velocity[vii], L is the characteristic length of the system[viii], and μ is the dynamic viscosity of the fluid. This is often replaced by:

$$\mathrm{Re} = \frac{VL}{\upsilon}$$

Where ν is the kinematic viscosity of the fluid.

Significance: The Reynolds number gives the ratio of inertial forces to viscous forces acting on the flow. As such it is extremely important in determining the flow regime one is working in. At low Reynolds numbers, flow can be expected to be very sluggish, with minimal boundary layer separation and take a long time/space to develop. At high Reynolds numbers, fluid inertia gives rise to phenomena such as boundary layer separation and the formation of recirculating eddies. The Reynolds number also has an intimate link to the phenomenon of turbulence as opposed to laminar flow. The transition from a laminar flow regime to a turbulent one was a topic of Lord Osborne Reynolds' original research. His data showed that at low Reynolds numbers, flow in a straight smooth pipe remained laminar throughout. At a Reynolds number of approx. 2300 (known as the "upper critical Reynolds number"), laminar flow would spontaneously undergo a transition into turbulence. On the other hand, below a Reynolds number of

---

[vii] In the case of flow through a closed channel such as the case of arteries this is typically taken as the mean velocity of flow in the channel.

[viii] In flow through a closed channel this is typically the diameter of the tube.

approx. 1800 (known as the "lower critical Reynolds number"), turbulent flow would revert back to laminar. The precise quantitative nature of these results changes from one system to the other. In the case of arterial bifurcations for example, both the pulsatility of flow and the bifurcations themselves can be expected to significantly reduce the critical Reynolds numbers. Qualitatively however, the general result holds true – significantly below the critical Reynolds numbers, spontaneous conversion of laminar to turbulent flow is not expected to occur and if, by whatever mechanism, turbulence has been introduced into the flow, at low Reynolds numbers it would not be expected to persist. Perhaps the only way to measure flow without disturbing it is by using what is known as a "flow wire", which is a thin (0.014") guidewire of the type used to direct the placement of endovascular devices such as balloon catheters mounted with a piezoelectric crystal[44,45]. This device makes use of the Doppler Effect to obtain the flow velocity in the vicinity of the crystal. The problem with this method stems from the fact that the cross-sectional location of the wire in the artery is practically impossible to control and hence some velocity profile must be assumed to relate the velocity measured by the crystal to the mean velocity of the tube. Most of these devices assume a fully developed laminar profile in a tube, i.e. the Haggen-Poiseuille parabolic flow. In practice however, issues such as entrance length, bifurcations and a non-negligible Womerseley number (discussed hence) all work to make the flow non-parabolic hence invalidating this assumption[46].

These issues not withstanding, one must ultimately attempt to estimate the Reynolds number in arteries. Common ranges cited in the literature are:

Artery	*Reynolds number range*
Coronaries	90[47][ix] - 300[32]
Ascending Aorta	1100[48]
Common Carotid	180[33]
Renal	300-500[49]

Table 2-1: Reynolds numbers. Common values cited in the literature.

[ix] This is the only measurement given here made with flow wires.

Note that while there is a wide variation in these values, all the cited values (except perhaps the ascending aorta) are well below the lower critical Reynolds number, making the existence of turbulence improbable. Moreover, all the values belong to the same flow regime – one in which inertial forces are clearly dominant over viscous ones and yet are not high enough to provide for turbulence. In this sense it is really not the precise Reynolds number that must be kept constant but rather the order of magnitude of the Reynolds number as long as we are primarily concerned with the qualitative aspects of the flow field. This statement is in fact true for any one of the dimensionless parameters considered.

2.4.2. The Womerseley Number

Definition: $\alpha = \frac{L}{2}\sqrt{\frac{2\pi\rho f}{\mu}}$

Where L is a characteristic length of the system (most commonly diameter), ρ is the density of the fluid, μ is the viscosity of the fluid and f is the frequency of oscillations (heart rate).

Note: A common practice is to present α^2 often referred to as the "unsteadiness coefficient".

Significance: The Womerseley number gives the ratio of *transient* inertial forces to viscous forces and is thus sometimes referred to as a "Reynolds number based on frequency". It provides an estimate of the extent to which the flow profile is affected by the frequency in a pulsatile system. At low Womerseley numbers (usually corresponding to low frequencies), the flow is usually "quasi-steady" i.e. at every instant in time the properties of flow (for example the profile) are determined by the boundary conditions (e.g. pressure) as if the flow was steady with these boundary conditions held constant. At high Womerseley numbers on the other hand, the profile does not have time to develop and the instantaneous flow profile is typically blunted with respect to the parabolic one (fig. 2-18). Absent the time for shearing forces which originate from the wall to diffuse and shape the entire velocity profile, the entire core of fluid moves almost as a whole, a condition sometimes referred to as 'slug-flow'.

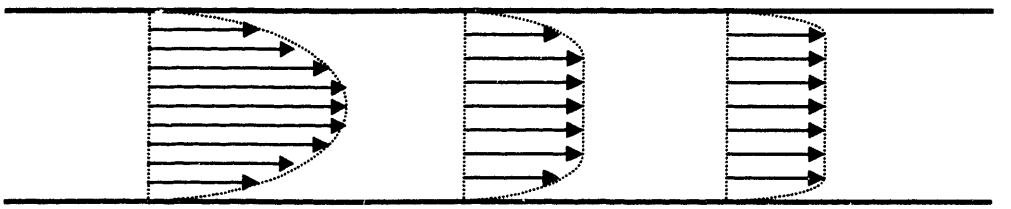

Figure 2-18: Effect of Womerseley Number on Profile. Increasing Womerseley numbers (from left to right) show the effect on the instantaneous profile from parabolic for low values to almost flat for high ones.

Once more we must answer the question: what are the relevant values in real arteries? Common estimates range between 5 and 15 depending on the artery in question. This places the *in-vivo* Womerseley number in the gray range of not really quasi-steady and not really slug-flow. Numerical and experimental measurements however have simulated this flow and the results in practice turn out to resemble the slug-flow situation much more closely than the instantaneously parabolic case[33,50,51].

Since this work is primarily focused on boundary layer separation and hence the velocity profile of flow within arteries, the Reynolds and Womerseley numbers were regarded as the most critical in importance. Thus an effort was made to keep these two parameters constant (or more precisely within the same regime) between prototype and experiment. Nonetheless, for completeness, we give consideration to several other dimensionless parameters

2.4.3. The Strouhal Number

Definition: $S_t = \frac{fL}{U_m}$

Where f is the frequency of oscillations (heart rate), L is a characteristic length (diameter) and U_m is the maximal flow rate.

Significance: The Strouhal number governs such things as the rate of break away of unstable vortices. A common everyday example of this is the wind whistling as it passes over wire.

Note that:

$$\frac{\alpha^2}{\mathrm{Re}} = S_t$$

So that keeping the Reynolds number and the Womerseley number the same will by definition also maintain the Strouhal number constant.

2.5. Calculation of Parameters for Mock Circulation

We begin by citing the relevant parameters for the prototype. Once more we note that there is considerable variation in the literature as to these values. We maintain however that since all these values are really within the same flow regime, and since the present work strives to present qualitative results and not precise numerical predictions, the use of one set of data is as good as another. In practice the data here is based on measurements obtained using flow wires in coronary arteries such as[44]:

Cross-sectional area: $A = 7.64\text{mm}^2$

Diameter[x]: $D = 3.12\text{mm}$

Mean velocity: $U_{ave} = 15\text{cm/sec}$

Frequency (heart rate): $f = 60/\text{min}$

Viscosity of blood: $\nu = 0.05\text{stokes}$

These values allow us to calculate the following values for the dimensionless parameters:

Reynolds number: $\mathrm{Re} \approx 100$

Womerseley number: $\alpha \approx 1.5\text{-}2.0$

Were it not for practical physical constraints, we would like to create a model that would reproduce these precise parameters. However, one is rarely placed in such a scenario, and in the physical model, the following constraints exist:

- To perform flow visualization effectively and to dynamically change the geometry of the model, as discussed in the materials and methods section, the diameter of the main branch of the model is constrained to be no smaller than approx. 2.5cm.

[x] Derived from cross-sectional area assuming circular cross-section.

- The stroke volume of the pump used to simulate the pulsatile waveform is limited to 100cc. In practice, as the frequency of the pump must be reduced greatly to match the Womerseley number, the stroke volume is limited to an even smaller value of approx. 60-70cc.
- The frequency of the pump cannot be reduced below approx. 0.1Hz.
- The viscosity of the fluid that can be pumped cannot greatly exceed that of the viscosity of blood.

Given these constraints, these are the values ultimately used in the modeling:

Diameter: $D` = 2.5cm$

Stroke volume: $SV` = 65cc$

Frequency: $f` = 1/9$ Hz.

Mean velocity[xi] $U`_{ave} = 1.4cm/sec$

Viscosity of fluid: $\nu` = 0.05stokes$

These values give the following for the dimensionless parameters:

$Re` \approx 70 \approx 0.7 \cdot Re$

$\alpha` \approx 4.7 \approx 2.7 \cdot \alpha$

As can be seen, the values for both the Reynolds and the Womerseley numbers are not identical to the prototype, and yet are sufficiently close to produce reasonable qualitative results.

[xi] Derived from SV`, D` and f`.

3. Bench-Top Experiments

This chapter describes the 4 main modeling experiments performed in this work:

I. Establishment of flow regime.

II. Mathematical modeling.

III. Flow visualization – large side branch.

IV. Flow visualization – small side branch

Each segment dealing with an experiment is subdivided into three parts:

1. Theory. Describes the main theoretical concepts behind the method of the experiment and the hypothesized results.
2. Experiment. A description of the methods used in the experiment and the measurements performed.
3. Results and Discussion. The raw data obtained from the measurements performed in part 2 and a discussion of its possible meaning.

Flow circuit data:

Experiment	Stroke Volume (mL)	Pump Frequency (Hz)	Bifurcation Angle (degrees)	MB/SB Diameter Rratio
I	80	0.1	45	4:3
II	80	0.1	45	4:3
III	65	0.11	45	1:1
IV	65	0.11	45	2:1

3.1. Establishment of Flow Regime

Analysis of the regime of flow lends important insight into the phenomena that can be expected to occur. In addition, this regime can aid in the fabrication and validation of the construction of physical models.

3.1.1. Theory

The physical parameters measured in the present experiments, pressure and flow rate, are related to each other by the fluid dynamic impedance of the vessel segment. The generalized Ohm's law describes this relation:

$$\Delta P(t) = Z(\omega) \cdot Q(t)$$

Where ΔP(t) is the instantaneous pressure drop in the vessel, Z is the frequency-dependent fluid dynamic impedance of the vessel and Q(t) is the instantaneous rate of flow in the vessel.

The impedance of the vessel segment is comprised of three independent components: resistance, compliance and inertance. The geometry as well as the conditions of flow determines the values and the relative importance of these three factors.

3.1.1.1. Resistance

The simplest flow scenario is that of steady flow in a straight long tube of constant cross section with rigid walls. For this flow, the resistance is given by the Hagen-Poiseuille equation:

$$\Delta P = \frac{128\mu L}{\pi D^4} \cdot Q$$

Where ∇P is the pressure gradient, μ is the fluid viscosity, Q is the flow rate and D is the tube diameter.

The fluid dynamic resistance is defined in analogy with electrical resistance:

$$R \equiv \frac{\Delta P}{Q}$$

and hence is given by:

$$R = \frac{128\mu L}{\pi D^4}$$

Since R is not frequency dependent, its contribution to the total impedance is simply:

$$Z_R = R$$

3.1.1.2. Compliance

The elasticity of the blood vessel wall imposes a compliance component of the fluid dynamic impedance. In the same way that the fluid dynamic resistance is analogous to electrical resistance, the compliance is analogous to electrical capacitance. It is defined by:

$$-Q = C\frac{\partial(\Delta P)}{\partial t}$$

Its contribution to the total impedance is given by:

$$Z_C(\omega) = \frac{C}{\omega}$$

Where C is the compliance, which is a constant determined by the geometry and the material properties of the vessel, and ω is the frequency of oscillations of flow.

As is reflected in the equation above, the contribution of compliance to the total impedance is inversely related to the frequency. At high frequencies, the vessel wall does not have sufficient time to expand and contract and hence the effect of compliance is negligible. At low frequencies on the other hand, the vessel expands and contracts considerably during each cycle and the compliance has a major effect on the flow.

3.1.1.3. Inertance

A third contribution to overall impedance is imposed by the inertia of the fluid. The electrical analogy here is with inductance. The inertance is defined by:

$$-\Delta P = I\frac{\partial Q}{\partial t}$$

such that its contribution to the total impedance is given by:

$$Z_I(\omega) = \omega I$$

Where I is the inertance, which is a constant determined by the geometry and the material properties of the fluid, and ω is the frequency of oscillations of flow.

In contrast to compliance, the inertance contribution to the total impedance is proportional to the frequency. At very low frequencies, flow is for the most part unidirectional and so inertia plays very little role. At high frequencies, fluid is constantly being accelerated and decelerated and thus inertia plays a major role in determining the pressure required to move fluid.

In the most general case, the impedance and hence the relation between the pressure drop in the vessel and the flow rate is determined by a combination of all three components. However, under certain conditions the fundamental frequency of the oscillations dictates that either the compliance or the inertance is negligible, greatly simplifying analysis of the model. In the case of blood flow in the arterial bed, we hypothesize that the

contribution from compliance is very small and can be neglected leaving just the inertance and resistance as the major components of impedance.

3.1.2. Experiment

The assertion that this is an inertia-dominated system was validated by the following method: The pressure drop waveform in the main vessel was recorded using pressure taps feeding into a differential pressure sensor. The proximal tap was located immediately upstream from the model (fig. 3-01), and the distal tap was located immediately downstream from the model on the main branch. Flow rate in the main branch was recorded using the flow sensor mounted on the tubing carrying the main branch flow.

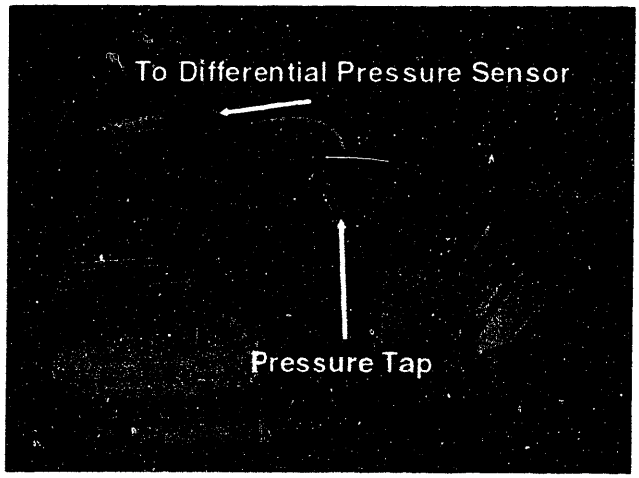

Figure 3-01: Differential Pressure Tap. Pressure is measured just proximal to the model segment and just distal (not shown) and fed into the differential pressure sensor.

Both the differential pressure and the flow-rate waveforms were decomposed into their Fourier spectrum. For each integer multiple of the fundamental frequency the Fourier coefficient for the differential pressure drop was divided by the Fourier coefficient for the flow rate. This produces a plot of the impedance as a function of frequency. In the compliance-dominated regime, the magnitude of the impedance should drop with increasing frequency. In the inertance-dominated regime, the magnitude of the impedance would be expected to increase with frequency.

3.1.3. Results and Discussion

The plot for the magnitude of the Fourier transform of the differential pressure waveform and the flow waveform is given below (fig. 3-02), as well as the magnitude of the impedance as a function of frequency.

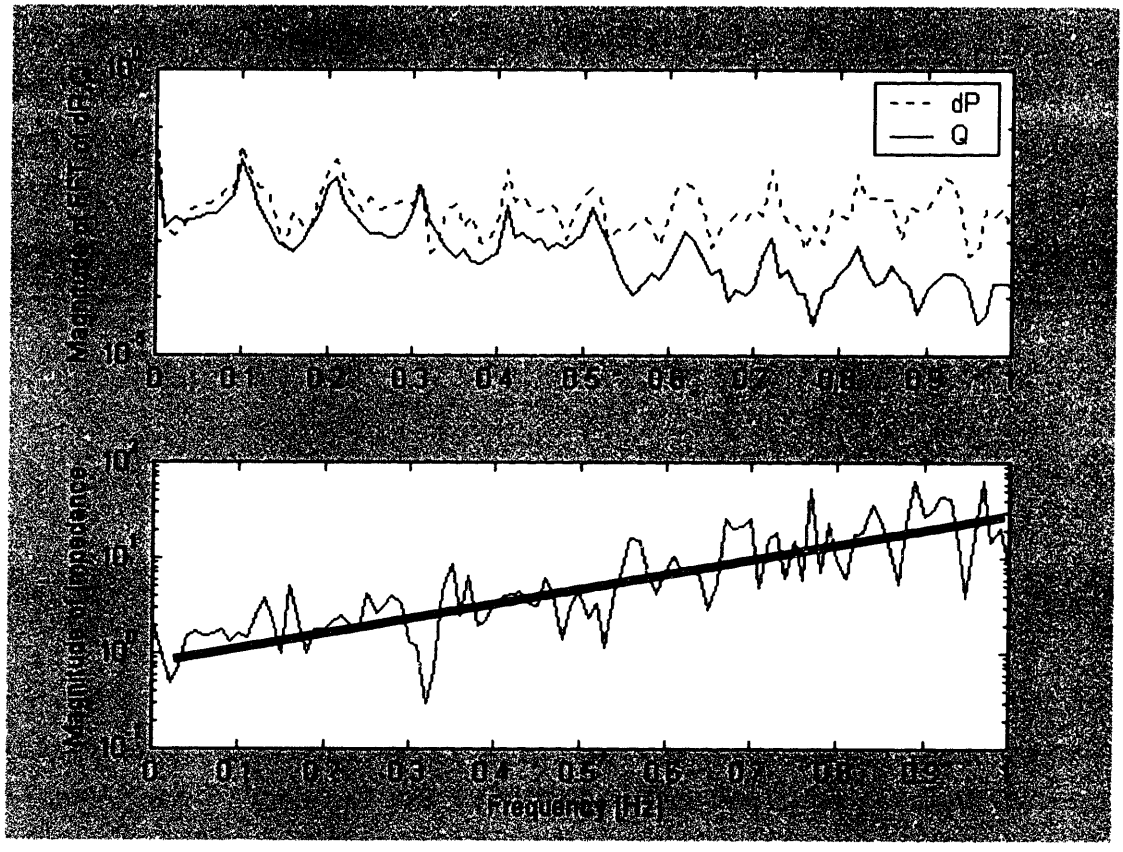

Figure 3-02: Fluid Dynamic Impedance. Top panel: Magnitude of FFT of differential pressure and flow waveforms. Note the harmonics at integer multiples of the fundamental frequency of 0.1 Hz. Bottom panel: Magnitude of the fluid dynamic impedance (in arbitrary units) as a function of frequency. Note the increase in impedance with increasing frequency.

The top panel of figure 3-02 shows the expected form of the Fourier transform of both the flow rate and the differential pressure waveform. Harmonics can be seen at integer multiples of the fundamental frequency of the pump which is approx. 0.1Hz.

In the bottom panel, when one transform was divided by the other, these harmonics can no longer be distinguished. Inspection of the bottom panel (note the logarithmic scale) shows that the impedance clearly increases with frequency. As discussed previously, this increase indicates that the system is inertia- as opposed to capacitance-dominated. In

some respects, the frequency dependence observed here contradicts the traditional first order model of the vascular system, the Windkessel model, which only includes resistance and capacitance elements. The apparent disparity between the two models is most plausibly explained by the inclusion of the entire vasculature from the aorta onwards in the Windkessel model. The aorta is the primary site of vascular compliance, and would naturally require a capacitor rather than an inductor. The present model on the other hand deals with a more isolated portion of the circulation, namely that of a group of distributing arteries such as the coronary arteries. These arteries are less compliant than the aorta, and as the volume they contain is much smaller their potential capacitance should be much less significant than that predicted by the Windkessel model. This result is consistent with the observation[52] that a non-compliant model was no worse at correlating between intimal thickness and measured wall shear than a compliant model. Finally, the observed frequency dependence justifies the use in the next experiment of a mathematical model that includes resistance and inertance, but not compliance. A system function H(S) for such an inertial-resistive model can then be written with two terms:

$$H(S) \equiv \frac{Q(S)}{\Delta P(S)} = \frac{1}{R + I \cdot S} \text{ or:}$$

$$\Delta P = (R + I \cdot S) \cdot Q$$

The first term is a resistance and is independent of S, frequency, reflecting the proportional relationship between pressure drop and flow rate. The second term includes a frequency component and reflects the fact that in a purely inertial system, the pressure drop is proportional to the time derivative of the flow rate as indicated by:

$$-\Delta P = I \frac{\partial Q}{\partial t}$$

Had the system had a significant compliance-related impedance, there would have been a need to incorporate one more term into the system function, inversely related to frequency (1/S).

3.2. Mathematical Modeling

Mathematical models can aid in the qualitative understanding and help construct quantitative descriptions of the physiological flow system. This requires proper validation, precise quantification and repeatable measurements.

3.2.1. Theory

In the most basic mathematical model of a linear physical system the system is defined by its response to a controlled stimulus. The output is measured and the form and nature of the transformation of the input that creates the output is defined as the *system transfer function*. Once the system transfer function is identified, the output waveform for an arbitrary input can be deduced. We can view the flow system as an input-output system if we define the differential pressure across the vessel segment as the input and the flow through the segment as the output or vice-versa. The system transfer function is then simply the LaPlace transform of the differential equation that governs the flow circuit. In the general case this circuit can be quite complex, however since we have shown in the previous section that this is an inertia-dominated system, we can neglect the compliance and model it at the lowest order as simply a resistance with an inertance in series, much like an electrical circuit of a resistor with an inductor in series. The differential equation governing this circuit is then:

$$\Delta P(t) = R \cdot Q(t) - I \cdot \frac{dQ(t)}{dt}$$

Taking the LaPlace transform of this equation we obtain:

$$\Delta P(S) = R \cdot Q(S) + I \cdot S \cdot Q(S)$$

And thus the system function is given by:

$$H(S) \equiv \frac{Q(S)}{\Delta P(S)} = \frac{I}{R + I \cdot S}$$

This function allows us, given a flow waveform to compute the predicted pressure waveform that would be produced. Alternatively, since the properties of the system - resistance and inertance - appear in the system function as free parameters, given a known flow and pressure waveform we can use the system function to find a fit for the resistance and inertance values.

Despite the obvious analogy between an electrical and a fluid dynamic resistance, there are important differences: An electrical resistor has a set value, independent of the circuit in which it resides or the current flowing through it. In contrast, the fluid dynamic resistance through a *fixed* geometry is dependent on the flow through it. For example, boundary layer separation can raise the resistance in a segment by altering the effective diameter for flow (fig. 3-03).

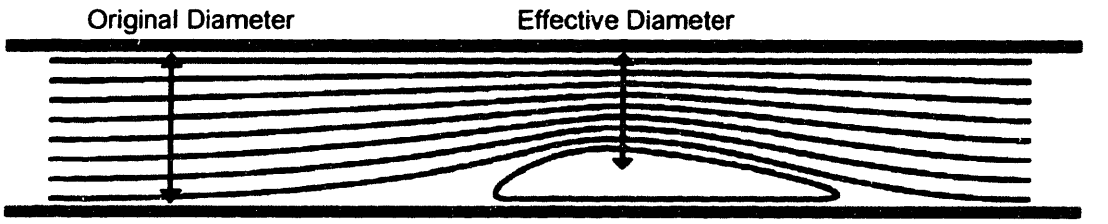

Figure 3-03: Effective Diameter in Tube with Boundary Layer Separation. Boundary conditions at the region of flow disturbance cause an elevated resistance to flow.

The boundary conditions imposed by the flow act in the same way as a physical wall with the effect of reducing the diameter and thus raising the resistance.

The value for the inertance is determined by the physical properties of the fluid, the setting of a pump that propels fluid through the system and the flow pattern itself. Thus, changes in the flow pattern could lead to changes in the inertance as well. However, as is often done with the Nelder-Mead technique and to increase the stability of the fit for the resistance, we assume here that the inertance remains constant despite changes in regions of flow separation in the branches of the bifurcation. This in turn limits the precision and utility of the fit for the resistance as will be discussed subsequently.

3.2.2. Experiment

The flow circuit was used to first validate the adequacy of the system function previously described and then to derive the free parameters (most importantly resistance) under different conditions.

3.2.2.1. Validation

To validate the mathematical model, the physical flow model was perfused and the differential pressure and flow rate were measured and subsequently low-pass filtered to

reduce noise with a cutoff frequency of 2Hz to include the first 20 harmonics. The waveforms were then used in conjunction with the difference equation that represents the system function in discrete domain to obtain a fit for the two free parameters R and I. This was accomplished by simulating the differential pressure waveform based on the flow waveform, and minimizing the total difference between the simulated and measured waveforms by varying the free parameters in a stepwise fashion using the Matlab command `fmins` which employs the Nelder-Mead simplex method. Once the best fit for R and I were obtained, these values were used to predict the differential pressure waveform from the flow waveform (see appendix B). The predicted waveform was compared to the measured waveform. A good agreement between the two demonstrates the ability to fit the data to a 2-parameter model.

3.2.2.2. Quantification of Boundary Layer Separation

Once the mathematical model was validated it could then be used to provide a semi-quantitative indication of the region of boundary layer separation in the main branch. Flow and differential pressure waveforms were acquired for different conditions simulating scenarios of progression of disease and adaptive optimization of the flow system (table 3-1).

Case	Daughter Vessel Constriction	Mother Vessel Geometry
1	None	Straight
2	None	Taper
3	Partial	Taper
4	Full	Taper
5	Full	Straight

Table 3-1: Experimental cases for quantification of flow separation. Cases 1-5 represent disease and optimization scenario.

For each flow condition, Fourier decomposition was performed for both the differential-pressure and flow-rate waveforms. The Fourier coefficients for the former were divided by the coefficients for the latter to provide impedance as a function of frequency. Based on the assumption that the contributions to this impedance come from resistance, which is

invariant with frequency, and inertance, the resistance was taken as the impedance at zero frequency. As outlined in the theory section above, changes in the resistance were taken to be a reflection of changes in the extent of boundary layer separation.

3.2.3. Results and Discussion

3.2.3.1. Validation

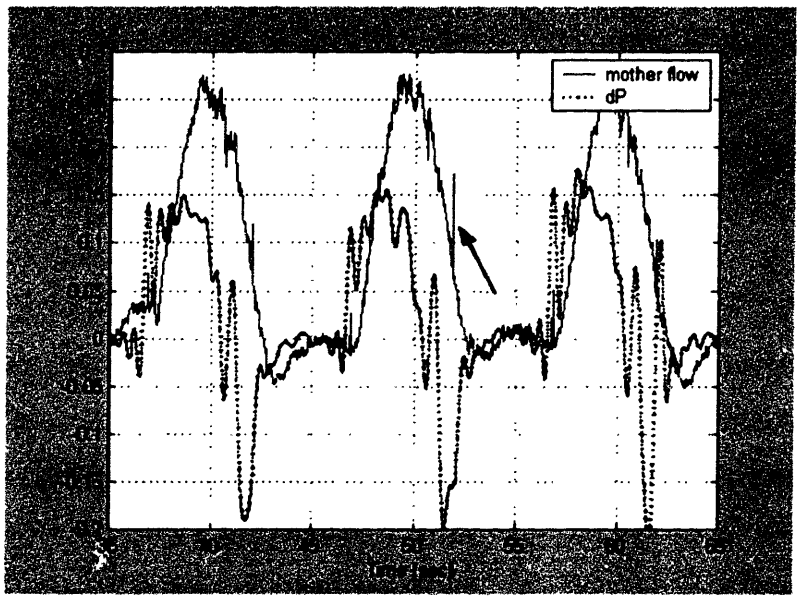

Figure 3-04: Waveform Acquisition. Simultaneous recording of the unfiltered flow and filtered differential pressure waveforms. The arrow points to the dicrotic notch in the flow waveform, which is manifested as an up-down-up deflection in the dP waveform.

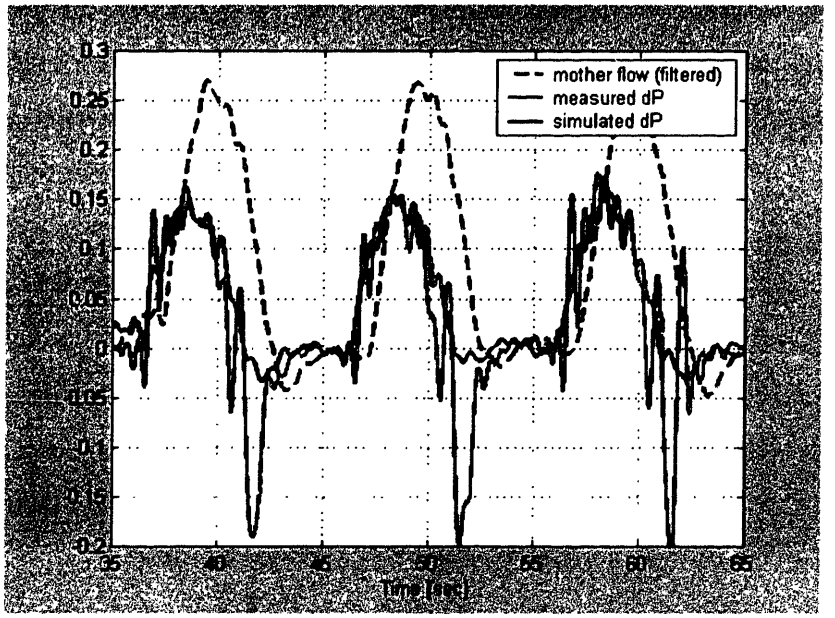

Figure 3-05: Waveform Simulation. Figure shows the filtered flow and dP waveforms as well as the dP waveform produced by the mathematical model. Note the disappearance of the dicrotic notch from the flow waveform as a result of filtering. Elsewhere, the measured and the simulated dP waveforms are in good agreement.

Simulation of the differential pressure waveform by passing the flow waveform through the system function (fig. 3-05) produced excellent agreement between the measured differential pressure drop and that predicted by the mathematical model. This included correlation, in phase and in magnitude, of local minima and maxima in both waveforms. The single exception to this was in mid-deceleration where the measured waveform had a characteristic up-down-up deflection that the predicted waveform did not follow. This error likely arises from the origin of the deflection. As can be seen in figure 3-04, the deflection in the pressure waveform corresponds in phase to the location of the dicrotic notch in the flow-rate waveform. Furthermore, the shape of the deflection in the pressure waveform is the theoretical response one would expect to the dicrotic notch. The response to any waveform is determined by the system function, which in this case is comprised of a linear combination of a multiplication by constant and a derivative with respect to time. The dicrotic notch is essentially an impulse function. The derivative of an impulse function consists of a sharp positive deflection, followed by a sharp negative deflection and a return to zero. The presence of just such a function in the differential

pressure waveform (fig. 3-04), further reinforces the assertion that the deflection in the differential pressure waveform is a result of the presence of the dicrotic notch. However, prior to performing the mathematical simulation that generated the predicted differential-pressure waveform, the flow-rate waveform was low-pass filtered to produce better behavior of the numerical filtering algorithm that is the system function. This low-pass filter removed all high-frequency components from the measured flow waveform signal, including the dicrotic notch itself that is comprised entirely of high frequency components. Thus, when the system function is imposed on the flow waveform to produce the predicted differential-pressure waveform, this flow waveform no longer includes a dicrotic notch. Accordingly, the predicted differential pressure waveform is missing the response to the dicrotic notch, which accounts for the discrepancy seen in figure 3-05.

3.2.3.2. Quantification of Boundary Layer Separation

The best fit for the resistance based on the system function (fig. 3-06), computed for the 5 flow model configurations described in table 3-1, shows how the resistance (in arbitrary units) of the main branch changes with changes in the geometry.

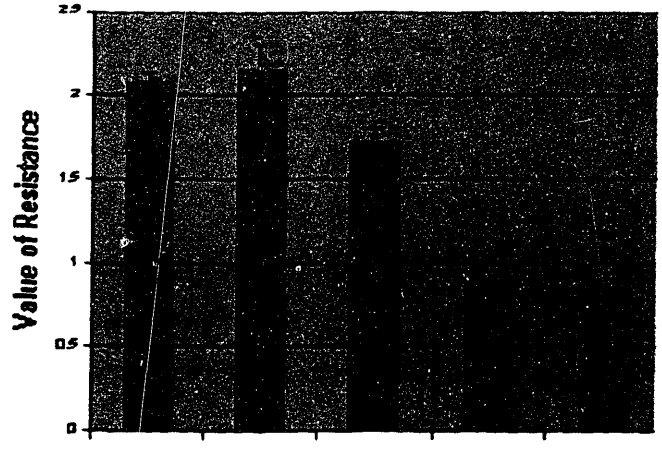

Figure 3-06: Quantification of Resistance. Values of main branch resistance, in arbitrary units, for cases 1-5 as calculated by best fit. The case number, main branch geometry and degree of side branch occlusion are given below the graph.

As expected, there is virtually no change in the resistance from case 1 to case 2, despite the reduction in the diameter of the mother vessel between these two cases. The lack of effect on resistance is consistent with the theoretical prediction that a part of the cross-section of the main vessel in case 1 was taken up by a region of boundary layer separation (see fig. 3-03). Thus, while the physical diameter of the vessel was reduced in case 2 when a taper was induced on the mother vessel, the effective diameter for flow did not change, keeping the resistance nearly constant.

As progressive constriction was imposed on the side branch in cases 3 and 4, a marked reduction in the resistance of the main branch was observed, despite no change in the geometry of the main branch. Once more, this is consistent with the theoretical model that attributes a part of the resistance in the main branch to boundary layer separation induced by the presence of the side branch. As flow into the side branch was reduced, the region of flow separation in the main branch decreased and the resistance dropped.

Case 5 differed from case 4 in that the gradual taper in the main branch opposite the ostium of the side branch was now removed. At this point, flow was essentially through one straight channel. On theoretical grounds, the resistance would be expected to decrease further, and yet this was not the case. The resistance in case 5 was almost identical to case 4 (fig. 3-06). A possible explanation for the lack of change in resistance here lies in the method in which the differential pressure measurement was performed. Absent boundary layer separation, a rough estimate of the expected effect of removing the taper can be achieved using the Haggen-Poiseuille equation. When the flow rate in this equation was set to the mean flow rate of the pump, the calculated pressure drop over 4 diameter lengths for a straight segment would only be 0.01 mmHg lower than that of a vessel with a 10% taper. In contrast, the differential pressure sensor measured a total pressure drop across the entire model on the order of 1 mmHg. Hence, the pressure drop from the taper was only a small component of the total pressure drop measured. The small pressure drop creates two problems: a low signal to noise ratio, and more importantly, the presence of the major part of the pressure drop elsewhere in the model. A likely site for this pressure drop is in the connectors that interface the pressure tap into the flow circuit, as well as the interface of the glass pieces that connect the external

tubing to the silicone channels. The pressure drop at these sites is most likely affected by any change in the flow patterns thus masking the effect in the region of interest.

3.3. Flow Visualization – Large Side Branch Model

Visualization of flow involves description of the shape and attributes of the flow velocity field. Many methods exist for this purpose including the simple injection of dye into the flow stream, creation of small hydrogen bubbles, introduction of smoke, tracer particles or other types of streamers etc. Other more elaborate methods include laser Doppler anemometry (LDA), which utilizes coherence of laser beams to measure precise instantaneous velocities at a point, as well as particle image velocimetry (PIV), which tracks the flow to produce a vector field.

3.3.1. Theory

The optimal mode of visualization for each situation is determined by the properties of the model and/or flow. In our case, the determining characteristics were:

a) Pulsatile flow. Hence dyes and other types of streamers are ineffective as these fill up the entire cross-section when the flow is at its stationary point in the cycle.
b) Material properties. The materials and methods by which the flow model was built are not well suited for analysis using laser beams that require optical purity.
c) Scale. The scale of the model was such that small tracer particles could not be used without zooming in to a level that did not allow viewing of the entire region of interest in one frame.
d) The scale and material required precise diffuse lighting and so methods that rely on high definition optics (most PIV) were not well suited for this model.

Given these considerations, two methods for flow visualization of the models were adapted specifically for use here. These two methods give complementary views of the flow field that can be used simultaneously to get an overall qualitative description of the properties of flow.

3.3.1.1. Visualization of Streamlines

Visualization of streamlines involves using the tracer particles described previously to obtain a semi-instantaneous image of the streamlines of flow. The model was perfused

and filmed using the digital video camera at 30 frames per second. Neutrally buoyant tracer particles (see section 2.3.1) were injected into the flow via the proximal injection port. The particles were not suspended in the perfusing fluid itself so as to maintain a high particle concentration inside the model itself. A digital video image was acquired, stored on the computer and synchronized to the waveform analysis. A 32-frame, approx. 1 second segment of the video for which visualization was to be performed was identified using the waveform analysis. The segment was split into 64 still-frame images. The images were enhanced to produce maximal contrast between particles and background, and each of 16 pairs of successive images used to produce a difference image using the `image→calculations→difference` command in Adobe Photoshop. This was repeated for these 16 difference images in a binary tree fashion. The outline of the bifurcation was drawn onto the image using one of the original 32 images to detect the edges.

This method produces an image that is composed of each one of the original particles at 32 successive positions and thus represents the paths these particles take. Strictly speaking, these paths are what are know as 'streaklines' rather than 'streamlines' i.e. they describe particle paths rather than instantaneous velocity fields. However, if the particle density is high enough, and the image is limited to a short period in time compared with the length of an entire cycle (in this case, there is a difference of approx. an order of magnitude), then these lines represent the instantaneous streamlines at the point in the cycle that they were taken. Furthermore, since the length of each line represents the velocity of the particle that produced it, this method actually provides a hybrid representation comprised of not only information about the direction but also the magnitude of the velocity vector field.

3.3.1.2. Particle Image Velocimetry

The particle image Velocimetry (PIV) used in this study was adapted from an algorithm developed by Douglas P. Hart at the department of mechanical engineering at MIT. This program is described in a paper by D.P. Hart[53] and is available for download from his website at: http://web.mit.edu/dphart/www/Program.pdf. Like all PIV algorithms, this program employs a correlation between the particle locations in two images to deduce the

vector field that produced the translocation of these particles. The algorithm also employs bilinear interpolation to fill in the spaces between tracked particles with appropriate velocity vectors. The primary limitation to using this program to obtain vector images in the present models is that the program's effectiveness is highly dependent on the particle concentration. To achieve a high particle concentration in the present models, particles on the order of tens of microns in diameter need to be used. While these particles can easily be fabricated, capturing a clear image of them with the video camera requires either a very high-resolution camera, or elaborate lighting. To escape these issues, large particles on the order of hundreds of microns to a millimeter were used. This however dictates that the number of particles that can be injected at a time and hence the number of particles per image field is low, producing poor results with the PIV algorithm.

To overcome this problem we employed a method that exploits the repetitive pulsatile nature of the models to raise the apparent particle density in the image field. As in the streamline method the model was perfused and filmed using the digital video camera at 30 frames per second. Tracer particles were injected into the flow via the proximal injection port. The digital video image was acquired, stored on the computer and synchronized to the waveform analysis. A phase in the flow waveform was chosen to perform the visualization. This typically was the point of maximal velocity, mid-acceleration or mid-deceleration. Two cycles (not necessarily successive) that had a relatively high particle density were selected. For each cycle, six successive still images at the selected phase were produced and enhanced to provide maximal contrast (see section 2.3.3). For the purpose of this procedure we labeled these images 0 thru 5 (fig. 3-07). Using Adobe Photoshop, image 4 was copied and pasted onto image 0. Using the `magic wand` tool, the background on the image 4 layer was selected and then cleared. The same procedure was followed for images 1 and 5. Thus, we were left with two "successive images" that contained twice the normal particle density each, although the second layer of particles was close to the first layer of particles thus in reality the particles in each image were effectively doubled. This procedure was repeated for the second cycle.

The first and second of the successive images for each cycle were combined using the same technique to ultimately produce two composite images one frame apart which had four times the density of particles as the original images. The entire procedure is illustrated in fig. 3-7.

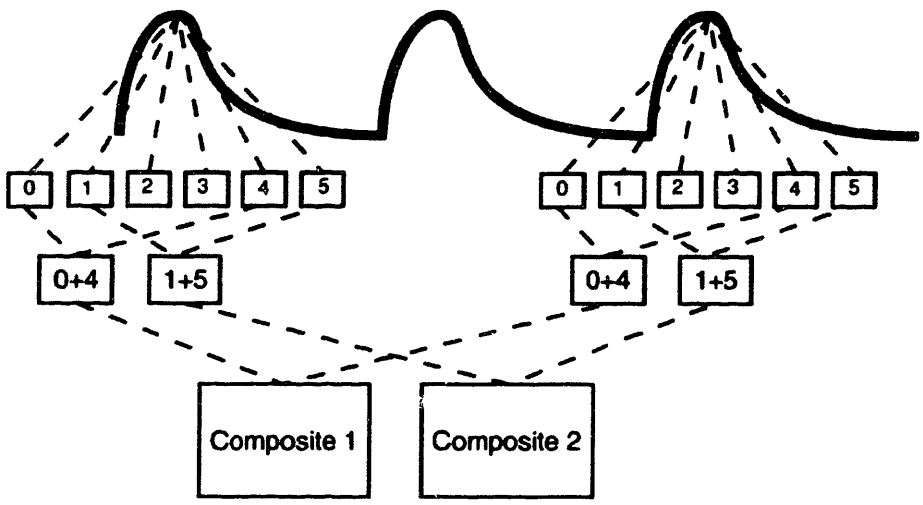

Figure 3-07: Scheme for Creating Composite Images for PIV. Frames 0 thru 5 in each cycle are successive. Composites contain four times the particle density of original frames.

Once the two composite images were obtained, the normal particle image velocimetry program was run using the following parameters:

Primary Correlation Window Size = 32

Sub-Correlation Window Size = 32

Compression Pixel Number = 32

Maximum Search Length = 8

Max. Dev. = 8

√ Fill Voids √ Smooth Data √ SPCorrection

The output was then displayed at a velocity scale of 8[xii]. The output image was copied and pasted into Adobe Photoshop where it was cropped and enlarged to the original 720X480 resolution of the DV camera. An image of the boundaries of the bifurcation, obtained using the original frames, was superimposed onto the image. Vectors

[xii] For an explanation of the meaning of each one of these parameters, see the help file in the software package.

occasionally fell outside of the boundaries because of the interpolation scheme and were deleted from the final vector field map.

Despite attempts at overcoming the difficulties in employing PIV within these models, ultimate particle concentrations were marginal at best. One common site of inaccuracy was close to the lateral model walls (particularly in the main branch) where particle counts were particularly low. The PIV algorithm used employs a bilinear interpolation scheme in regions where particles cannot be identified. Thus, the forward motion around the centerline of the vessel was interpolated down to zero at the vessel wall without showing the reverse flow expected in a region of boundary layer separation. Perhaps the best demonstration of the inaccuracy of these results is the fact that some of the images clearly violate conservation of mass in that the sum of the fluid fluxes in the two branches does not equal the flux in the entrance segment. For these reasons, the reliability of the PIV data cannot be established beyond any doubt, and in this thesis these data will only be presented supported by streamline images. If PIV is to be used in the future for this type of work, significantly higher particle concentrations will have to be used, which will in turn require the use of sophisticated imaging and lighting techniques.

3.3.2. Experiment

The goal of the flow visualization experiment was to provide qualitative descriptions of the flow field in the bifurcation under different conditions. These descriptions would serve to provide evidence in support of the hypothesis of interactions between the side branch and main branch, as well as provide a basis for the *in-vivo* experiments.

3.3.2.1. Experimental Scenario

The experimental scenario (see section 1.6) was simulated in several cases, distinct from those described previously (table 3-1), where each case represented a change in one geometric parameter of the model. These cases are outlined in the table 3-2 below. Lesions in the daughter vessel were simulated by reduction of flow using the downstream resistance.

Case	Main branch geometry	Side branch flow[+]	Collateral flow[+]
6	Constant diameter	93%	None
7	Tapered[*]	95%	None
8	Tapered[*]	61%	None
9	Tapered[*]	17%	None
10	Tapered[*]	8%	25%
11	Constant diameter	93%	36%
12	Medium Lesion	No lesion	None
13	Large Lesion	No lesion	None

[+] Percent of main branch flow

* 1-2 degrees

Table 3-2: Cases for scenario simulation.

Note: Daughter vessel flow in case 10 was affected by both the lesion and the re-distribution of flow from the introduction of collateral and hence does not reflect the extent of the lesion alone. The extent of the lesion on the side branch was similar to that of case 9.

The two methods for flow visualization detailed above were performed for each case. PIV was performed at end acceleration. Streamline visualization was performed at approx. 2/3 of the maximal velocity both during the acceleration and the deceleration phases. The results were then compared on a case-by-case basis.

3.3.2.2. Temporal Development of Boundary Layer Separation

The model was fixed in the geometry described by case 6 in table 3-2 above, i.e. a straight mother vessel, no lesion in the daughter vessel and no collateral flow. PIV was performed at the point of maximal flow velocity, and one second later during mid-deceleration. The two results were compared to see how the flow field develops over time during the deceleration phase.

3.3.3. Results and Discussion

3.3.3.1. Experimental Scenario

For each one of the cases outlined above (table 3-2) a figure is provided showing the following four results:

1. A sample of the waveform representing one cycle. Circles denote the instants of the flow visualization. A dashed circle denotes the PIV, a single circle denotes streamlines at acceleration and a double circle denotes streamlines at deceleration.
2. PIV result.
3. Streamlines at acceleration.
4. Streamlines at deceleration.

The caption for each one of these figures identifies the three components that define the specific case of the experiment: main branch geometry (straight, tapered or lesion), side branch flow (see table 3-2) and collateral flow (see table 3-2). The parameter that has been altered from the previous case in the figure in question is underlined.
Following each one of these data sets is a discussion of the important aspects of flow that can be identified in the figures, and a comparison is made with the previous sets.

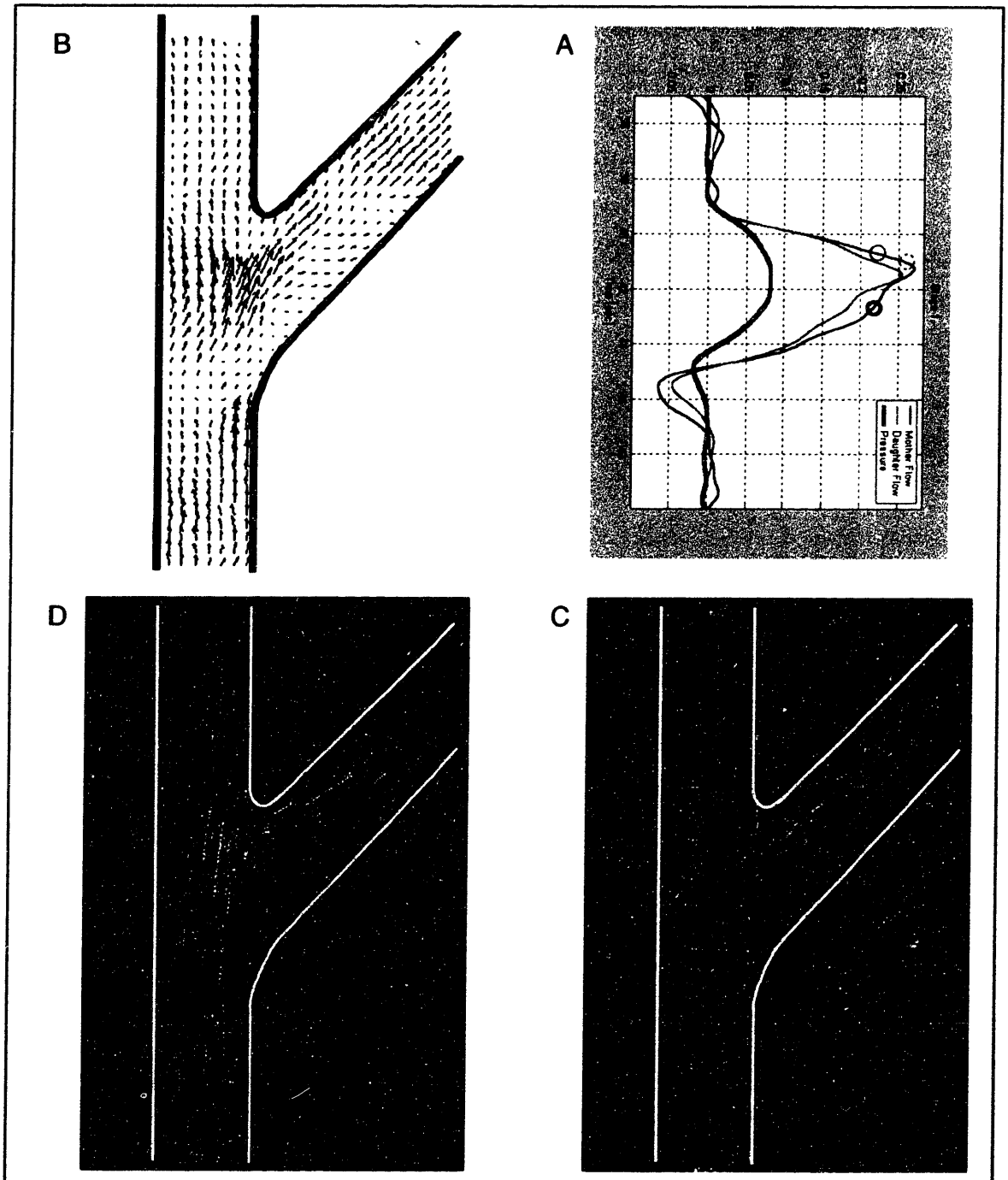

Figure 3-08: Case 6 Visualization. Main Branch: Straight, Side Branch flow: 93%, Collateral flow: 0. (A) Waveform: Dashed circle: PIV, Single circle: Streamlines at acceleration, Double circle: Streamlines at deceleration. (B) PIV. (C) Streamlines at acceleration. (D) Streamlines at deceleration.

The waveform plot (fig. 3-08A) shows the general characteristics typical of flow rate through most arteries. There is a sharp period of acceleration, followed by a small decrease in velocity, a plateau phase and a deceleration down to zero velocity, followed by a period of low to zero flow of length approximately equal to that of the flow cycle. Note the appearance of net flow reversal as indicated by a negative velocity in both the mother and the daughter branches. This flow reversal correlates with a period of what appears to be negative pressure. This negative pressure is not an actual vacuum, as liquids are incapable of sustaining a true vacuum, but rather a drop in the pressure to below the hydrostatic pressure at the flow sensor location that is used to determine the zero pressure point.

Particle image velocimetry (fig. 3-08B) clearly shows both regions of flow disturbance[xiii]. The first prominent region is located in the ostium of the side branch on the lateral wall. Vectors in this region are short indicating low flow velocities and low shear stress. The vectors immediately adjacent to the wall are in fact reversed, indicating the re-circulation of fluid that occurs in the region of boundary layer separation. The second region of disturbance can be seen in the main branch on the lateral wall opposite from the ostium of the side branch. The presence of disturbed flow is clearly indicated by the curvature of the direction of flow indicated by the vectors – first away and then back towards the artery wall. Flow in the central region of the bifurcation leading towards the flow divider can be seen to accelerate. This will eventually become the region of high shear predicted to occur adjacent to the flow divider walls. In this image, this high shear can be seen next to the side branch angle of the flow divider. The main branch angle of the flow divider does not exhibit particularly high shear in this image, most likely from practical limitations of the modeling, namely absence of particles in that specific area in the images used to produce the PIV.

Streamline images (fig. 3-08C, 3-08D) show the same general phenomenon observed in the PIV image. Both regions of flow separation can clearly be made out by the curvature of the streamlines and the presence of very short streamlines inside, which indicate low

---

[xiii] While the term 'disturbance' is most commonly used to refer to transitional or turbulent flow, here it shall be used to denote regions of slow flow, suggesting the possibility of flow reversal.

flow velocities and low shear stress near the wall. The region of separation in the side branch is more rounded and confined whereas the separation in the main branch is flatter and more elongated. This might explain why in the PIV image no flow reversal can be detected adjacent to the wall in the mother vessel. As opposed to the PIV, the high shear region adjacent to both angles of the flow divider can now clearly be seen, especially in the deceleration picture, as indicated by very long streamlines corresponding to high velocities that nearly hug the flow divider walls.

Comparison between the acceleration (fig. 3-08C) and deceleration (fig. 3-08D) images provides further insight into the patterns of flow and separation. Despite the fact that the mean velocities are the same in both cases, the regions of flow separation are entirely different in shape. In general, both regions of separation are substantially more pronounced in the deceleration phase than in the acceleration phase. Thus during deceleration, there is a shift of flow away from the lateral walls and towards the flow divider. This shift is also evident if one observes the difference in length of streamlines next to the flow divider between these two phases of flow. While both regions of separation increase in size from acceleration to deceleration, this is much more pronounced in the side branch than in the main branch. Thus, one would expect the relative resistances of these two vessels to change as the flow bypasses the stagnant zone. This can be observed in the flow waveform (fig. 3-08A) as the fact that despite the equivalence of flow rates in the mother vessels (as indicated by the two solid circles), the flow rate in the daughter vessel was lower during deceleration than during acceleration. This reduction can be explained entirely by the shift in relative resistances as growth of the regions of separation diverts flow from the daughter vessel towards the mother vessel during the deceleration phase of flow.

Lastly, combining all three flow images highlights another interesting result. As indicated by the circles denoting the timing (fig. 3-08A), the chronological order of these three figures is 3-8C→3-8B→3-8D. Focusing on the location of the region of separation in the main branch, in particular the proximal end (the point of separation), one can see that the region grows in the proximal direction during the entire cycle.

The general features described in the discussion of this first case are evident in the results for all other cases defined in table 3-2. In what follows, the results for these other cases

are presented in the same format and the discussion will focus on the differences between one case and another.

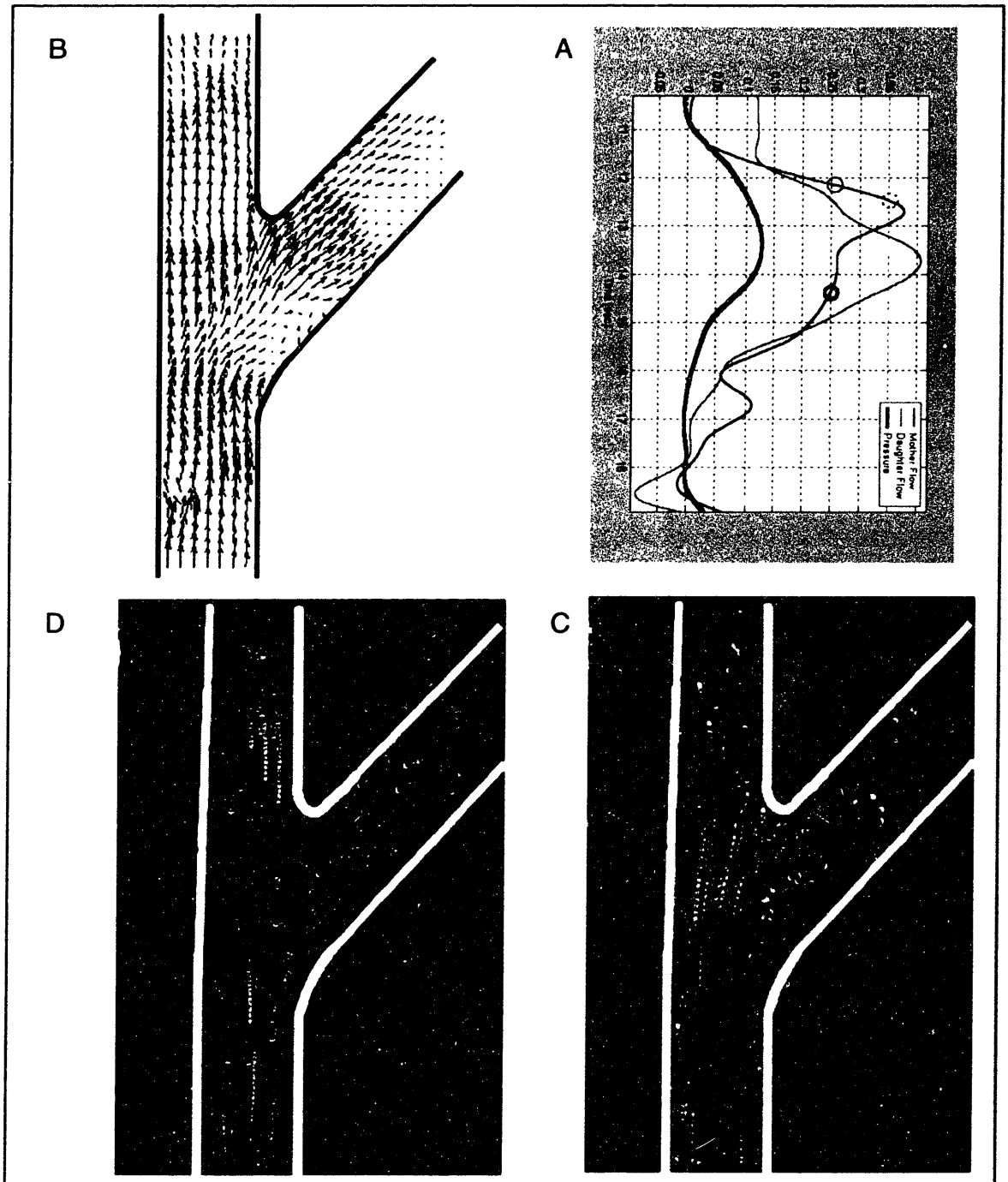

Figure 3-09: Case 7 Visualization. Main Branch: Taper, Side Branch flow: 95%, Collateral flow: 0. (A) Waveform: Dashed circle: PIV, Single circle: Streamlines at acceleration, Double circle: Streamlines at deceleration. (B) PIV. (C) Streamlines at acceleration. (D) Streamlines at deceleration.

The gradual taper of the mother vessel produced a waveform plot (fig. 3-09A) of the same general characteristics as for a straight vessel (fig. 3-08A) with two qualitative differences worth consideration. First, the taper produced a phase shift between the flow rates in the mother and daughter vessels, with the daughter lagging the mother vessel waveform by approx. 20% of the cycle length. This phase shift is analogous to the clinical phenomenon of delayed dye clearance in angiographic images of obstructed arteries. Second, taper eliminated the component of flow reversal in the mother vessel seen in the straight vessel waveform (compare to fig. 3-08A) and the corresponding phase of negative pressure. PIV (fig. 3-09B) clearly supports the theoretical prediction for flow in this tapered geometry: While separation in the side branch is clearly evident, including a prominent aspect of reversal, there is no disturbance in the main branch. Instead, the vectors are parallel to the wall along the entire length of the tapering vessel. As before, high shear can be seen to exist adjacent to the flow divider, particularly in the side branch angle. The streamline images (fig. 3-09C&D) confirm the same observations seen in the PIV. The separation on the lateral wall of the side branch is obvious in the acceleration phase. There appears to be a slight residual separation in the main branch in fig. 3-09C, however comparison of the length of streamlines adjacent to the walls between this image and fig. 3-08C clearly shows that there is significantly higher shear stress in the tapered vessel than in the non-tapered one. Finally, the deceleration streamline image (fig. 3-9D) provides further evidence of the phase shift between mother and daughter vessel flows noted above. While flow in the main branch is clearly decelerating at this point, most of the flow now seems to be entering into the side branch. This finding was also seen in real-time video (not shown here). This could be no more than a result of inaccuracies in the imaging, e.g. poor distribution of tracer particles in the image. However, coupled with the result seen in the waveform image (fig. 3-9A), it is likely that this effect is real.

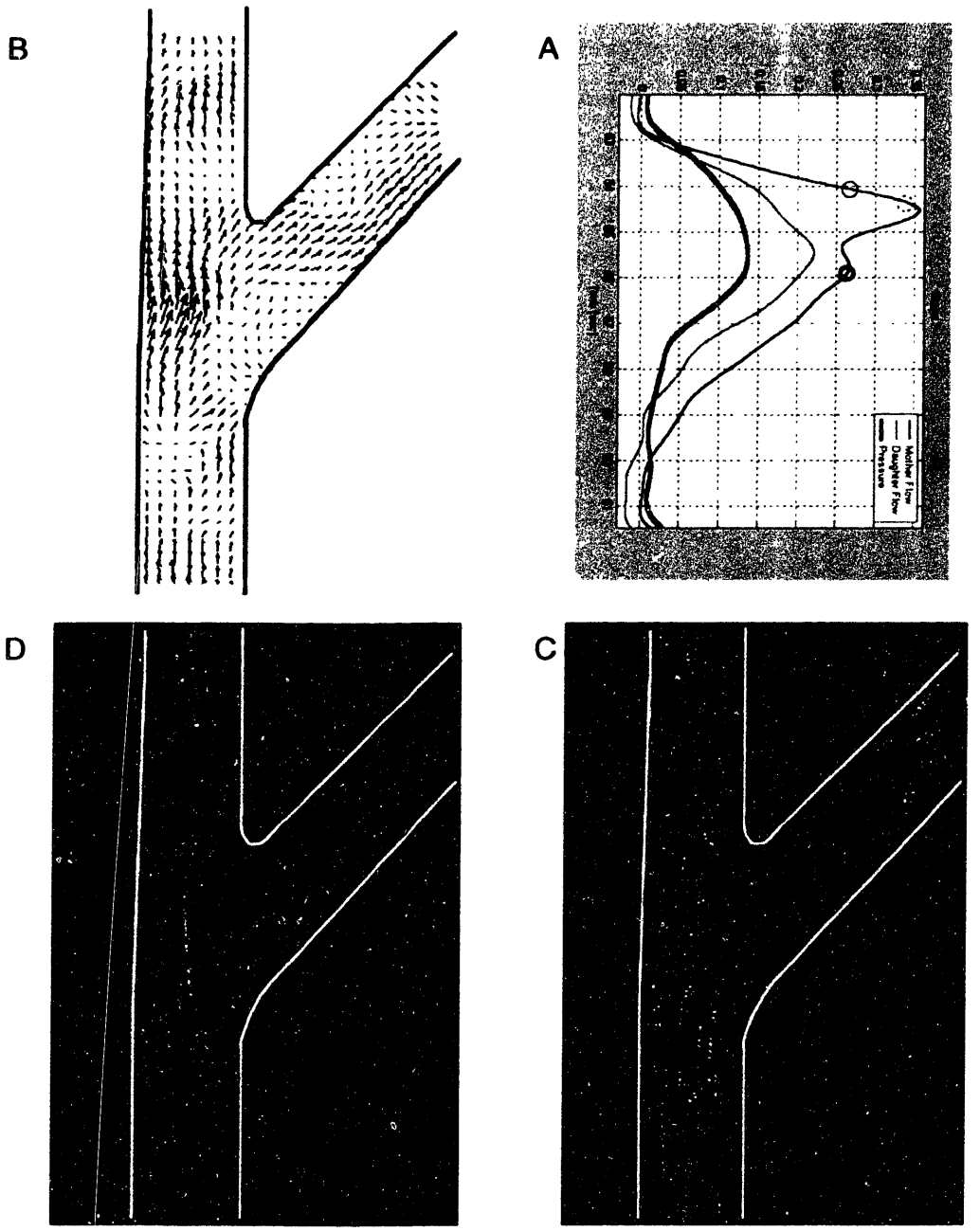

Figure 3-10: Case 8 Visualization. Main Branch: Taper, Side Branch flow: 61%, Collateral flow: 0. (A) Waveform: Dashed circle: PIV, Single circle: Streamlines at acceleration, Double circle: Streamlines at deceleration. (B) PIV. (C) Streamlines at acceleration. (D) Streamlines at deceleration.

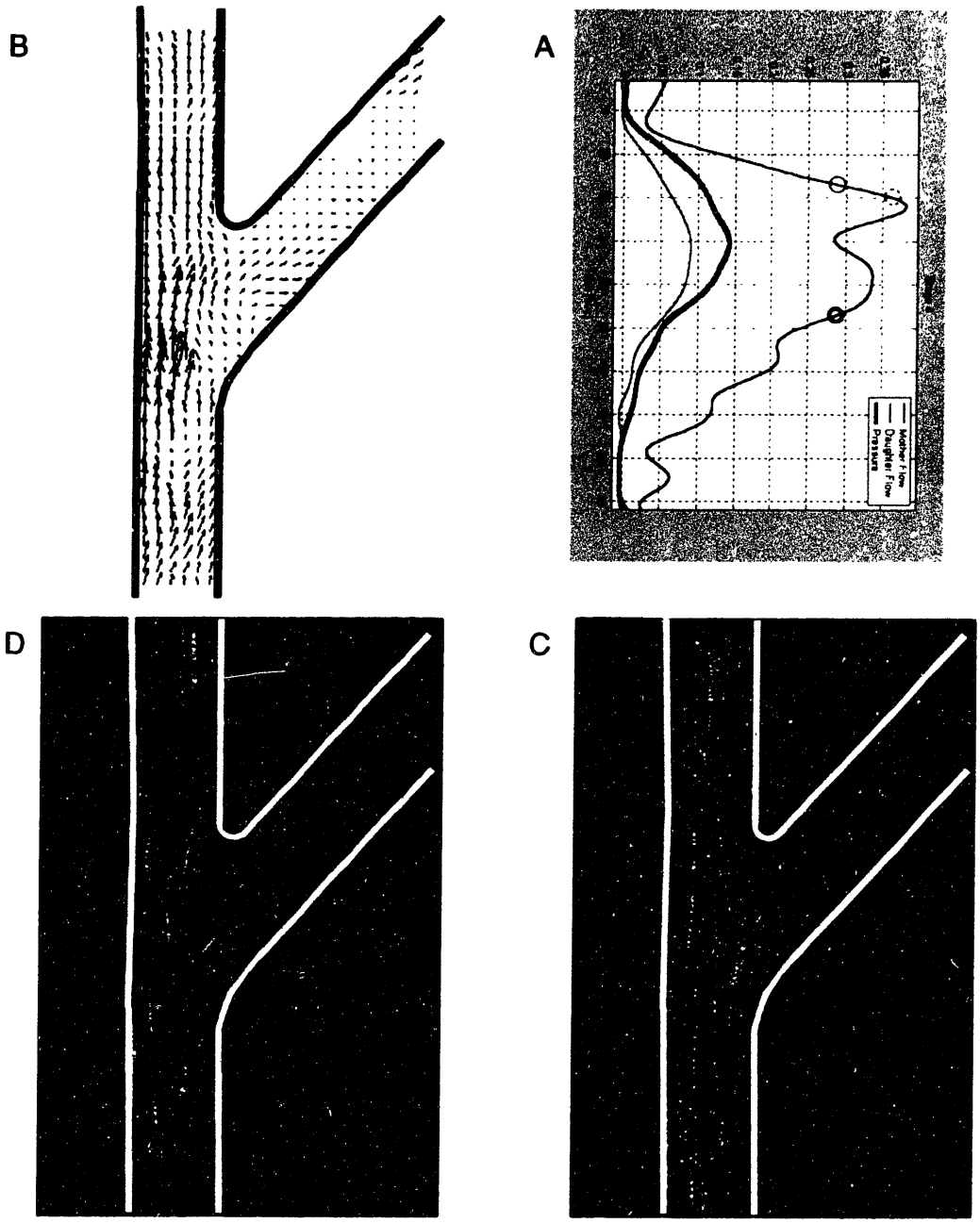

Figure 3-11: Case 9 Visualization. Main Branch: Taper, Side Branch flow: 17%, Collateral flow: 0. (A) Waveform: Dashed circle: PIV, Single circle: Streamlines at acceleration, Double circle: Streamlines at deceleration. (B) PIV. (C) Streamlines at acceleration. (D) Streamlines at deceleration.

Case 8 represents a modest reduction in total flow into the side branch (61% of main branch flow), and case 9 represents a drastic reduction in total flow into the side branch (17% of main branch flow). Qualitatively, these are two points along a spectrum and thus they will be discussed jointly here. The waveforms (figs. 3-10A, 3-11A) once more show no evidence of flow reversal or negative pressures. Additionally, there is a change in the plateau phase of the mother branch flow rate waveforms. As the flow in the side branch was reduced, first modestly in case 8 and then drastically in case 9, the plateau pressure increased until it became a discrete peak (fig. 3-11A). The origin of this new peak can be attributed to the phase lag that was demonstrated between the main branch and side branch flow waveforms (see fig. 3-09A and subsequent discussion of case 7). Since the pump output was held constant throughout all cases of this experiment, as the flow rate in the side branch was decreased, (figs. 3-10A and 3-11A) the excess flow, in the absence of collaterals, was added to the main branch flow waveform. Since this excess is at a phase lag with the original main branch flow, the effect of this added flow was to create a second peak that increased in amplitude as more and more flow was diverted from the side branch. Not unexpectedly, PIV (figs. 3-10B, 3-11B) showed progressively decreasing velocities into the side branch (compare vector lengths in the ostium from fig 3-9B to 3-10B and then 3-11B). While there is still some deviation of the vector alignments in the main branch (fig. 3-10B) accounted for by the non-zero flow into the side branch, for the most part and especially in fig. 3-11B, flow in the main branch is nearly axial laminar flow as would be expected in a simple straight tube. Streamline images once more show the reduced flow velocities into the side branch (compare length of lines in figs. 3-10C and 3-11C to fig. 3-9C). Additionally, the region of boundary layer separation in the side branch in these two cases is reduced in size. This is likely from the slower flow rates, and hence, inertia of the fluid coming around the lateral angle and into the side branch. Separation in the main branch was nearly eliminated in the modest flow reduction case (fig. 3-10C) and disappeared entirely in the drastic flow reduction as evidenced by the streamlines in fig. 3-11C that have no curvature towards the lateral wall at all.

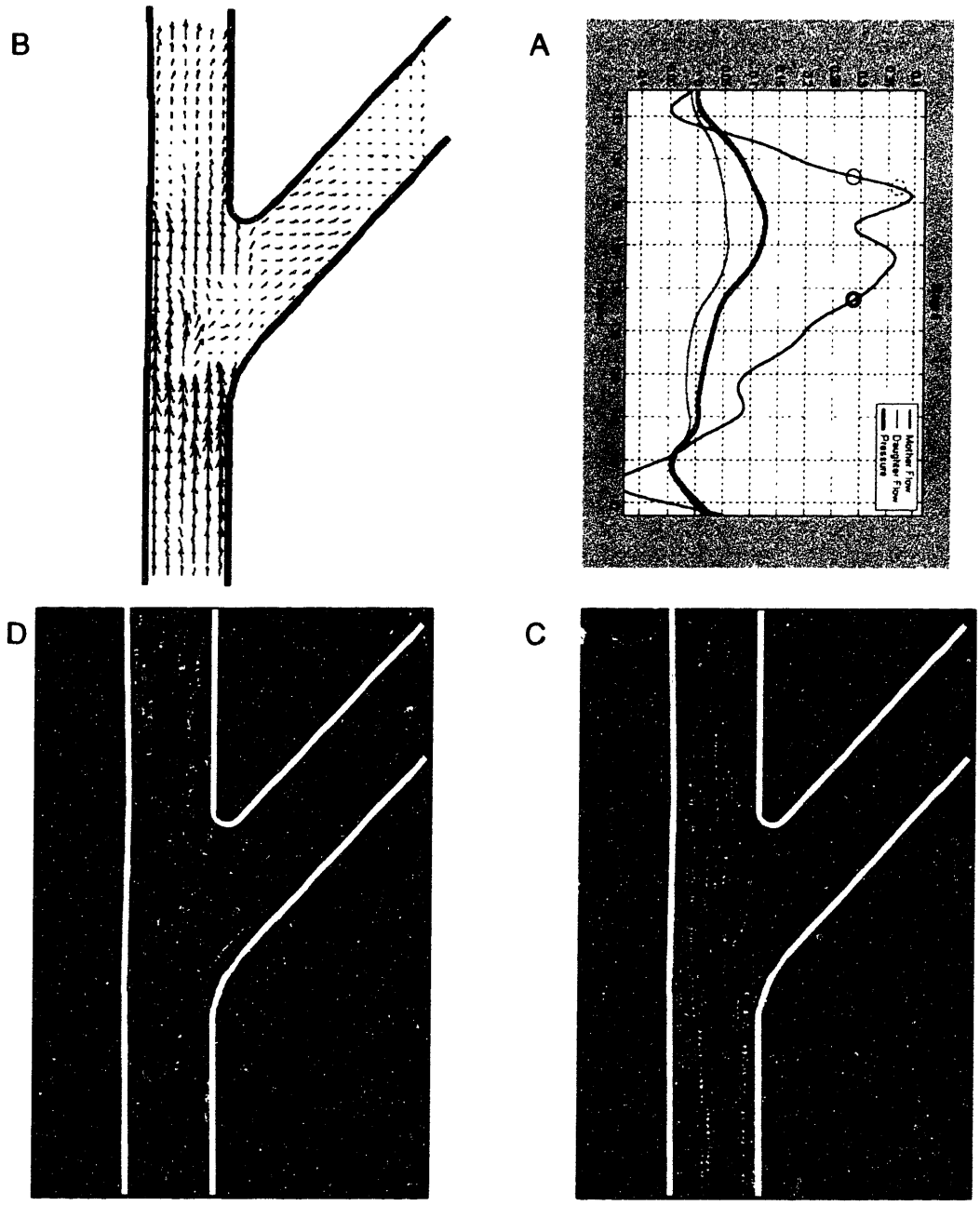

Figure 3-12: Case 10 Visualization. Main Branch: Taper, Side Branch flow flow: 8%, Collateral flow: 25%. (A) Waveform: Dashed circle: PIV, Single circle: Streamlines at acceleration, Double circle: Streamlines at deceleration. (B) PIV. (C) Streamlines at acceleration. (D) Streamlines at deceleration.

The introduction of collateral flow in this geometry had very little effect on the shape of the flow patterns, as can be seen by comparison of the PIV images (figs. 3-11B, 3-12B) and of the streamline images (figs. 3-11C, 3-11D, 3-12C, 3-12D), despite the nearly 25%

of the total pump output that was flowing through the collateral vessel. The length of the streamlines in figs. 3-12C, 3-12D is shorter than that of 3-11C, 3-11D in accordance with the reduced total flow entering this segment, yet the qualitative shape of flow remains unchanged. This observation is in fact meaningful, in that it shows that the qualitative shape of the streamlines through the bifurcation segment is relatively invariant with respect to the total flow coming into the proximal end. Hence, as long as one is interested in the qualitative aspects of flow and not precise absolute values, the experiment is not sensitive to a precise determination of the input flow, which is difficult to attain in the prototype because of practical limitations (see section 2.4.1).

Inspection of the waveform (fig. 3-12A) and comparison with the previous case (fig. 3-11A) shows that a reduction in flow occurs in both the side branch and the main branch. In other words, the collateral vessel "steals" flow from both vessels. The amount of steal can be predicted from the simple electrical analogy (fig. 3-13).

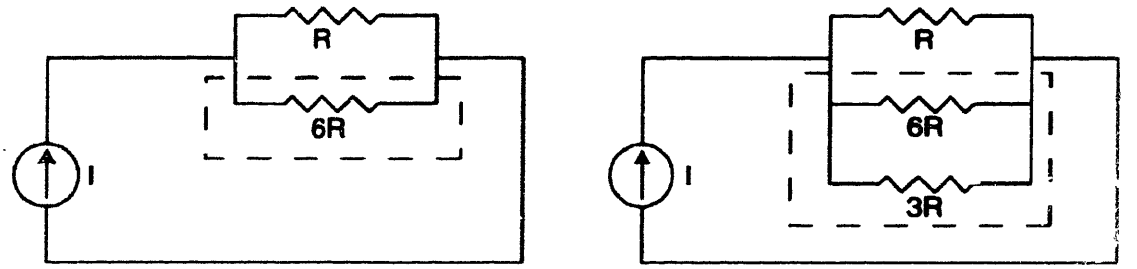

Figure 3-13: Collateral Steal. Left panel shows circuit analogy prior to development of collateral. High resistance represents lesion in the side branch. Right panel shows analogy for development of collateral vessel. The regions in the organ perfused by the dashed boxes are the same.

The prediction gained from this model was compared to the integrated flow in the two vessels. These two values were consistently within 2% of each other, demonstrating that, for the purposes of this analysis, the simple electrical analogy is highly accurate. The reason this simple analogy works so well in this case is that as mentioned before with respect to the streamline images, the flow patterns themselves do not change with the introduction of collateral flow, hence the channels can be treated as simple invariant resistors.

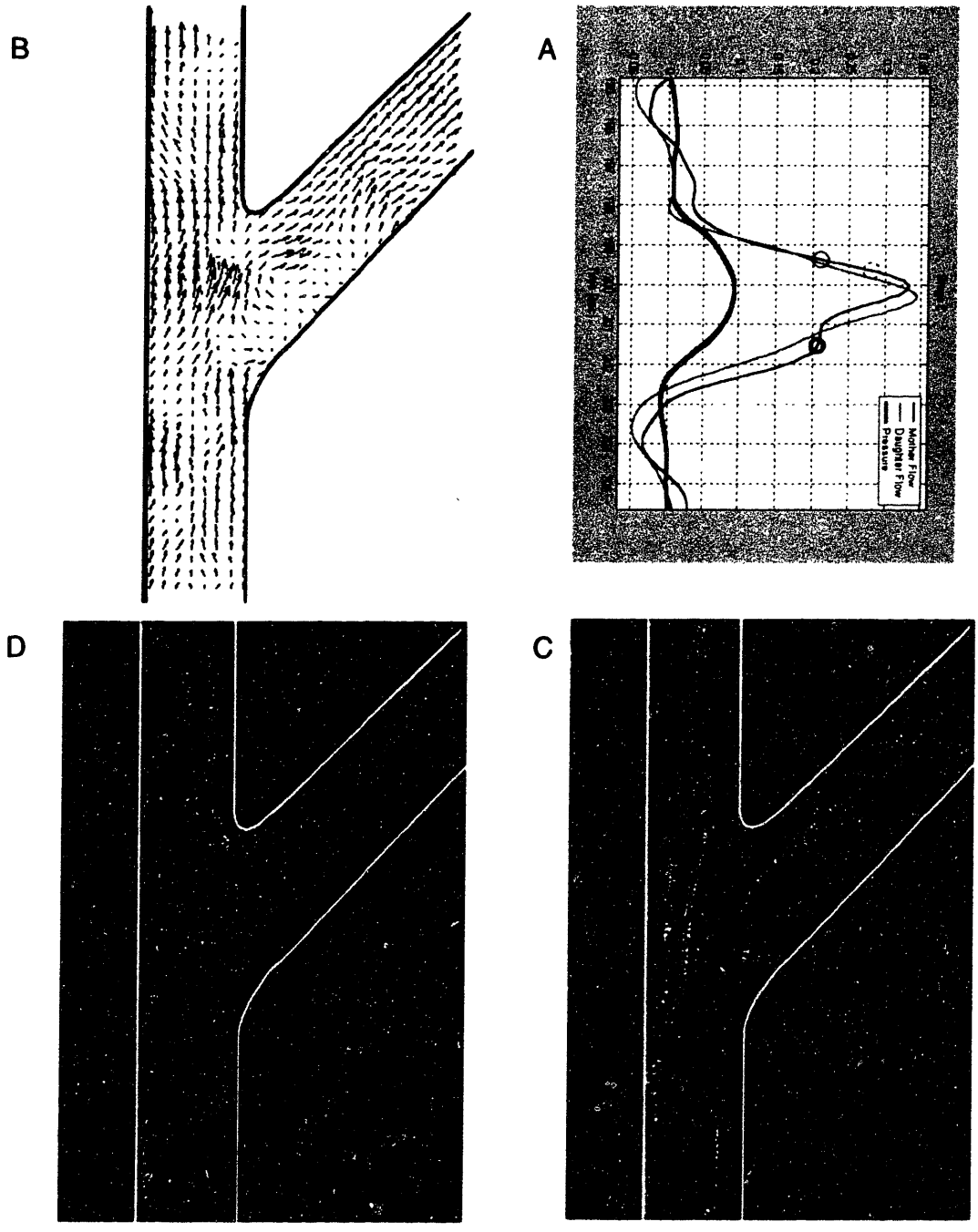

Figure 3-14: Case 11 Visualization. Main Branch: Straight, Side Branch flow: 93%, Collateral flow: 36%. (A) Waveform: Dashed circle: PIV, Single circle: Streamlines at acceleration, Double circle: Streamlines at deceleration. (B) PIV. (C) Streamlines at acceleration. (D) Streamlines at deceleration.

Reopening of the side branch in case 11 created a geometry that was similar in many respects to the constant diameter main branch with a patent side branch (case 6), except for the existence of a substantial element of collateral flow. Examination of the waveform image (fig. 3-14A) shows the same general properties as those observed originally in fig. 3-08A. These include a plateau in the deceleration phase of the flow wave, as opposed to a discrete second peak, as well as flow reversal at the end of deceleration in both the mother and the daughter branches. Also present is the negative component in the pressure waveform, although it is somewhat smaller in fig. 3-14A than in fig. 3-8A. It is unclear whether this reduction in the negative component is from a real effect caused by the presence of collateral flow, or to intrinsic fluctuations that exist in all of the experimental waveforms. The PIV image (fig. 3-14B) shows the expected flow separation in the side branch, and re-establishment of a large region of flow disturbance in the main branch. The extent of this latter region of disturbance is substantially larger both in the axial and in the radial directions than that seen in the straight vessel with intact side branch flow (compare with case 6 fig. 3-8B). The differences can only be attributed to the presence of collateral flow, the single geometric parameter altered between these two cases, and can be understood if one takes into account the reduced inertia of the flow in the main branch, from take-off of flow into the collateral. Such a reduction would allow easier and more extensive diversion of the streamlines from the axial direction. Streamline images provide further evidence of the above-mentioned growth in separation from case 6. The point of stagnation, the proximal end of the region of flow separation, is further proximal in fig. 3-14C than in fig. 3-8C, extending now even more proximally than the ostium itself. Comparison between the deceleration phases (figs. 3-14D, 3-8D) shows the growth in the radial direction of the region of separation, which now extends to well beyond the centerline of the mother vessel.

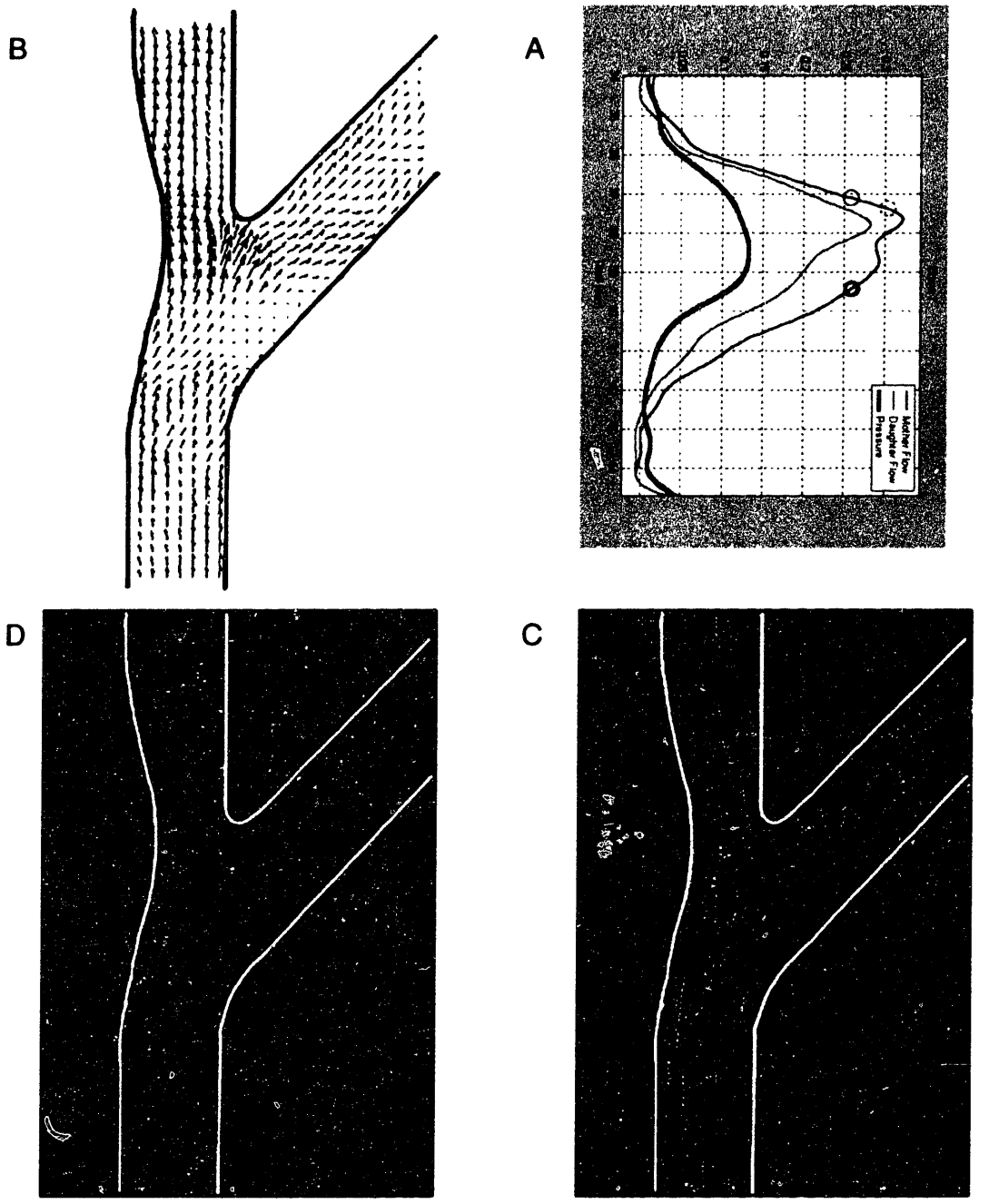

Figure 3-15: Case 12 Visualization. Main Branch: Lesion, Side Branch flow: 90%, Collateral flow: 0. (A) Waveform: Dashed circle: PIV, Single circle: Streamlines at acceleration, Double circle: Streamlines at deceleration. (B) PIV. (C) Streamlines at acceleration. (D) Streamlines at deceleration.

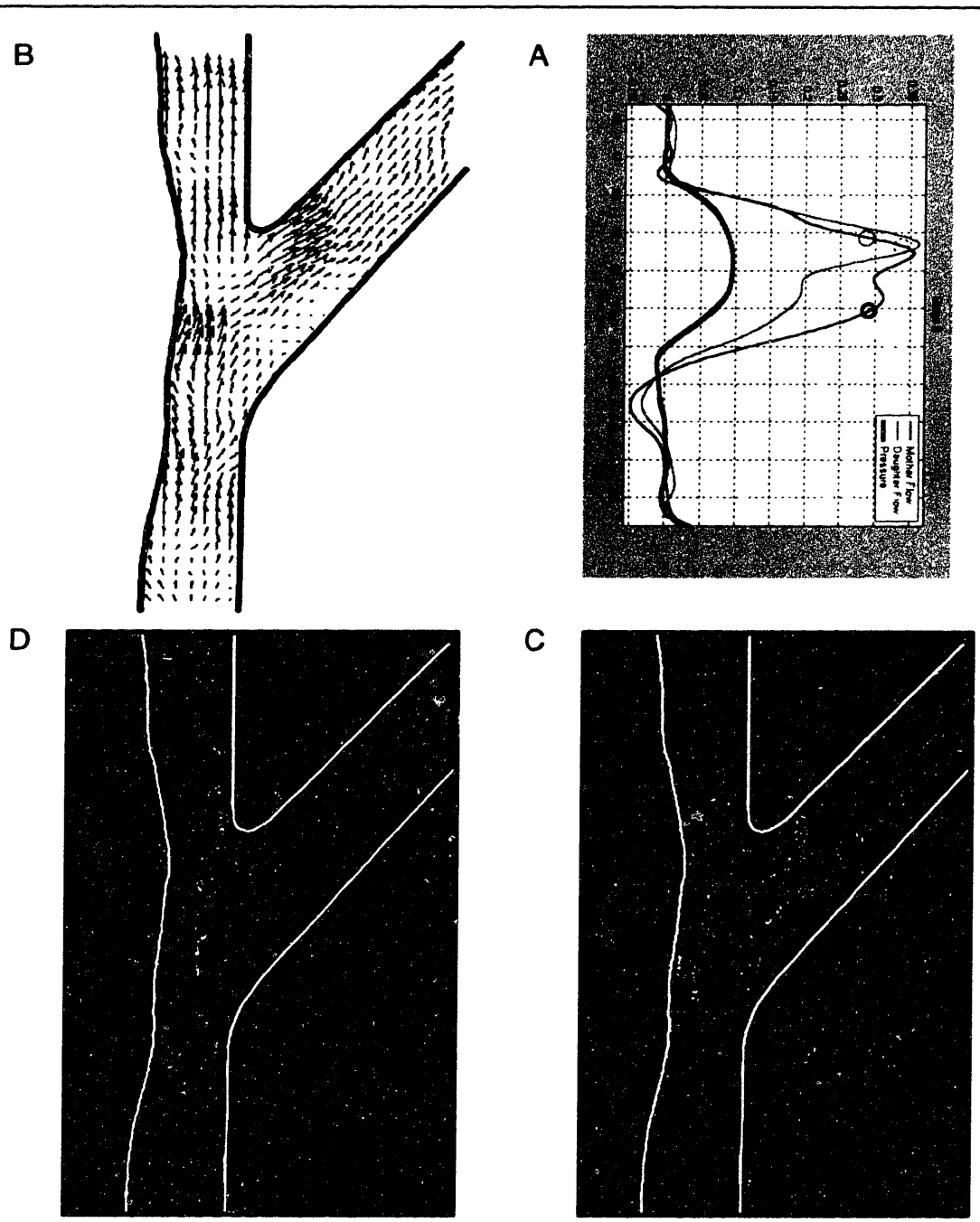

Figure 3-16: Case 13 Visualization. Main Branch: long lesion, Side Branch flow: 90%, Collateral flow: 0. (A) Waveform: Dashed circle: PIV, Single circle: Streamlines at acceleration, Double circle: Streamlines at deceleration. (B) PIV. (C) Streamlines at acceleration. (D) Streamlines at deceleration.

Cases 12 and 13 are two points along a spectrum that is somewhat different from the preceding cases in that instead of simulation of lesions in the side branch, the lesions were now located in the main branch. The location of these lesions corresponds to the region of boundary layer separation observed in the previous cases, and is thus an expression of the implicit assumption that boundary layer separation is a trigger for atherosclerosis. The minimal luminal diameter was the same in both cases; however the lesion in case 13 was approximately twice as long as that of case 12, and began proximal to the ostium of the side branch (see figs. 3-15, 3-16). Waveform analysis for case 12 (fig. 3-15A) shows the same general properties observed in previous cases. It should be noted that downstream resistance on the side branch was adjusted to produce the observed flow ratio, hence this ratio does not express the re-distribution of flow expected to arise from a lesion in the main branch alone. There is no apparent flow reversal in either the main branch or the side branch, nor is there a component of negative pressure at the end of deceleration. PIV (fig. 3-15B) as well as streamline analysis (fig. 3-15C,D) shows that despite the obvious region of flow separation in the side branch, there is no apparent disturbance in the main branch. Note particularly the long streamlines that pass very close to the lateral wall of the main branch all along the lesion in fig. 3-15C.
In contrast, waveform analysis for case 13 (fig. 3-16A) shows distinctly different features. First, the phase difference between the main branch and side branch flow waveforms was reversed from all previous cases of the experiment, with the side branch waveform at a phase lead relative to the main branch waveform. Secondly, there is now a clear aspect of flow reversal in both waveforms, as well as a component of negative pressure, suggestive of the existence of separation now in the main branch. PIV (fig. 3-16B) as well as streamline (fig. 3-16C,D) images confirm this suggestion, with a clear region of flow separation seen in the main branch distal to the apex of the lesion. Note that the flow accelerates along the lesion and does not separate up to the apex (fig. 3-16B), and then separates in the diverging section of the vessel distal to the apex. Note also that the region of separation in the side branch has decreased in size (compare figs. 3-15B,C to figs. 3-16B,C), presumably from the diversion of more flow into the side branch as the lesion in the main branch progresses.

3.3.3.2. Temporal Development of Boundary Layer Separation

Images of PIV performed during case 6 – straight main branch, no lesion in the side branch and no collateral – are presented below. These two images show the flow vector field at two instances during the cycle.

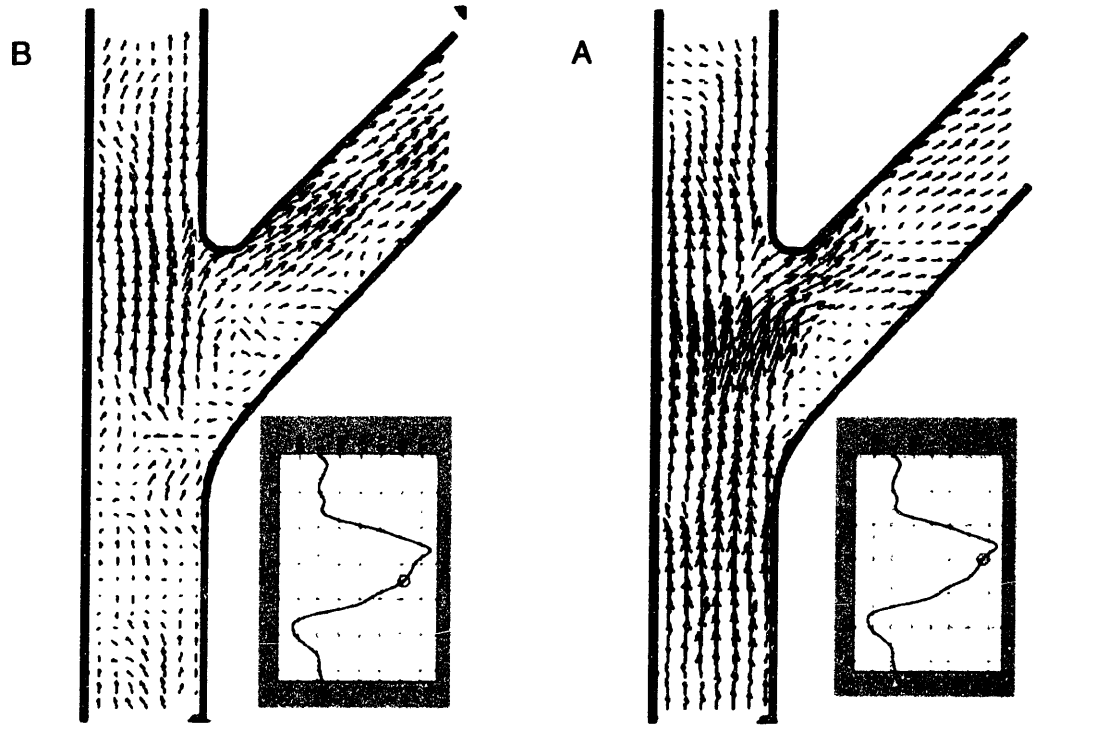

Figure 3-17: Development of Boundary Layer Separation. (A) PIV at beginning of deceleration. (B) PIV at mid deceleration. Circles denote instant of visualization

Both images in fig. 3-17 display the regions of flow disturbance in both the main branch and the side branch. Comparison between fig. 3-17A and fig. 3-17B shows how these regions change over the course of a small part of the deceleration phase of flow. The region of separation in the side branch remains in the same location, and grows rapidly outwards in the radial direction to fill almost the entire ostium of the side branch. The region of disturbance in the main branch on the other hand, grows in a more axial direction, primarily proximally and the proximal end of the disturbance rapidly moves upstream to the ostium of the daughter branch itself.

3.4. Flow Visualization – Small Side Branch Model

As discussed previously, the number of possible arterial geometries is infinite. On the other hand, the number of geometries that can be modeled (numerically and certainly physically) is finite. One possible approach is to attempt to decide on a specific case and to attempt to model that specific case as faithfully as possible. Results obtained in this way are certainly the most accurate possible description of the specific case chosen, however their application to any different case is limited by the large number of deviations from the specific conditions actually modeled. Another common approach is to attempt to average all of the instances encountered in clinical practice and then to build a model reflecting these average conditions. The difficulty with this method is in that an 'average' patient does not really exist and the interpretation of how the deviations from this average state affect the predicted results can be challenging.

We suggest here a third, different approach. First, we identify a set of parameters that describe the problem e.g. the angle of the bifurcation, the ratio of sizes of the main branch to the side branch, the total rate of flow, etc. Next, for each one of these parameters, instead of simply building the average model, we build two models reflecting the extremes of what might be encountered in clinical practice. Thus, for the angle of bifurcation, for example, we build one model with a large angle and one with a small model. The results from these extremes are compared to see which characteristics of the flow are important in one condition, which are important in the other and which are invariant with respect to the parameter chosen. In this way, we propose to build a matrix of rules of thumb that can be applied clinically in the qualitative sense to a wide array of patients.

In practice, filling out this entire matrix is a formidable task, beyond what would be practical for this work. We thus chose to demonstrate this approach using just one such parameter – the relative size of the main branch.

The experiments described in sections 3.1 & 3.2 (establishment of flow regime and mathematical modeling) were performed with the 'average' case of a main branch to side branch diameter ratio of 4:3. The experiments described in section 3.3 (flow visualization – large side branch) were performed with a 'large' side branch i.e. a 1:1 diameter ratio. To compare to the other extreme, we repeated the 'experimental scenario'

part of the flow visualization (section 3.3.3.1) with a 'small' side branch i.e. a 2:1 main branch to side branch diameter ratio.

3.4.1. Theory

It is important to realize that the flow circuit (section 2.2.1) allows control of the downstream resistance to flow for each branch independent of the diameter of the vessel. Thus, the ratio of flow rates can be dictated independent of the ratio of diameters. In practice, a smaller side branch will typically imply a lower rate of flow relative to the main branch. The degree to which this actually occurs is highly dependent on the resistance imposed by the downstream arterial beds and thus cannot be predicted based on the vessel dimensions alone. As a result, we have decided to view the flow ratios as an independent parameter separate from the diameter ratios. For the purpose of comparison to the large side branch model then, the downstream resistances were adjusted so as to produce the same flow ratios as in the large side branch model.

3.4.2. Experiment

The flow visualization experiment for the large side branch model (section 3.3.2.1) was repeated with the small side branch model as described below:

Case	Main branch geometry	Side branch flow[+]	Collateral flow[+]
14	Constant diameter	80%	None
15	Tapered*	94%	None
16	Tapered*	36%	None
17	Tapered*	18%	None
18	Tapered*	7%	23%
19	Constant diameter	90%	29%

[+] Percent of main branch flow

* 1-2 degrees

Table 3-3: Cases for scenario simulation – Small side branch.

Cases 14 through 19 in this experiment are analogous to cases 6 through 11 in the large side branch model respectively.

3.4.3. Results and Discussion

Comparison of the qualitative flow pattern for the small side branch model (fig. 3-18) to the large side branch model shows that the results as far as the main branch are concerned are very similar. In the initial non-tapering geometry (case 14), the region of boundary

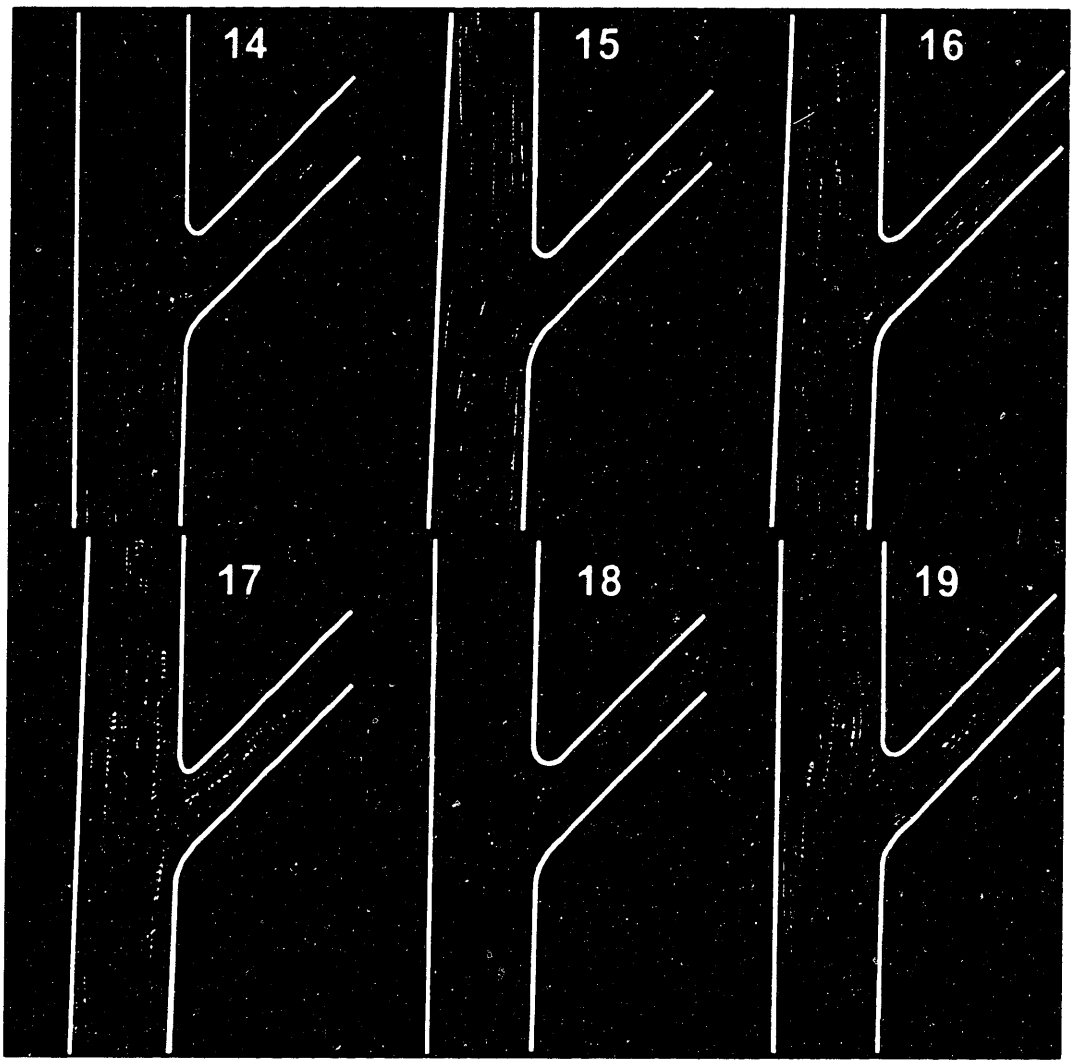

Figure 3-18: Flow Visualization in a Small Side Branch Model. Cases 14-19 track the experimental scenario described in table 3-3. Note the prominent regions of boundary layer separation in the main branch opposite form the ostium of the side branch in prior to taper and following side branch dilation (cases 14 and 19 respectively). Conversely, note the long, straight streamlines on the lateral wall of the main branch in the tapered and 'diseased' states (cases 15-17) indicating high wall shear stress.

layer separation opposite the ostium of the side branch can clearly be seen. Tapering of the main branch effectively eliminates this region of disturbance to produce smooth flow

at high shear in throughout the main branch (case 15). Following side branch occlusion, compensation and addition of collateral flow (cases 16-18) dilation of the side branch in the now non-optimal geometry re-introduces a large region of boundary layer separation in the main branch (case 19). Thus, the effect that manipulation of the side branch has on modulating main branch flow pattern seems to be dependent on side branch flow rather than diameter.

Careful comparison between the large side branch model and the small side branch model (fig. 3-19) reveals that indeed the patterns of flow in the main branch are very similar. At

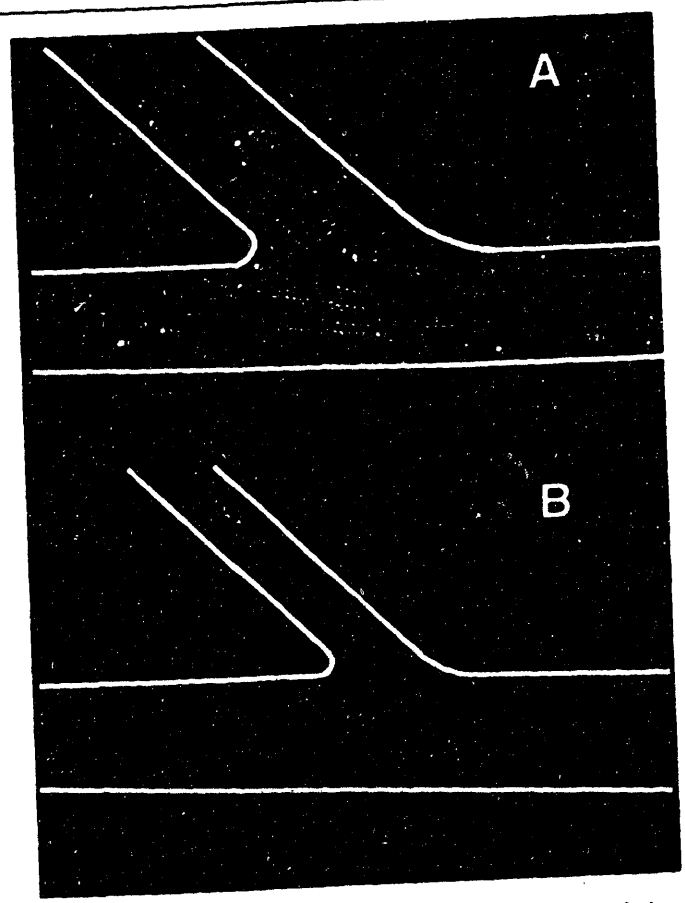

Figure 3-19: Parametric Comparison of Flow Pattern. Images of the large side branch model (A) and the small side branch model (B) taken from the same case in terms of external conditions demonstrate the qualitative difference between these two conditions. Note the similarity in region of boundary layer separation in the main branch, as opposed to the shift in localization of flow separation in the side branch. The swirling 'S' pattern is highlighted in (B).

the particular stage chosen, there is a small residual region of streamline curvature in both images, the location and extent of which is nearly identical. Conversely, the pattern of

flow in the side branch in the two cases is entirely different. Whereas the boundary layer separation in the large side branch case is associated with the lateral wall, in the small side branch case, the region of boundary layer separation is clearly associated with the flow divider. On video, particles flowing in towards the apex of the flow divider can be seen to be deflected towards the lateral wall and then rapidly down the side branch hugging the lateral wall. This swirling 'S' pattern was not seen at all in the large side branch model.

4. In-Vivo Methods

The *in-vivo* investigation of the effects investigated by the bench-top modeling required the development and utilization of novel methods in animal experimentation. These methods included a new animal model of bifurcation restenosis, a novel method for the occlusion of large arteries and a novel histopathological technique. These will be discussed below:

4.1. Animal Model

4.1.1. General

A unique animal model had to be developed to correlate the bench-top experiments to *in-vivo* findings. The first important requirement from this model was the ability to accurately manipulate arterial geometry. In practice, this meant choosing as large a model as possible to facilitate accurate manipulation of stents relative to the arterial geometry. The porcine animal model was found to be ideal for this purpose due to its size, relative ease of use and the considerable experience present in our lab in working with this animal. We chose to work with the bifurcation of the external iliac artery into the femoral and the deep femoral arteries (fig. 4-01). This particular bifurcation offers several important advantages:

1. Large diameter: The femoral artery (the main branch) has a diameter of approx. 6mm, whereas the deep femoral (the side branch) has a diameter of approx. 4mm. These sizes allow for precise placement of stents relative to the arterial geometry.
2. Reproducible: The structure and dimensions of this particular bifurcation (diameters and angles) were largely constant for all animals tested thus minimizing variability within and between groups.
3. Control: Utilizing the fact that there are two (nearly identical) such bifurcations in each animal, animals could serve as their own internal control. This was done by treating one side of the animal (in practice always the right-side bifurcation) and using the data from the other (left) side as baseline.

Figure 4-01: Animal Model Anatomy. The porcine arterial anatomy used for the purposes of *in-vivo* experimentation is shown in schematic form (left) and in an angiogram (right). Note the existence of two nearly identical bifurcations allowing for the use of an internal control.

4.1.2. Model

To examine the effect of side branch dilation on main branch stents, an experimental animal model was developed to compare between bifurcations with an occluded vs. a patent side branch. In all animals, the right-sided deep femoral artery was occluded (see section 4.2). This created two bifurcations, one with an occluded and the other with a patent side branch in the same animal (fig. 4-02).

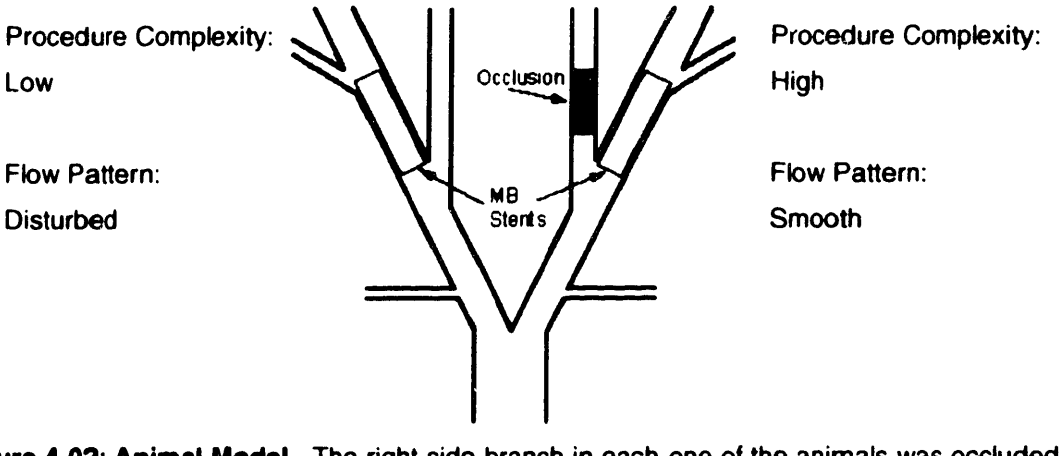

Figure 4-02: Animal Model. The right side branch in each one of the animals was occluded, while the left one was left patent. Stents were implanted in both main branches in the locations shown. This model allows for comparison between both scenarios in the same animal. Note the reversal in the contribution of procedure complexity vs. flow pattern in the expected results

Identical stents were implanted in the main branches of both bifurcations in the position shown. These stents were long enough to cover the entire segment of the main branch from the bifurcation of interest all the way up to the next bifurcation. The right-sided main branch stent functions within the context of an occluded side branch, whereas the left-sided main branch stent functions within the context of a patent side branch (simulating a side-branch that has been dilated). Thus, the clinical situation is reversed: In clinical practice, the side branch would be occluded to begin with and the choice would be between dilating it or leaving it occluded. In the model, the side branch is patent to begin with and the choice is whether to occlude it or not. It should be noted that despite this reversal, it is not our intention to model a clinical scenario of purposely occluding a side branch. Rather, the left bifurcation in fig. 4-02 represents the clinical strategy of 'dilating the side branch' whereas the right side represents the clinical strategy of 'leaving the side branch occluded'. This reversal of steps does offer one interesting benefit: it allows us to test the root cause of disparate success for angioplasty of single and bifurcation lesions. The accepted dogma is that added procedural complexity and time reduce the long-term success of bifurcations. In the bifurcation two vessels must be treated rather than one, with added time, injury and manipulation. In the current animal model, the reversal of order previously discussed induces greater complexity on the side branch subjected to occlusion. The hypothesis that predicts stent performance based on the complexity of the treatment would suggest that the occluded side branch side would do worse (fig. 4-02). In contrast, the hypothesis based on flow pattern would predict that the un-occluded side would do worse. This system thus allows one to test the relative contribution of each one of these factors.

4.1.3. Stents

In clinical practice, stents are placed in arteries with significant atherosclerotic disease. These arteries are typically stenosed, calcified, contain lipid pools and have aberrant vasomotor tone, growth control, and surface hemostasis. All of this altered physiology contributes to the rate of restenosis associated with the implantation of stents. Animals used for experimentation, on the other hand, are typically young, healthy and possess clean arteries. Thus, if they are simply stented as one would do a human, they tend to

exhibit little to no restenosis. To study the process of restenosis in an animal model, one must elicit restenosis by abnormal manipulation of the arteries. There are numerous ways in which to do this including chemical abnormalities such as feeding the animals a high-cholesterol diet, as well as mechanical ones such as balloon denudation of the endothelial cell layer, or balloon over-inflation of the arterial wall. It is important to keep in mind that none of these methods claims or even attempts to identically re-create the human condition. Rather, these are simply models that allow one to study other factors that may or may not modulate the restenotic process.

The porcine model does not lend itself well to hypercholesterolemia as pigs become so large that they are unmanageable. Initially, we made attempts at both balloon denudation and over-inflation injury. However, even these procedures induced little to no neo-intimal hyperplasia after implantation with a regular stainless steel stent (fig. 4-03). One possible explanation for this failure involves the large size and elasticity of these peripheral arteries. These properties make them especially resistant to attempted mechanical injury of the sort induced by over-expansion.

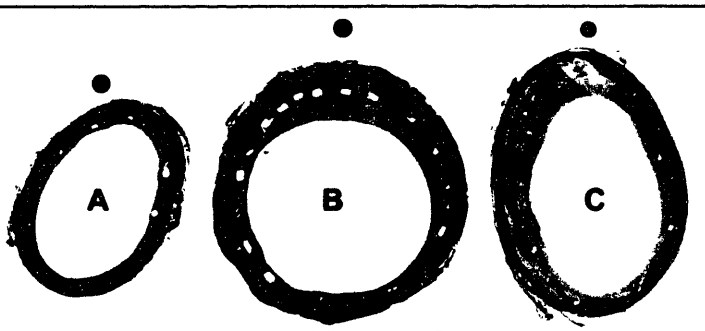

Figure 4-03: Neo-Intimal Response of Different Stent Types. Microscope images of porcine Iliac arteries stented with different stent types stained with Verhoeff's elastin stain. A normal modern stent (A) produces little to no restenosis at 14 days. A first generation (Palmaz P-108) stent (B) in the same animal produces substantial neo-intimal proliferation. Note the higher number of stent struts and their substantial thickness. A modern stent whose surface was contaminated with copper (C) produces a similar effect at 28 days. Note the eccentricity of the lesions in the two latter examples. The blue dot next to each section denotes the lateral wall of the bifurcation.

To overcome this difficulty we used stents with properties that would induce excessive neo-intimal hyperplasia upon implantation including early versions of clinical stainless steel stents and copper-doped experimental prototypes. The Johnson & Johnson P-108 stent is a first generation stent that possesses sub-optimal mechanical properties. Its struts are large in cross-section, producing excessive local injury upon deployment as well as local flow-disturbance once in place. The stent surface properties are sub-optimal as well. Outdated cutting, cleaning and passivating techniques leave uneven and abrasive surfaces. Stents were implanted in the absence of prior balloon injury as balloon inflation had no added effect on lesion formation but could induce vascular complications and consume significant time. Substantial neo-intimal hyperplasia was observed at chronic follow-up (fig. 4-03). Moreover, the circumferential distribution of the restenotic layer was clearly skewed in a manner fitting the bench-top experimental prediction, as will be discussed extensively later. However, the limited availability of these stents, as well as their short lengths forced use of alternative devices.

Copper is well-known as a highly thrombogenic as well as atherogenic material. Small arteries are often intentionally occluded clinically using a percutaneously-implantable copper coil. We thus reasoned that a stent whose surface was electro-plated with a small amount of copper would induce a higher degree of neo-intimal response. The NiRoyal stent is a modern stainless steel stent design available in many lengths and sizes, in which the stent surface is electroplated with gold. The gold plating is radiopaque and thus aids in precise placement of the stent relative to arterial and/or lesion geometry. Copper powder was mixed in with the gold during the electroplating process at different concentrations. Auger microscopy characterized the percentage of stent surface covered by copper by molecular weight. These stents were then implanted in porcine Iliac arteries and followed for 28 days. A surface copper concentration of 10-15% was found to produce reproducible lesions several hundred microns in thickness that were large enough to be characterized and modulated, but not too large so as to obscure the underlying asymmetric process (fig. 4-03).

4.2. Side Branch Occlusion

In-vivo simulation of the hypotheses discussed here was contingent on development of an adequate method for Side Branch (SB) occlusion. Surgical occlusion through either ligation or placement of occlusive devices was briefly considered but then discounted as being too labor-intensive as well as injurious to the general region. Thus, a need arose to develop a technique for percutaneous occlusion of large (3-5mm) arteries. Starting from very naïve approaches, the method of SB occlusion has evolved together with our understanding of the processes that take place with implantation of these devices (fig. 4-04).

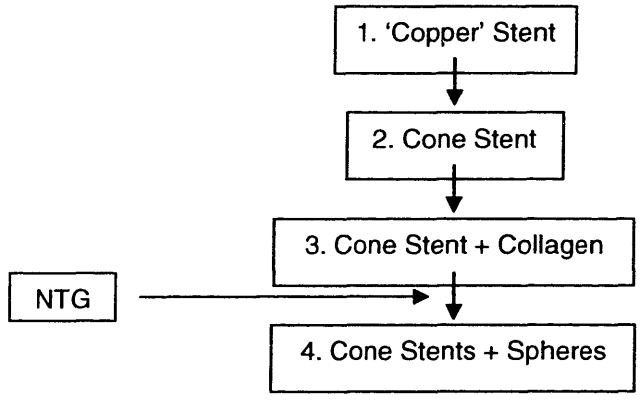

Figure 4-04: Side Branch Occlusion Schemes. Four different SB occlusion schemes were attempted with varying results.

4.2.1. Occlusion Using a Copper-Contaminated Stent

Following the same reasoning given above, 16mm long NiRoyal stents were electroplated with large amounts of copper. Approximately 40% of the surface was covered by copper as measured by Auger microscopy for molecular weight (compare to the 10-15% used in section 4.1.3 to induce a thin neo-intimal layer). These stents were then implanted in the SB of several animals which were then followed for 16 days. Angiographic analysis at 16 days showed that complete (or even nearly complete) SB occlusion did not in fact occur (fig. 4-05).

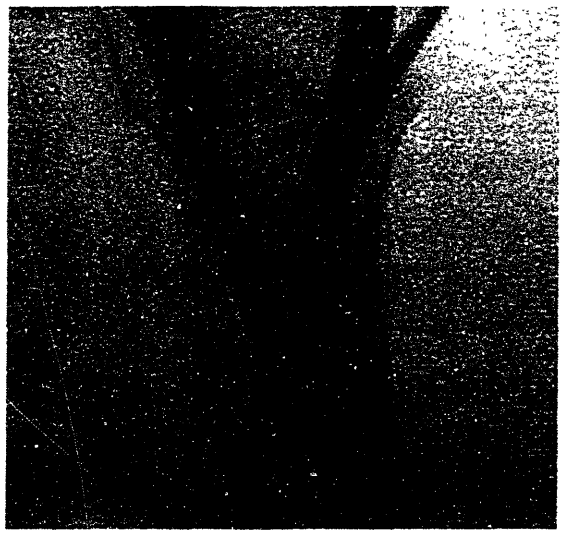

Figure 4-05: Occlusion Using Copper Stent. Angiographic image at 16 days post implantation of copper-contaminated stent in the SB of a bifurcation. Lack of occlusion of the SB is evident.

4.2.2. Occlusion Using a Cone Stent

In clinical practice, great care must be exercised when manipulating arteries to prevent accidental occlusion secondary to thrombosis. It is commonly assumed that any object that protrudes into the lumen will lead to a localized flow disturbance which will in turn lead to thrombosis and arterial occlusion. Indeed, in the early days of endoluminal stenting, acute and sub-acute thromboses were common occurrences and major hurdles to the widespread use of stenting. Accordingly, we assumed that introduction of a large physical disturbance into the lumen would lead to flow disturbance, thrombosis and ultimately occlusion of the SB. The device selected for this purpose is described in fig. 4-06.

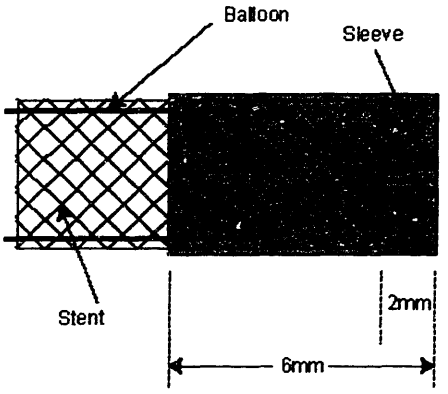

Figure 4-06: Schematic of SB occluder. The occluder device is composed of a stent crimped onto the end of a balloon, with a polyurethane sleeve mounted around the outside. When the stent is expanded, the sleeve forces the distal end of the stent into a funnel shape.

The main components of this system are:

1. NiRoyal 25mm 9cell stent. The characteristics of this particular stent that make it well suited for this purpose are:
   1.1. Length: at least 25mm is necessary for both anchoring and tapering segments (see below).
   1.2. Diameter: suitable for stenting of 4-6mm vessels.
   1.3. Radiopacity: gold coated stent aids in precise placement in vessel.
2. Cordis Charger 4.0x30mm balloon. This balloon was chosen due to its relatively short tip.
3. Polyurethane tubing.
   3.1. Diameter: 1.5mm
   3.2. Wall thickness: 140μm

The stent was crimped onto the balloon such that the distal end of the stent was 2mm back from the balloon tip (see fig. 4-06). Next, a 6mm long segment of the polyurethane tubing was cut and slipped onto the external surface of the stent so that the distal end of the tube was flush with the distal end of the balloon. The balloon was deployed at an inflation pressure of 10atm for 30 seconds. After inflation, the compression force generated by the sleeve is larger than the maximal radial force of the stent, and the distal

end of the stent collapses back to its crimped diameter. Thus, the stent is anchored in place by its proximal segment; whereas the distal segment creates a funnel of crisscrossing struts in the center of the lumen (fig. 4-07).

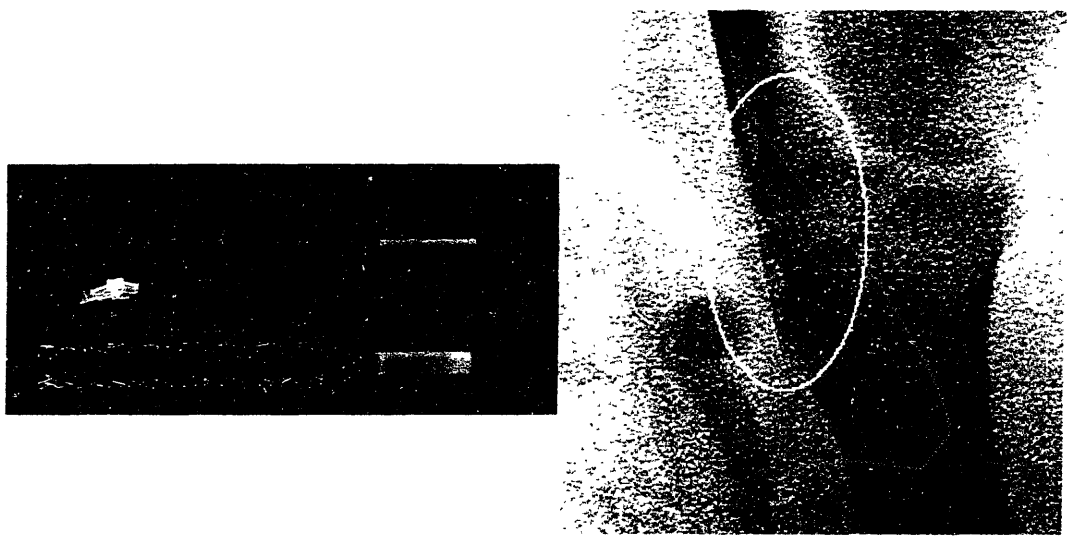

Figure 4-07: Deployed Side Branch Occluder. Side Branch Occluder *in-vivo* (right) and on the benchtop (left).

An attempt was made to measure flow rates into the SB pre and post occlusion using a Flow-Wire. This type of device measures the maximal flow rate at some point in the cross-section and then uses an assumed cross-sectional velocity profile (Hagen-Poiseuille parabolic solution) to calculate the total flow rate. This method is obviously dependant on the actual flow profile which in bifurcations can be quite far from parabolic. Thus, it was not surprising that the Flow-Wire measurement was found to be highly erratic and non-reproducible and was thus discontinued. Unfortunately, no other method was found to non-invasively obtain a reasonably accurate measurement of flow rate.

Despite the obvious creation of a severe flow disturbance, 28 day follow-up on the three animals in which this procedure was performed showed a completely patent SB by angioplasty (see fig. 4-08).

Animal #9368 Animal #9371 Animal #9372

Figure 4-08: Occlusion using cone stent. 28 day angiographic results showing lack of SB occlusion using cone stent.

Histological analysis showed that in spite of the angiographically pristine appearance of these arteries, there was in fact neo-intimal hyperplasia induced by the placement of cone-stent device. Fig. 4-09 shows the longitudinal pattern of neointimal hyperplasia in a representative animal.

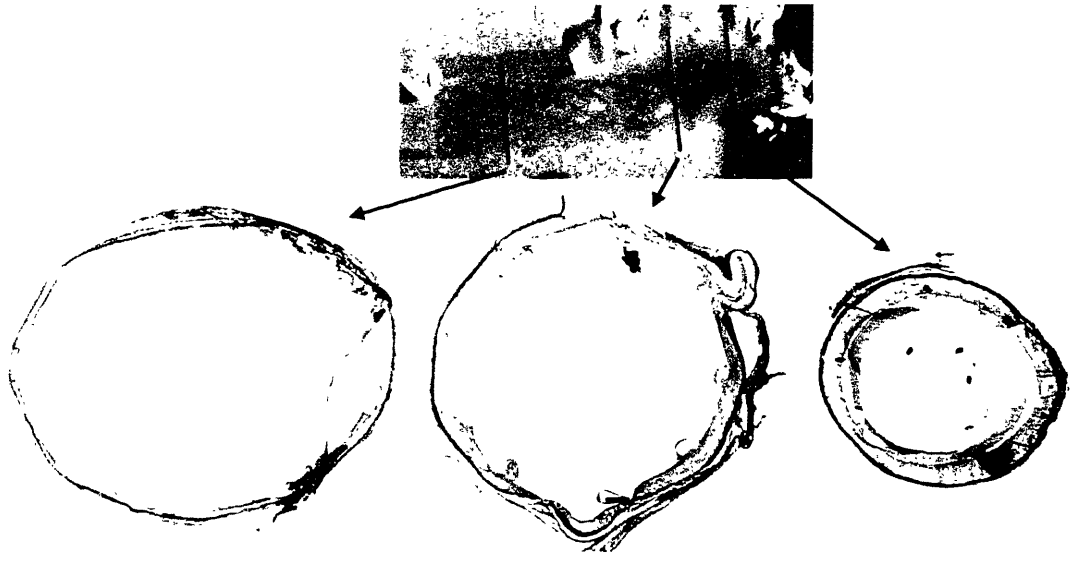

Figure 4-09: Side Branch Occluder Sections. Serial sections along the SB occluder (shown *ex-vivo* above) from proximal (left) to distal (right) end show absence of neo-intimal hyperplasia in the proximal and mid sections and a concentric ring of neo-intimal hyperplasia beyond the funnel section. Stain: Verhoeff's Elastin.

The proximal and middle sections exhibit little to no neo-intima as would be expected for a modern stent deployed in a large, healthy artery. The distal section, beyond the funnel segment, shows a unique pattern (see also 4-10): The central region within the collapsed stent struts has completely occluded with a thrombotic plug. The arterial wall shows a uniformly thick layer of neo-intimal hyperplasia. This neo-intimal layer is particularly interesting in light of the fact that no mechanical injury was imparted to arterial wall at this point. Indeed, neither the stent nor the balloon came in contact with the arterial wall beyond the funnel segment. Thus, this concentric ring of neo-intimal hyperplasia was induced purely by the alteration of flow pattern, first and foremost the creation of a new boundary layer in the center of the lumen.

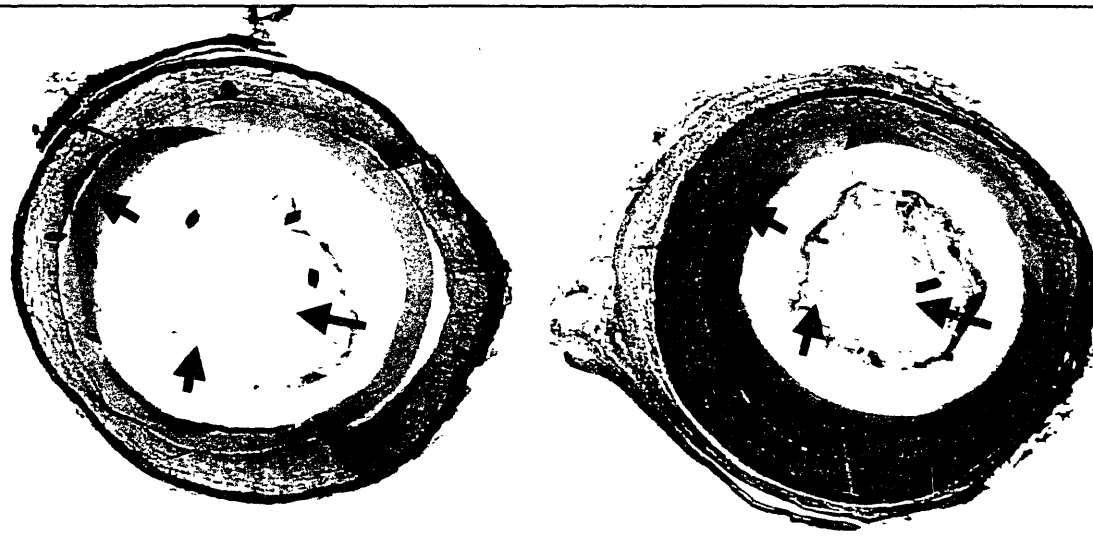

Animal #9371 Animal #9372

Figure 4-10: Cone Stent Occluder Distal Histology. Distal sections from two animals downstream from the cone segment. The collapsed stent struts (red arrow) can be seen in the center, filled with a thrombotic plug (green arrow). A concentric layer of neo-intimal hyperplasia encircles the entire artery (blue arrow). Blood flow occurs in the annular space in between (yellow arrow).

Blood flow through these arteries occurs in the concentric annular space between the thrombotic plug in the center and the hyperplastic wall on the outside (see fig. 4-10). Since angiography displays a two-dimensional projection of this lumen, the vessel appears by angiography to be completely patent. In reality, one must assume that the resistance of this vessel is greatly increased and thus that the total flow through it is

decreased. However, absent any way to quantify this new flow rate, and given the need for a total occlusion, this method was deemed inadequate.

4.2.3. Occlusion Using Cone-Stent + Collagen

Given the failure in trying to induce the vessel to thrombose on its own, it was decided to attempt to induce thrombosis. The approach was to find a highly thrombogenic material and to position this material within the SB. VasoSeal is a device used for closure of punctures created for arterial access during angioplasty. It is composed of a synthetic mesh of collagen, which is one of the most thrombogenic materials known. Occlusion was performed in a two-step process:

a. A cone-stent (see 2 above) was deployed in the SB.
b. VasoSeal material was slightly loosened in saline and then, under fluoroscopic guidance, injected through the guiding catheter directly into the proximal portion of the SB. The strands of collagen were carried downstream and caught within the funnel segment of the cone-stent.

This process leads to complete occlusion of the vessel within seconds (fig. 4-11).

Figure 4-11: Occlusion Using Cone-Stent + Collagen. Panel A shows bifurcation prior to intervention. Panel B shows acute result immediately after injection of collagen into cone-stent. Panel C shows distal migration of occluder at 3 days post occlusion.

Early attempts at using this occlusion strategy showed that the entire occluder had a tendency to migrate distally over time (see fig. 4-11). In several cases, this new location was distal enough to the SB ostium that it enabled flow through the first branch of the SB itself thus negating the occlusion. It was felt that mild vasoconstriction at the time of the intervention led to an undersizing of the cone-stent relative to the actual arterial

dimensions. After the procedure, when vasorelaxation occurred, the stent would not be well-opposed to the arterial wall. This, in combination with the excess force created by the flowing blood pushing against the plug would be enough to dislodge the stent and carry it distally. To overcome this problem, nitroglycerin (200μg) was administered intra-arterially prior to cone-stent deployment to ensure maximal vasodilation.

Despite the early success in obtaining SB occlusion by this method, occlusion was not sustained in the long term (fig. 4-12). It is likely that sometime between 72 hours (at which all side branches were occluded) and 28 days (at which almost all side branches were patent), collagenases and other enzymes had a chance to break down the collagen and thrombus plug and to re-cannulate the artery.

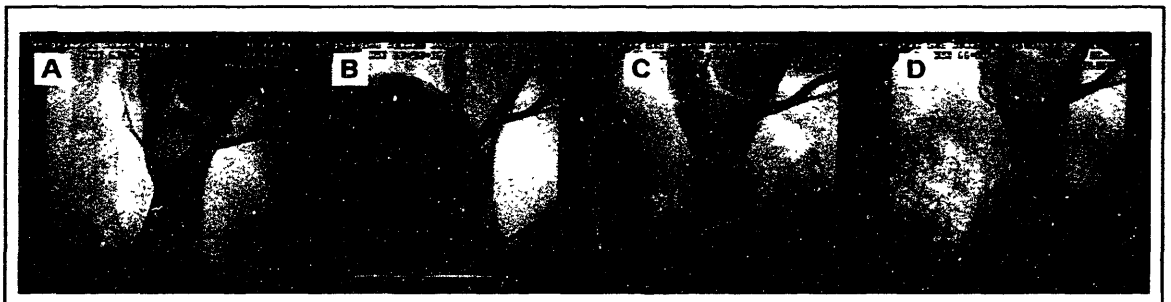

Figure 4-12: Re-Cannulation Following Cone-Stent + Collagen. Panel A shows bifurcation prior to intervention. Panel B shows acute result immediately after injection of collagen into cone-stent. Panel C shows good occlusion at 3 days post occlusion. Panel D shows re-cannulation of the SB at 31 days post occlusion. Note that the cone-stent has not migrated and yet the SB is nearly completely patent.

Figure 4-13 shows a representative histological analysis of such an occluder at 31 days post implantation. The occlusion has in fact re-vascularized forming several large channels of flow.

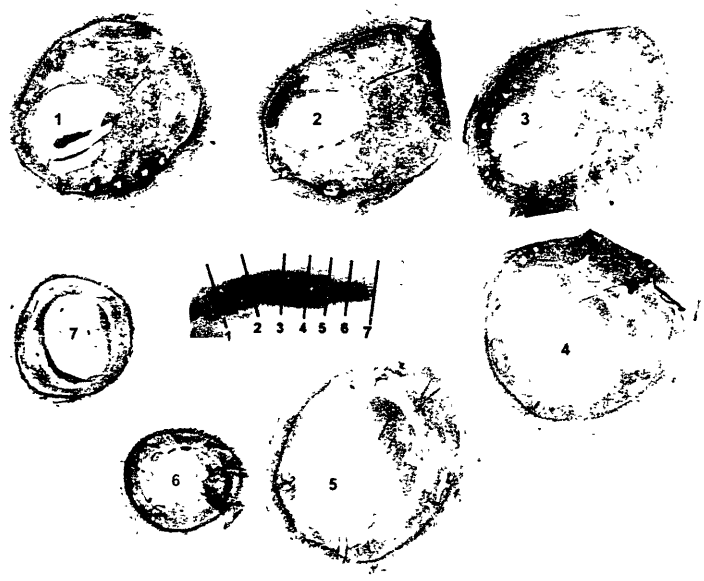

Figure 4-13: Histology of Re-Cannulation. Serial histological sections of cone-stent with collagen stained with Verhoeff's elastin stain. Figure shows progression from proximal to distal end (clockwise from top-left) with the location along the actual occluder shown in the center. Note the several large channels of flow through each one of the sections at 31 days post total occlusion.

4.2.4. Occlusion Using Cone-Stents + Microspheres

The promising acute results obtained with the cone-stent + collagen method (see above), coupled with the poor chronic result due to lysis/metabolism of the occluding material prompted a search for another injectable occluding material. The optimal material should be:

a. small enough to make it easy to inject through a guiding catheter
b. large enough to become entrapped within the cone-stent
c. thrombogenic enough to induce a total occlusion over a relatively brief period of time
d. able to 'bleed off' pressure until the stent became well-embedded within the vessel wall. This would prevent the stent from migrating downstream
e. composed of a material that cannot be lysed or in any other way metabolized over the course of the experiment

The polymer microspheres used for flow visualization in the flow models (see 2.3.1) meet these criteria quite well. Thus, the SB occlusion procedure was altered to:

1. Vasodilatation using nitroglycerin.
2. A first cone-stent was implanted with its proximal end 5-6 cm distal to the SB ostium.
3. The proximal end of the cone-stent was post-dilated at high pressure to ensure vessel-wall apposition.
4. The guiding catheter was advanced into the proximal end of the cone-stent.
5. A syringe was filled with 200-300 microspheres was connected to the guiding catheter and then used under fluoroscopy to inject the cone-stent full of microspheres.
6. A second cone-stent was implanted proximal to the microspheres to prevent leakage of spheres out of the occlusion under pulsatile flow.

Figure 4-14 shows this entire process including successful follow-up at 56 days post occlusion. This method was found to be efficient and relatively easy to employ. Three days post implantation, the SB occlusion was complete, and total occlusion was maintained at both 28 day and 56 day follow-up.

Figure 4-15 shows histological sections taken through the proximal end of the distal cone-stent (the one that contains the microspheres). These images clearly show a total occlusion formed by the volume of the packed spheres, with the spaces in between filled up by a thrombus/neointimal formation.

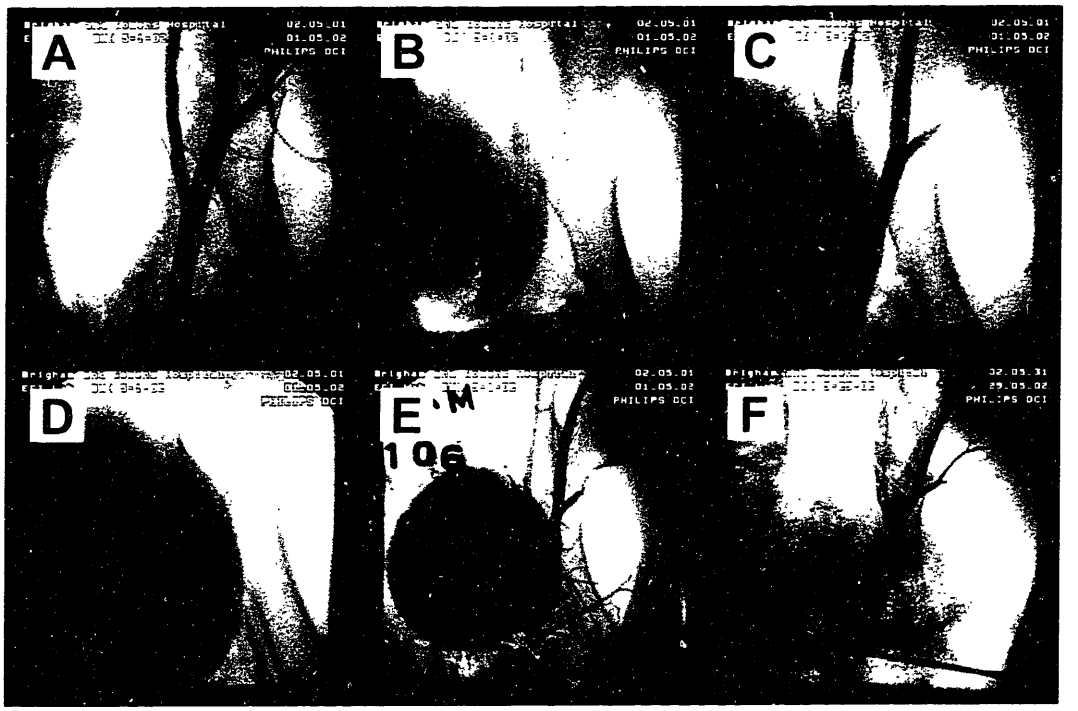

Figure 4-14: Total Occlusion Using Microspheres. (A) Bifurcation prior to intervention. (B) Post deployment of first cone-stent. (C) Post injection of microspheres. Note the radiolucent region within the stent indicating the presence of spheres. (D) Post deployment of second cone-stent. The microspheres are now trapped between the two cones (E) Acute result. Note the 'bleed off' of pressure distal to the occluded segment. This will gradually occlude completely over the course of the next few days. (F) Follow-up at 56 days post occlusion. Note the total occlusion as indicated by disappearance of the SB.

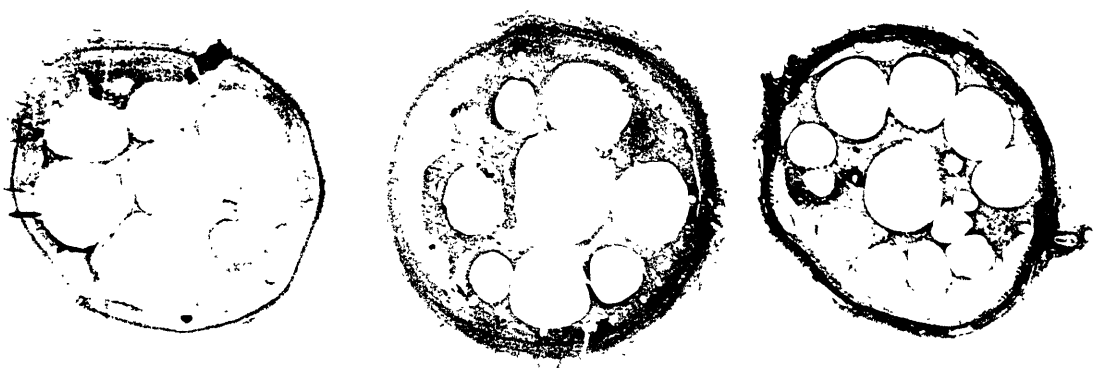

Figure 4-15: Total Occlusion Histology. Representative histological sections from 3 animals whose SBs were occluded using the cone-stent + microspheres technique. The microspheres themselves are dissolved during histological processing and hence show up as circular 'ghosts' surrounded by neo-intimal growth.

4.3. Histological Analysis

Histological processing and analysis for this project was somewhat more complex than the already challenging task of histological analyses of stented vessels. The two major specific challenges were: (1) The need to embed entire bifurcations which are substantially larger specimens than ordinary stented vessels. (2) The need for accurate spatial reconstruction of the lesion morphology. These two requirements had several immediate practical ramifications including:

a. Processing of very large samples requires special techniques to ensure proper perfusion and exposure of samples to various solvents while minimizing carry-over.

b. Embedding of very large samples requires large volumes of polymer material which means special polymerization techniques are needed to ensure uniform results.

c. Normally, histological sections are localized with low resolution along the length of the stent. Typically, three to five sections will be examined along the length of a stented artery. These sections can be localized axially (proximal, middle, distal) but cannot be oriented angularly. Thus, for each slide, there is no way of knowing what part of the circumference is derived from which arterial wall. To match lesion morphologies to flow patterns, three dimensional reconstructions of lesion morphologies were required. These three dimensional reconstructions dictated the development and use of special techniques in embedding, sectioning, microtomy, staining and analysis to ensure proper orientation and localization of the ultimate images.

4.3.1. Tissue Harvest and Processing

After sacrifice, the two bilateral iliac bifurcations were dissected cautiously taking care not to deform or damage the stents. As soon as the proximal iliac arteries were exposed, a stainless steel barb-type tube fitting with a Luer connector was placed *in-situ* in each artery. An infusion kit was connected to each Luer connector and the bifurcation was pressure-perfused with saline during the rest of the dissection procedure to prevent

clotting. The entire bifurcations were then dissected free, pressure perfused with 10% non-buffered formalin (NBF) and then stored in NBF for shipment.

Successive processing steps, in particular dehydration, have a tendency to warp the shape of the bifurcations. To prevent this from occurring, prior to processing, the bifurcations were laid flat onto and then tied down to a tissue processing cassette using copper wire (fig. 4-16).

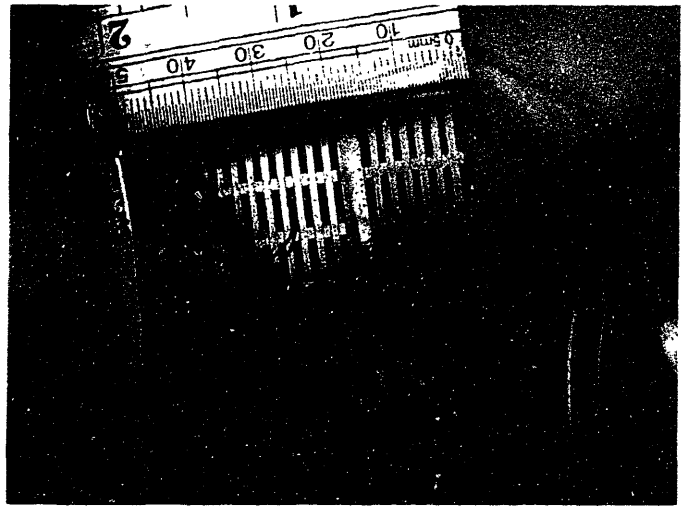

Figure 4-16: Tissue Sample Prior to Processing. Bifurcations were tied down to a tissue cassette using either suture or copper wire to prevent warping. Note the Luer connection on the proximal end used for perfusion of solvents during previous and subsequent stages.

Tissue processing included the same steps as for standard Methyl-Methacrylate embedding in our lab with two exceptions:

a. Processing times were greatly extended to account for greater tissue volumes.
b. At key times, the tissues were taken out of the processor and pressure perfused using the same solvent in which the tissues were currently residing. This was done to ensure adequate treatment of the insides of the arteries as well as to prevent solvent carry-over from one step to another.

The entire processing schedule is given in table 4-1 below.

Step	Solvent	Period (hrs)
1	10% NBF	48
2	70% Ethanol	8-96
3	80% Ethanol	2
4	95% Ethanol	2
5	95% Ethanol	2
6	100% Ethanol	4
7	100% Ethanol	4
8	100% Ethanol	8[1]
9	Xylenes	2
10	Xylenes	3
11	PolySciences Infiltration	24[2]
12	PolySciences Infiltration	24[2]
13	PolySciences Infiltration	24[2]

[1] Pressure perfusion in the middle of this step
[2] Pressure perfusion prior to this step

Table 4-1: Tissue processing schedule. Extended solvent times were needed to compensate for the large tissue volumes. The last three infiltration steps were performed in the same solution as the embedding (see below), under refrigeration (4°C) and gentle agitation.

4.3.2. Embedding

Early attempts at using the methyl-methacrylate embedding formulation normally used in our laboratory, and slight modifications thereof, were unsuccessful. The particularly large volumes required for embedding of the large bifurcation specimens led to incomplete and/or inhomogeneous polymerization. In place of the standard formulation, these large specimens were infiltrated and embedded using the Polysciences Inc. Methyl Methacrylate & Butyl Methacrylate kit which contains:

Infiltration/Embedding Solution: 80.0% (v/v) Methyl Methacrylate
20.0% (v/v) Butyl Methacrylate
0.5% (w/v) Benzoin Methyl Ether

This is a U.V. accelerated solution. Overnight exposure to U.V. light was adequate to uniformly polymerize large volumes sufficient for embedding of the entire bifurcation.

A dedicated embedding procedure was developed as part of the three dimensional reconstruction technique (fig. 4-17):

1. Pre-Polymerization:
   1.1. A 9cm diameter plastic cup was chosen such that the cup was just large enough to contain the entire bifurcation when laid flat.
   1.2. A steel wire was used to create a metal spike that stuck 2-3cm perpendicularly up from the bottom of the cup.
   1.3. A 1cm deep layer of embedding solution was poured into the cup and allowed to polymerize overnight under U.V. light, trapping the metal spike in this bottom layer in the process.
2. Embedding:
   2.1. A 1-2cm deep layer of embedding solution was poured on top of the pre-polymerized layer.
   2.2. The bifurcation was taken out of the infiltration solution and pressure perfused several times with the embedding solution to prevent solvent carry-over.
   2.3. The bifurcation was placed into the fresh solution layer in the cup and skewered onto the metal spike embedded within the pre-polymerized layer. This effectively immobilizes the bifurcation within the cup.
   2.4. The cup including the bifurcation was placed in a vacuum desicator until all air bubbles were evacuated from within the bifurcation lumen.
   2.5. A 10cm long 0.8mm diameter copper rod was placed flat on top of the pre-polymerized layer such that the rod was parallel to the lateral wall of the main branch of the bifurcation with approx. 3mm of distance between them. This rod would serve to angularly orient the final slides as described subsequently.
   2.6. The cup containing the bifurcation and rod was carefully placed under a U.V. source overnight to polymerize.

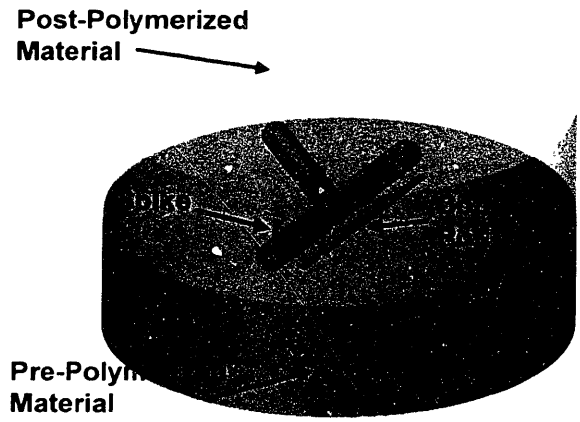

Figure 4-17: Specimen Embedding. Initially, the pre-polymerized layer is polymerized within the cup (not shown) such that it entraps the metal spike. After pouring the top post-polymerized layer, the bifurcation is placed inside, immobilized by the metal spike. The copper rod is laid flat onto the surface of the pre-polymerized layer positioned as shown.

4.3.3. Sectioning and Slide Preparation

The main goal of the procedure described below is to produce histopathological sections that can accurately localize an artery in three-dimensional space so as to produce a precise reconstruction of lesion morphology. This was achieved in the following steps:

1. The block containing the bifurcation (see embedding above) was cut out of the cup together with the embedded copper rod.
2. All faces of the block were sanded flat and then ground and polished until the block becomes transparent (fig. 4-18).
3. The required sections (usually seven equally-spaced cuts along the length of the stent) were marked onto the face of the block.
4. The block and markings were photographed to document location of the cuts.
5. A diamond wafering rotating saw was used to cut the block at the markings. Each section contained a longitudinal segment of artery together with a segment of the copper rod.
6. All sections were identically oriented using one of their edges and then photographed individually to show the relative location of the arterial segment and the copper rod.

7. Sections were microtomed (including both the artery and the rod[xiv]) and mounted on to microscopy slides using standard techniques[xv].
8. After overnight drying of the slides, a diamond-tipped stylus was used to carefully score a hole on the slide surface, within the hole left behind by the copper rod. This hole was then marked using solvent-insoluble ink.
9. Slides were stained using Verhoeff's elastin stain or H&E for morphometric analysis, immunohistochemical techniques or other stains where appropriate.

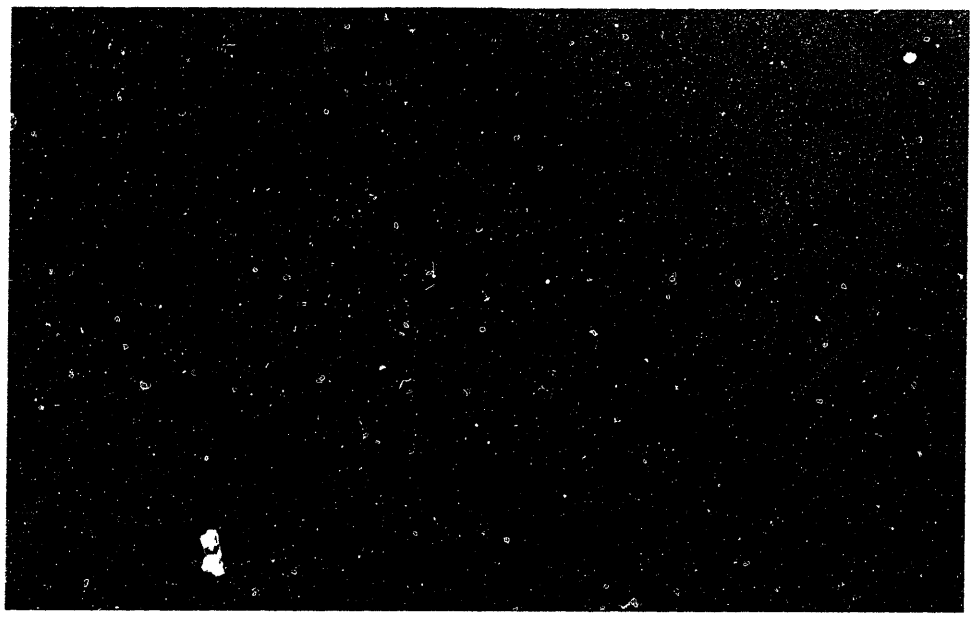

Figure 4-18: Sectioning. Figure shows arterial specimen embedded in polymer prior to cutting. Each black marking denotes the proximal end of one section to be cut and microtomed.

[xiv] The copper rod typically fell out of the 5μm thick segments, leaving behind a circular hole.

[xv] The relatively large dimensions of these microtome cuts, due to the need to contain both a large artery and the copper rod necessitated careful technique and occasionally the use of gelatin-coated slides.

4.3.4. Lesion Re-Construction

The axial location of each slide relative to the original artery was reconstructed based on the image of the markings (see fig. 4-18). The angular orientation of the slide was performed according to the following procedure:

1. The image of the most proximal section prior to microtomy (see step 6 under 'sectioning and slide preparation' above) was used to deduce the orientation of the lateral wall (opposite the SB ostium) relative to the lumen (fig. 4-19).
2. The orientation of the lateral wall relative to the lumen was then transferred to the images of all other sections.
3. For each section, the angle between the orientation of the lateral and the orientation of the copper rod was measured.
4. The angle between the location of the lateral wall and the copper rod was transferred to a digital image of the microscope slide, and then used to mark the lateral wall relative to the microscope image.

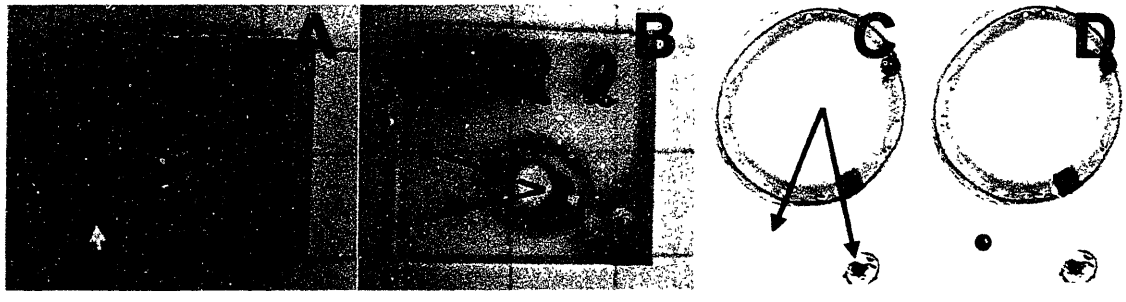

Figure 4-19: Angular Orientation. The process of angular orientation of the microscopy slides relative to the original arteries is demonstrated in four steps: (A) The most proximal section was used to determine the orientation of the lateral wall (blue arrow). Note the SB ostium 180° from the lateral wall (red arrow), and the segment of the copper rod (yellow arrow). (B) The orientation of the lateral wall was then transferred to the image of each one of the more distal segments. On each distal segment, the angle between the lateral wall and the copper rod was determined (green arrow). (C) The angle between the lateral wall and the copper rod was transferred and then aligned with the marking (black mark) on the microscope image of the section. (D) The angle between the lateral wall and the copper rod was used to mark the lateral wall on the microscope image (blue dot).

5. Finally, the separate oriented microscope images were re-assembled relative to the original image of the bifurcation to re-create the geometry of the entire lesion (fig. 4-20).

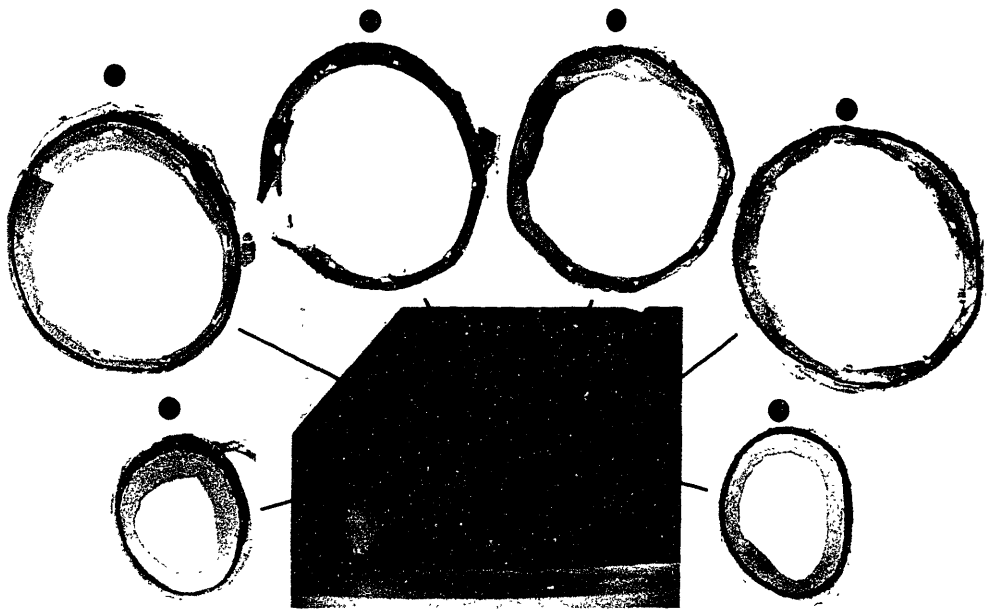

Figure 4-20: Lesion Geometry. Serial microscopic images (proximal to distal counterclockwise from bottom right) are shown relative to the image of the original bifurcation. All images were oriented angularly as previously described. The blue dot on each section denotes the lateral wall of the main branch.

5. Chronic In-Vivo Experiments

While the bench top experiments presented previously are unique in their focus on a dynamic-adaptive rather than a fixed geometry, the modeling of flow patterns inside of large arteries is not new. The association between regions of flow disturbance, specifically boundary layer separation, and sites of atherosclerotic lesions has been the topic of extensive study for several decades. These studies, however, have primarily been retrospective analyses aimed at providing an explanation for the occurrence of atherogenesis at specific locations and not at others.

A-priori prediction of the pattern of intimal hyperplasia in a certain class of geometries, such as bifurcations, has not been attempted because of several important limitations:

1. The role of flow in determining lesion geometry: It is generally agreed that flow patterns play a central role in determining the localization of atherogenesis i.e. why a lesion forms in one place versus another. However, the actual geometry of the chronic lesion is undoubtedly affected by many other parameters. It is thus not clear whether one could make meaningful predictions regarding the geometry of chronic lesions based solely on flow pattern.

2. Primary vs. secondary flow phenomena: The flow pattern in even the simplest realistic arterial geometry is highly complex. While the primary pattern can usually be demonstrated globally, as one proceeds to considering secondary, tertiary and higher order flow phenomena the level of complexity increases. In contrast to the pattern of flow, atherosclerotic geometric patterns are simple. It is thus unclear whether one can predict the geometric lesion pattern based on the primary flow pattern alone. Recently methods have been developed to create a high resolution (computational) flow models for a specific vessels' geometries. Unfortunately, the precise accurate re-creation of an individual vessel is a complex task suitable for research purposes but not applicable to a clinical setting. To be directly translatable to common clinical practice, the model needs to be as generalized as possible thus making its features applicable to a wide set of clinical conditions. At the same time, this means that the model and the *in-vivo* prototype will share only the most global geometry and hence only the most global flow pattern.

The question then becomes – Is the global flow pattern enough to predict lesion localization and geometry, or are detailed local patterns necessary?

3. Atherogenesis vs. restenosis: The association and relationship between flow patterns and vascular lesions has typically been demonstrated for atherogenesis as opposed to restenosis. While similar in many respects, restenosis and atherogenesis are not the same process. Some of the major factors that exist in restenosis but are entirely absent from atherogenesis are direct mechanical injury to the endothelial layer, and the permanent presence of a foreign body. Thus, it is unclear what the relative importance of flow pattern would be in restenosis.

The goals of the chronic *in-vivo* experiments were to begin to answer the questions raised above, to provide validation for the bench-top models and to examine the predictions based on the models related to effects of side branch flow.

5.1. Geometric Pattern of Restenosis at a Bifurcation

The goal of this segment was to provide qualitative evidence for correlation between the model predictions and the chronic *in-vivo* pattern of restenosis. Through this, we hoped to both validate the utility of the models and to examine the hypothesis that flow patterns play a central role in the localization and geometry of restenotic lesions. For this purpose, the main branch of pig iliac-femoral bifurcations was stented as previously described. The animals were then euthanized 14 or 28 days post stenting and the arteries excised, processed and analyzed as previously described to show both the morphology of the lesion and its composition.

5.1.1. Morphology

The geometric pattern of chronic restenotic lesions in the main branch of the bifurcation

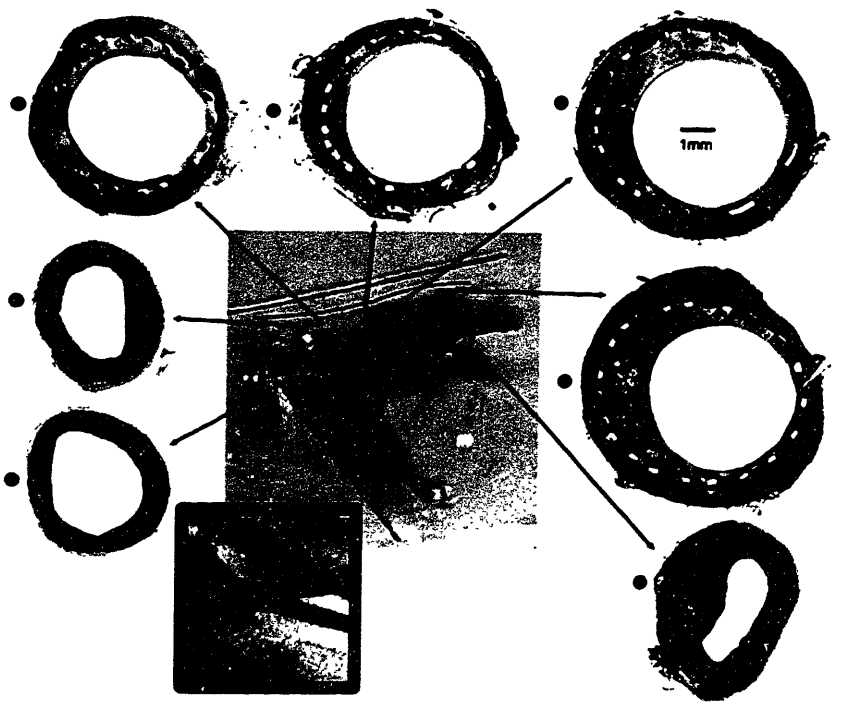

Figure 5-01: Lesion Geometry I. Chronic (14 day) lesion in a stented main branch of an arterial bifurcation. Each arterial section is shown with an arrow corresponding to the location relative to the original excised bifurcation (center image). Blue dots denote the lateral wall of the main branch demarcated as a solid blue line in the intact specimen. The copper rods that run along the main and side branches are visible as well and used as above for orientation. Inset: angiographic image of the original bifurcation in-vivo. Note that the highly eccentric lesion is centered around the lateral wall of the bifurcation. Stain: Verhoeff's Elastin. Stent: Palmaz P-108.

(figs. 5-01 & 5-02) bears a striking correlation to the prediction based on the bench-

top modeling. The restenotic lesion is highly eccentric with a maximum thickness located at the lateral wall of the main branch of the bifurcation. Use of a long stent in this

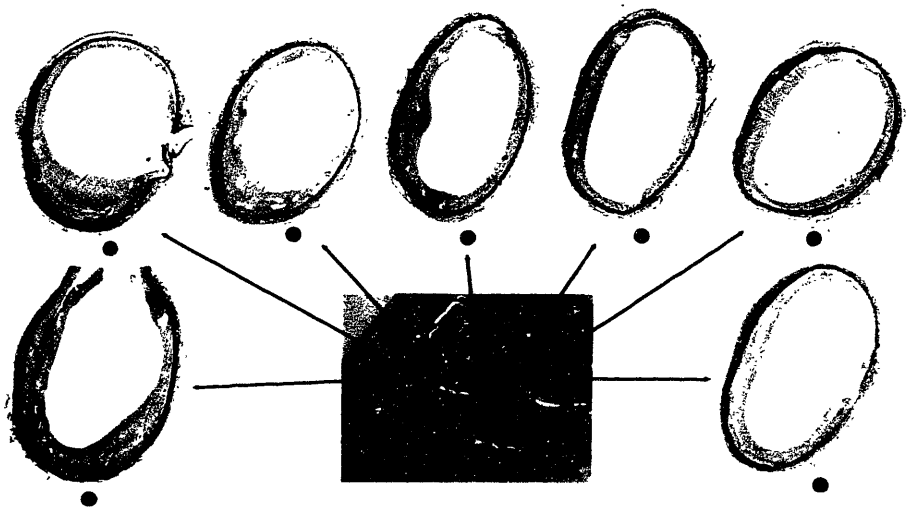

Figure 5-02: Lesion Geometry II. Chronic (28 day) lesion in a stented main branch of an arterial bifurcation. Each arterial section is shown with an arrow corresponding to the location relative to the original excised bifurcation (center). Blue dots denote the lateral wall of the main branch. Note that the highly eccentric lesion is centered around the lateral wall of the bifurcation. Axially, the lesion begins immediately opposite the ostium of the side branch grows rapidly and then shrinks back as one moves distally along the stent. Stain: Verhoeff's Elastin. Stent: NIRflex Royal w/ copper contamination.

model achieves two important purposes: it allows one to look at the longitudinal pattern along the entire segment between two bifurcations, and it reduces the effect of the stent ends on the pattern of restenosis. When this is done (fig. 5-02) it becomes evident that the pattern of restenosis matches that of the region of boundary layer separation demonstrated in the models in both its circumferential localization and its axial pattern. Circumferentially, the lesion is located on the lateral wall of the bifurcation. Axially, the extent of the lesion grows rapidly from opposite the ostium of the side branch at the proximal end, and then deceases in size along the length of the stent.

The general qualitative pattern of restenosis is maintained for nearly every single animal examined. The precise quantitative pattern is more variable in nature. This variability is likely due to at least two causes:

a. Variability in the vascular geometry and hence pattern of flow between different animals.
b. Variability in the extent of biologic tissue response to injury between animals.

A quantitative description of the geometric pattern of restenosis requires first that the data from each animal be normalized to account for the basal level of neo-intimal response to stenting/injury. The question becomes – what is the best reflection of this 'basal level'? The lateral wall reflects primarily the effect that the flow disturbance has on the rate of restenosis as opposed to the inherent biology. Similarly, the sections at the proximal and distal ends of the stent include a variability that is affected to some extent by the variable position of the stent relative to the bifurcation. Minor changes in position can lead to significant variability in mechanical injury at the ends of the stent during deployment in

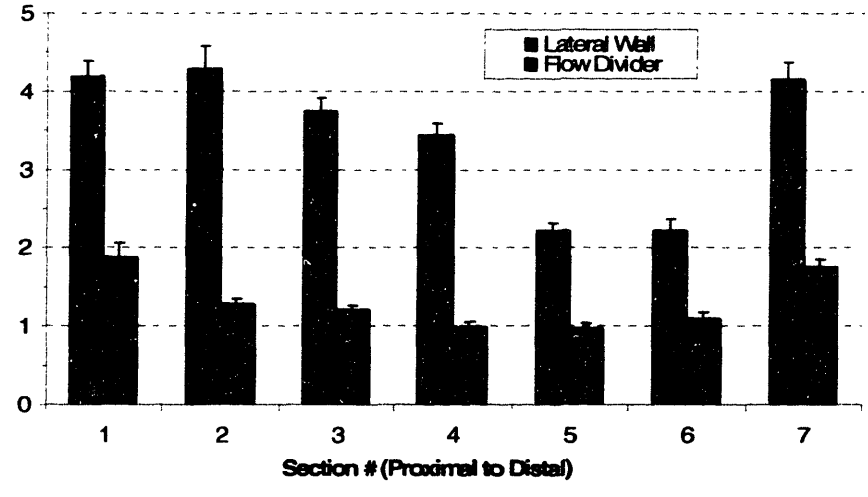

Figure 5-03: Quantitative Analysis of Lesion Geometry. Average (n = 11 animals) normalized thicknesses of the chronic (28 day) neo-intimal layer. Values are given for the lateral wall and the flow divider. Stent: NIRflex w/ copper contamination. Error bars here and everywhere else in this manuscript represent standard error.

this sensitive location. Thus, quantification was performed by measuring the thickness of the neo-intimal layer at the lateral and the flow divider wall. All measurements for each

animal were then normalized by the average thickness of the neo-intimal layer on the flow divider wall of sections 3,4&5. The average pattern of restenosis (fig. 5-03) recapitulates the pattern seen in each individual animal. The lesions in the main branch are highly eccentric with neo-intimal thickness at the lateral wall reaching values of up to 3.5 times higher than those on the flow divider wall. The difference between the two walls grows rapidly to a maximum just distal to the proximal end of the stent (section #2) and then diminishes gradually as one moves distally. The rise in values seen at section #7 is an artifact of the fact that the stents are sufficiently long such that in some of the cases the distal end of the stent (and hence section #7) reaches the ostium of the next bifurcation. Not surprisingly then, the thicknesses at section #7 are similar in values to those at section #1.

5.1.2. Composition

The most striking clinically relevant aspect of a restenotic lesion is its physical size as described in the previous section. However, geometry alone is not sufficient to fully describe a restenotic lesion. An understanding of the composition of the lesion is critical to understanding its formation and the factors that determine its progression. Furthermore, a restenotic lesion is not simply a fixed passive obstruction. Rather, the activity or quiescence of the lesion components plays a critical role in the long term clinical outcome.

The large numbers of histological analyses that can be performed for any given section are beyond the scope of this work. Rather, we concentrate here on that which can be demonstrated simply, using the basic elastin stain to highlight tissue components, monoclonal antibodies to identify primary cellular components – e.g. smooth muscle cells, and Carstairs stain to delineate the primary extra-cellular component, fibrin (fig. 5-04).

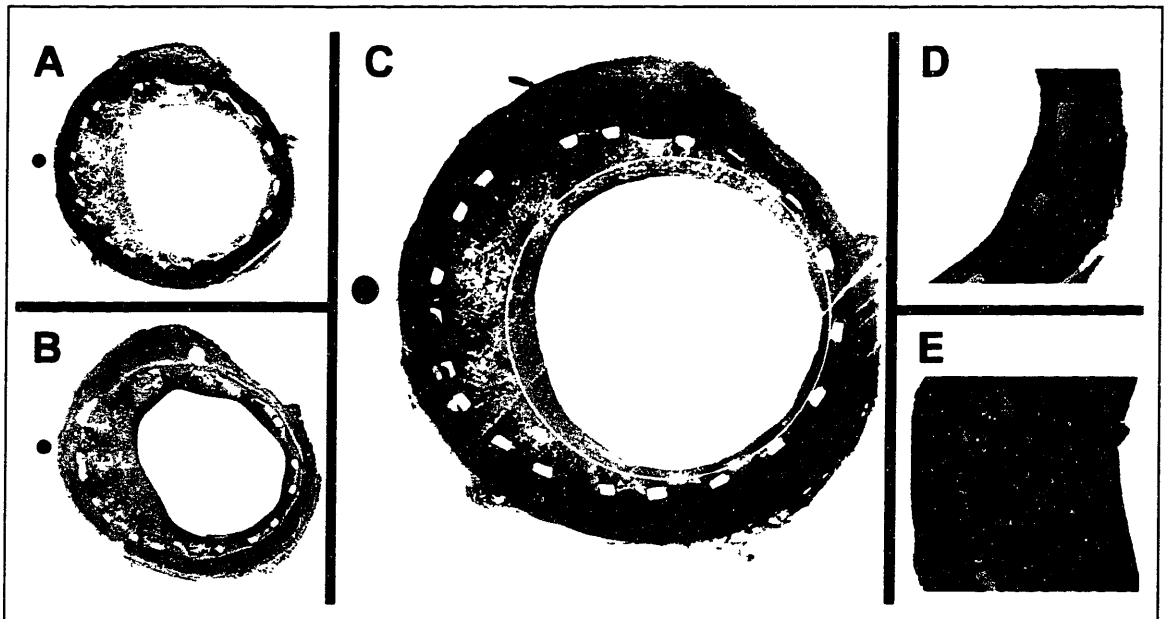

Figure 5-04: Chronic Lesion Composition. High magnification images of one of the sections of a chronic (14day) lesion. Verhoeff's elastin stain **(C)** shows a cellular/dense region of relatively uniform thickness (inside yellow circle) and an ECM-rich/sparse crescent region located on the lateral wall. Carstairs fibrin stain **(A)** demonstrates high concentrations of fibrin around the stent struts, particularly on the lateral wall. Smooth muscle cell alpha-actin stain **(B)** shows tightly packed smooth muscle inside along the lumen (inside of the hoop in C), with SMC-poor areas in the crescent region on the lateral wall. False colored enhancement of fibrin concentration (green in **(D)&(E)**) highlight the difference in ECM away from the struts in on the flow divider **(D)** and the lateral wall **(E)**.

The bulk of the chronic lesions can be divided into two regions with distinct properties. The inner region is roughly annular in shape. It is bounded by the lumen on one side and is 200-300 microns thick. The outer region is a crescent centered at the lateral wall. The inner annular region is dense with a high concentration of contiguous smooth muscle cells. This region is poor in ECM in general and fibrin in particular both around and in between stent struts. The crescent region is loose and re-vascularized. It is relative poor in smooth muscle cells and contains several 'holes' almost entire devoid of smooth muscle cells. Conversely, the crescent region is fibrin rich both around the stent struts and in the regions in between and away from the struts.

5.2. Effect of Side Branch Flow

The central hypothesis put forth in this thesis is that the interactions between different sites in the arterial tree affect the long-term outcome of vascular interventions. As a test for this, we examined the effect that side branch occlusion/dilation has on modulating the pattern of restenosis in the main branch. Based on the results of the bench top models, we predicted that a patent side branch would produce boundary layer separation on the lateral wall of the main branch. We further proposed that this region of disturbed flow would alter acute (discussed in the next chapter) and chronic events in such a way as to produce a lesion in the main branch that is substantially larger than if the side branch had been left occluded.

To test these predictions *in-vivo* we used the porcine iliac artery model described previously. Briefly, the side branch of the right iliac-femoral arterial bifurcation was percutaneously occluded. The main branches of both the left and the right bifurcations were then stented. Thus, the right side serves as a model for a bifurcation with an occluded side branch whereas the left side serves as a model for a bifurcation with a patent side branch. It is critical to understand that the goal of this was not to advocate the intentional occlusion of a side branch, but rather to examine the flow-mediated ramifications of a pre-existing side branch occlusion. The goal of these experiments would be to demonstrate that the extent of neo-intimal hyperplasia in the main branch on the left (side branch patent) side is substantially greater than on the right (side branch occluded) side.

One could argue that even if a disparity in lesion formation is observed, this effect has nothing to do with local flow patterns but rather the total rate of flow. When the side branch of a bifurcation is occluded, the total rate of flow through the main branch presumably increases. This would certainly be the case if the total flow into the bifurcation were constant. In reality, this is not the case, as the total flow is modulated by the downstream resistance. This resistance can increase or decrease because of selective vasoconstriction or vasodilatation of the distal vascular bed. Thus, in an occluded side branch case, one would expect the resistance downstream from the main branch to increase and the resistance of other vessels feeding the general region of the side branch

to decrease so that the total flow into the bifurcation will be reduced. Hence the proposed increase in flow in the main branch will be attenuated to some extent. The degree to which this happens is difficult to predict and absent an adequate method for *in-vivo* measurement, it is impossible to know just how much of a flow increase, if any, actually occurs. It is reasonable to assume however that there is at least a small increase in the total flow through the main branch as a result of side branch occlusion. Previous works have shown an inverse relationship between the total flow through a vessel and the degree of intimal-hyperplastic response[54]. It is thus incumbent upon us to show that not only is there a reduction in neo-intimal thickness in the main branch after occlusion of the side branch, but that this is truly a result of the effect on flow disturbance, as opposed to merely a reflection of the increased total flow.

In anticipation of this question, long stents were used. These stents cover the entire length of the main branch starting from the bifurcation of interest and extend distally to the next bifurcation, beyond the extent of the flow disturbance. Thus, when comparing the side branch occluded to the side branch patent side, the proximal to middle part of the stent differ by both the flow disturbance and the total flow whereas the distal part of the stent differs only by the total flow (fig. 5-05).

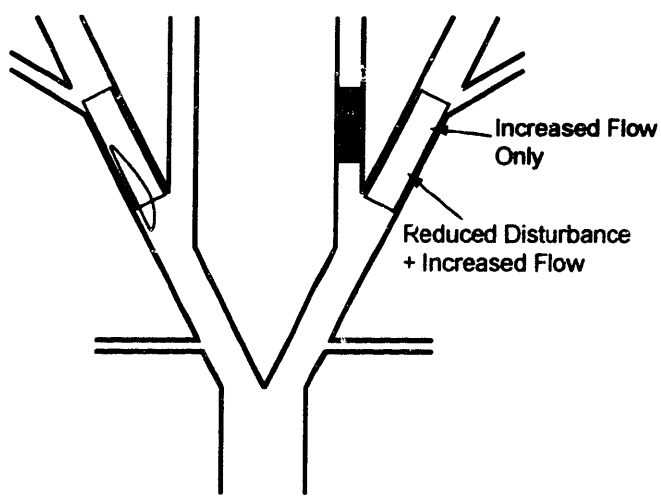

Figure 5-05: Multiple Effects of Side Branch Occlusion. Side branch occlusion causes total flow rates to be elevated everywhere in the main branch including the proximal and the distal parts of the stent. In contrast, differences due to flow disturbance should be prominent only in the proximal part of the stent.

If the increased total flow (assuming that indeed this is what occurs) is the dominant effect, one would expect the side branch occluded case to exhibit uniformly less neo-intimal hyperplasia along the entire length of the stent. Conversely, if the reduction of the extent of flow disturbance is the dominant effect, the side branch patent case should exhibit increased neo-intimal hyperplasia in the proximal part of the stent. This relative increase should diminish as one moves distally along the stent. Finally, at the distal end of the stent, the amount of neo-intimal hyperplasia on the side branch patent side should tend towards the side branch occluded side.

An important aspect of the theoretical and model prediction has to do with the ability of the main branch to remodel in response to side branch occlusion. We have put forth and modeled the notion that it is this chronic optimization of the main branch geometry to function within the context of an occluded side branch that makes it particularly ill-suited for functioning once the side branch has been dilated. To demonstrate this concept, the *in-vivo* experiments were performed in two versions: one which allows the main branch time to remodel between the time of side branch occlusion and main branch stenting, and a second whereby side branch occlusion is immediately followed by main branch stenting, thus not allowing the main branch time to remodel. Comparison between the results obtained from these two experimental outlines would demonstrate the relative importance of this effect.

5.2.1. Occlusion in the Presence of Main Branch Remodeling

The side branches of the right-sided iliac femoral arterial bifurcation of 3 pigs were percutaneously occluded as previously described. Briefly, a 'cone stent' was implanted distally in the side branch. Polymer microspheres were then injected into and trapped within the 'cone stent'. Finally, a second cone stent was implanted proximally in the side branch to prevent the microspheres from escaping under pulsatile flow. Animals were then allowed 28 days to recover. This period of time, which is considered a chronic follow-up period in this species, presumably allowed main branch remodeling to occur on the right side. 28 days post occlusion of the right-sided side branch, the main branches of

both the right and left sided bifurcations were stented with identical copper contaminated stents (fig. 5-06). These stents were of sufficient length to cover the entire main branch

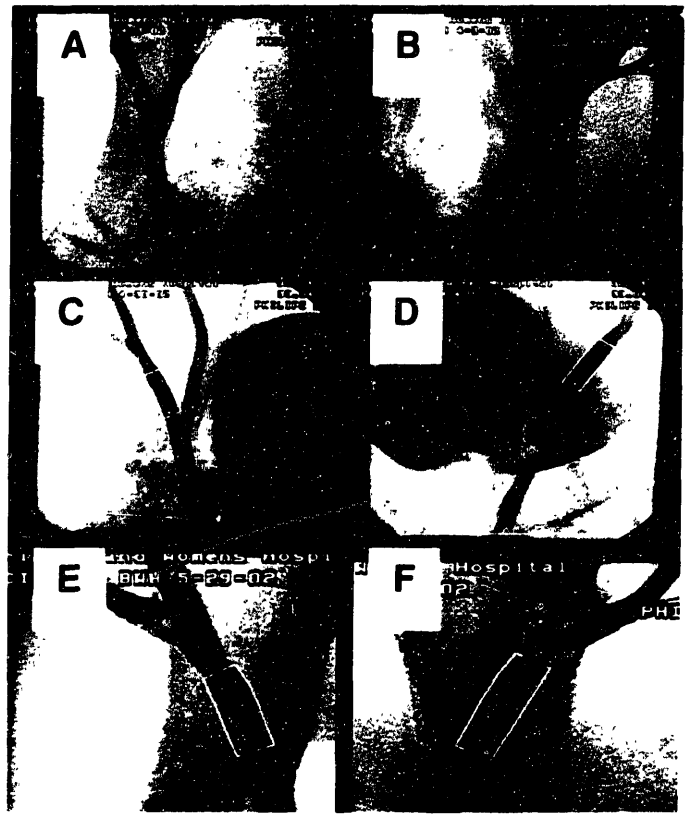

Figure 5-06: Chronic Response w/ Remodeling. Panels show angiographic sequence of events in the chronic experiment: Panels **(A)&(B)** show the left and right sided bifurcations respectively at baseline (day 0). The right sided side branch was then occluded (not shown) and the animals allowed to recover for 28 days. On day 28, the occlusion of the side branch was verified and the main branches stented with identical stents **(C)&(D)**. Yellow outlines indicate the location of the main branch stents. Animals were followed for an additional 28 days at the end of which the animals were re-imaged **(E)&(F)** and sacrificed for histological analysis. Note the lesion seen on the lateral wall of the side branch patent side **(E)**.

segment stretching from opposite the ostium of the side branch all the way distally to the next bifurcation. Animals were then followed for an additional 28 days to allow intimal hyperplasia to form in the main branch, and then sacrificed and the arteries excised for histological analysis as previously described.

Each animal was first analyzed on an individual basis to show the qualitative pattern of neo-intimal hyperplasia in the side branch occluded vs. the side branch patent side (fig. 5-

07). For each animal, the differences in pattern of hyperplasia between the side branch

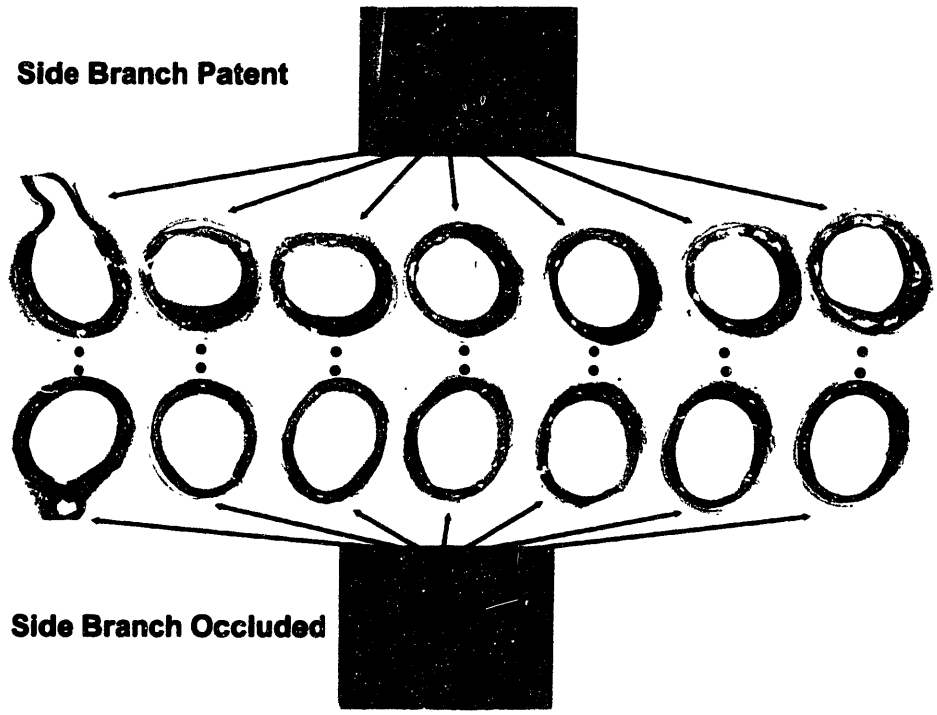

Figure 5-07: Occluded vs. Patent Side Branch Lesion Map. Three dimensional recreation of the morphometry of neo-intimal hyperplasia in a main branch stent in one animal. Top series shows the resultant lesion in the side branch patent case, whereas the bottom series shows the lesion in the same animal in the side branch occluded case. Blue dots mark the lateral wall of the bifurcation. The original excised bifurcations are shown for reference. Note the eccentric lesion located at the lateral wall in the first four sections of the side branch patent case as compared to the symmetrically thin neo-intima in the side branch occluded case.

patent and occluded side are immediately apparent: The volume of neo-intimal growth on the side branch patent side is significantly larger than on the side branch occluded side. This additional growth is distributed eccentrically centered at the lateral wall. As one moves towards the more distal sections, the two sides become very similar.

Before one can produce a more quantitative result based on numerous animals, one must first account for the different possible sources of variability including:

1) Intra-animal variability: Implantation of an endovascular stent is a manual process that includes an inherent variability in several respects including for example the

degree of mechanical injury imparted to the vessel wall. Furthermore, despite their outward similarity, there is no way to ensure that the left and the right bifurcations in a single animal are indeed identical in every way. These factors and others may very well introduce variability in the degree of neo-intimal hyperplasia in one stent versus another.

2) Inter-animal variability: Even assuming identical technique and stents are used in every single animal, the formation of neo-intimal hyperplasia is a multi-factorial biological process such that its precise extent is dependant on the individual animal used.

The few cases in which side branch occlusion was unsuccessful yielded an important control wherein the two sides in the same animal received essentially the same treatment.

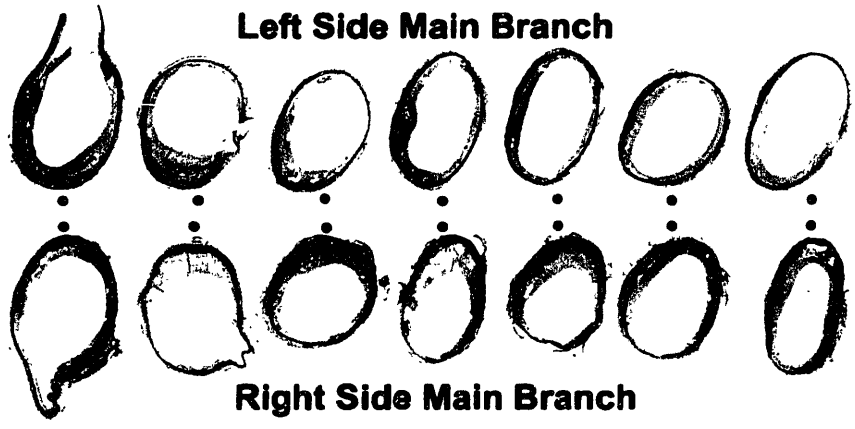

Figure 5-08: Intra-Animal Variability. One example of an animal in which side branch occlusion was unsuccessful. The pattern of neo-intimal hyperplasia on both sides is indistinguishable, demonstrating that the intra-animal variability that can arise from differences in technique or other local factors is small.

This allows us to examine the intra-animal variability (fig. 5-08). When the left and the right sided main branches of these animals are compared the intra-animal variability is very low. Both sides in this case have a similar appearance to the left (patent side branch) side seen in fig. 5-07, demonstrating that the technique itself is relatively stable and repeatable.

The right (side branch occluded) sided main branch was regarded as reflective of the basal degree of neo-intimal hyperplasia for each animal. Thus, to account for inter-animal variability, all measurements were normalized to the average of the same

measurements obtained in sections 2-6 on the right side. Another source of inter-animal variability is the length of the main branch from the iliac-femoral bifurcation to the next bifurcation downstream. Since long stents were used to cover this entire length, on those animals that had relatively short segments, the distal end of the stent extended into the more distal bifurcation. This was not felt to be a significant source of variability for the more proximal sections; however it did introduce a large variability in the most distal section. For this reason, only the 6 most proximal sections were included in the analyses. Three different types of measurements were made and then averaged across all animals:

1. Averaged neo-intimal area (fig. 5-09): The total area of neo-intima, defined as the area confined between the lumen and the internal elastic lamina, is a commonly used indicator

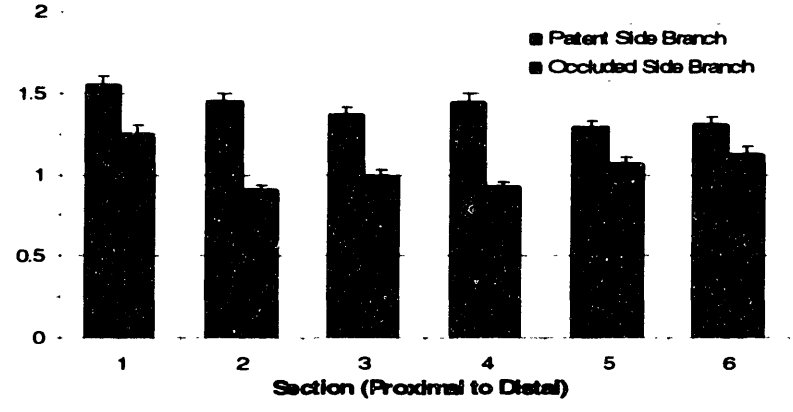

Figure 5-09: Modulation of Neo-Intimal Area. Averaged (n=3 animals) normalized neo-intimal area for the patent vs. occluded side branch case. The difference between the two cases grows rapidly in the proximal part of the stent and then diminishes and becomes insignificant in the more distal sections.

for the severity of neo-intimal hyperplastic response. The pattern for the occluded side branch case is the one normally seen with most stent types. The intimal response is worst at the proximal and distal ends of the stent and minimal in the middle. In contrast, the side branch occluded case exhibits a more uniform pattern. The difference between the two cases grows rapidly in the proximal segment and then shrinks towards the distal sections.

2. Averaged neo-intima to media ratio (fig. 5-10): The ratio between neo-intimal and medial area is another parameter commonly used to quantify hyperplastic response. The

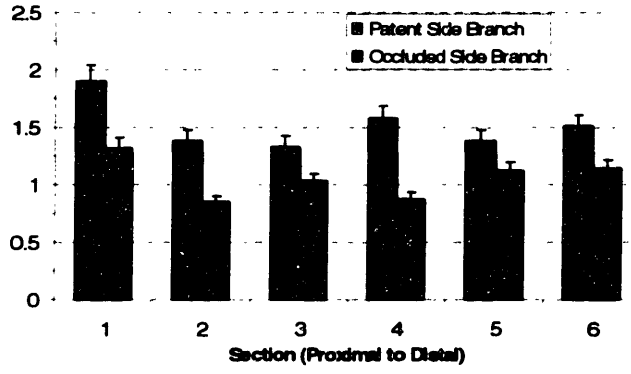

Figure 5-10: Modulation of Neo-Intima to Media Ratio. Averaged (n=3 animals) normalized neo-intima to media ratio for the patent vs. occluded side branch case.

advantage of this parameter is that the neo-intima in each section is internally normalized to the media thus controlling for artifacts due to processing for example. The disadvantage is that given the larger number of variables involved, the metric of error tends to be larger. The results here essentially recapitulate those seen with the intimal area analysis.

3. Averaged luminal area (fig. 5-11): Generally, luminal area is affected by intimal hyperplasia on one hand, and by (positive or negative) remodeling on the other. In a stented vessel, remodeling plays little if any role. Thus, not surprisingly, the picture obtained from average analysis of luminal area is very nearly exactly the mirror image of the intimal area (compare to fig. 5-09), i.e. significantly more cross sectional area available for flow in the proximal sections of the side branch occluded case and nearly no difference in the distal sections.

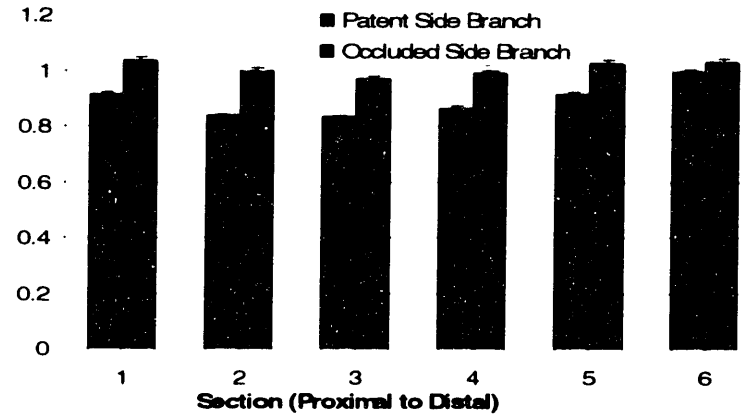

Figure 5-11: Modulation of Luminal Area. Averaged (n=3 animals) normalized luminal area for the patent vs. occluded side branch case. The cross section available for flow is larger when the side branch is occluded. The difference between the two cases disappears in the distal sections.

5.2.2. Occlusion in the Absence of Main Branch Remodeling

To examine the role of main branch remodeling in the effect side branch occlusion has on neo-intimal hyperplasia, the same experiment described in the previous section was performed again with one important difference. Whereas in the previous experiment, the time between side branch occlusion and main branch stenting was 28 days, in this experiment this was reduced to 3 days (fig. 5-12). Technically, it is possible to occlude the side branch and then stent the main branches concomitantly. However, it was felt that by performing these two procedures at the same time the right sided main branch would be affected by the active biological processes involved in occlusion of the adjacent side branch. Thus, we allowed three days to elapse between the two interventions so that the side branch would have an opportunity to become somewhat more quiescent.

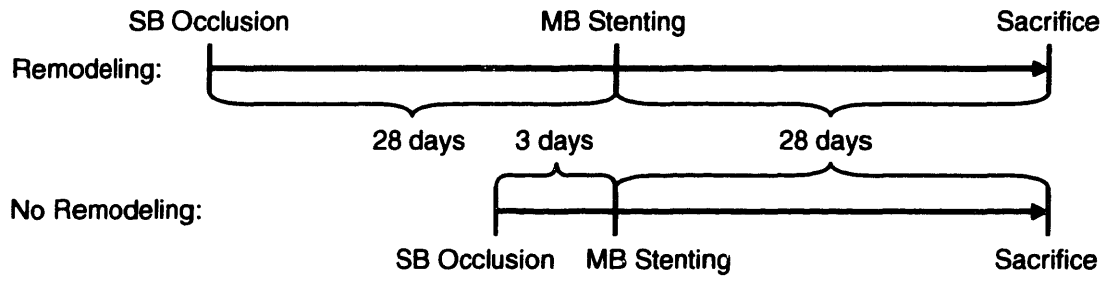

Figure 5-12: Experimental Design for Remodeling vs. Non-Remodeling. In the previous experiment (top) 28 days elapsed between side branch occlusion and main branch stenting thus allowing main branch remodeling to occur. In the current experiment (bottom), main branch stenting occurs just three days after side branch occlusion thus minimizing the influence of main branch remodeling.

The analyses of intimal area (fig. 5-13), of intima to media ratio (fig. 5-14) and of luminal area (fig. 5-15) were repeated as was done for the case with remodeling. When

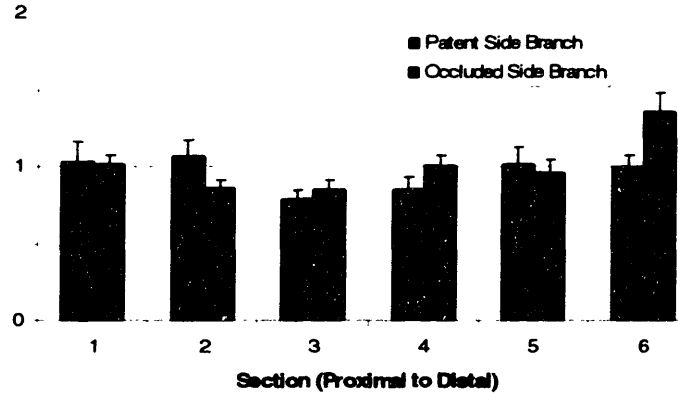

Figure 5-13: Effect of Main Branch Remodeling on Intimal Area. Averaged (n = 3 animals) normalized intimal area of the main branch in the absence of remodeling.

the main branch was not allowed to remodel in response to side branch occlusion prior to stenting, the differences previously seen between the side branch occluded and side branch patent side disappear (contrast figs. 5-13,14&15 to figs 5-09,10&11).

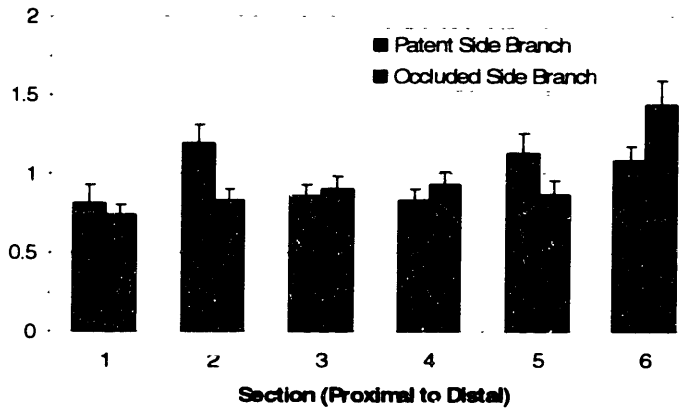

Figure 5-14: Effect of Main Branch Remodeling on Neo-Intima to Media Ratio. Averaged (n = 3 animals) normalized I/M ratio in the main branch in the absence of remodeling.

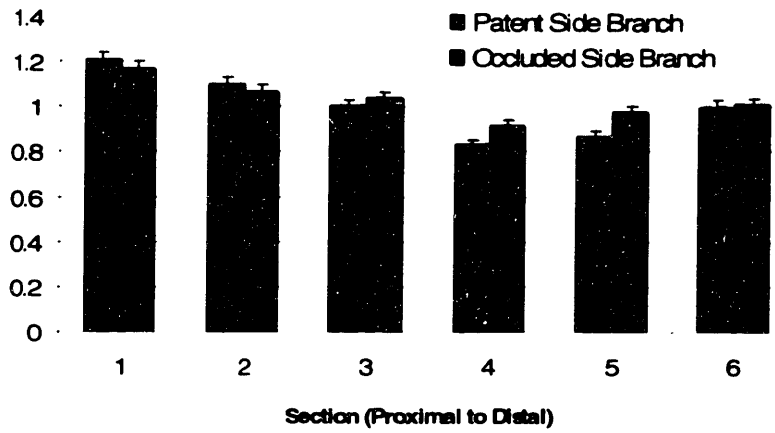

Figure 5-15: Effect of Main Branch Remodeling on Luminal Area. Averaged (n = 3 animals) normalized luminal area of the main branch in the absence of remodeling.

5.3. Discussion

The morphology of the chronic restenotic lesion correlates strikingly with the location, shape and extent of flow disturbance seen in the bench-top models. The lesions in the patent side branch case all begin immediately opposite the ostium of the side branch, are all located eccentrically on the lateral wall and all diminish as one proceeds distally along the stent length. All of these findings are in good agreement with the idea that the region of boundary layer separation would dictate lesion development (compare fig. 5-02 and fig. 3-08). First and foremost, these findings provide validation for the use of the models

employed. Additionally, the ability to economically make accurate *a-priori* predictions regarding clinically relevant phenomena with relatively simple modes of analysis carries several important implications:

a) The process of formation of neo-intimal hyperplasia is complex, affected by numerous physical, chemical and biological factors. The bench-top models used in this study simulate only one aspect of these conditions – flow pattern. That despite this obvious limitation, the models are still able to predict lesion geometry with a high degree of accuracy speaks to the relative importance of flow disturbance in determining the geometry of neo-intimal hyperplasia.

b) The link between flow disturbance and hyperplasia and restenosis, while postulated[55], has not been established to the same degree of certainty as that between flow disturbance and atherogenesis. While still not constituting proof, these data offer strong support for the notion that flow disturbance indeed plays a central role in restenosis as well.

c) As mentioned previously, the analysis performed here is of a generalized nature. Only the primary, largest scale flow patterns were taken into account, while ignoring the secondary and finer flow phenomena. Furthermore, the local disturbances such as for example would be caused by stent struts and/or imperfections in the arterial vascular wall were not even a component of the model. The success in predicting lesion geometry based on such a 'high level' analysis indicates the contribution of these 'large scale' phenomena in determining ultimate lesion formation. This of course does not mean that a finer analysis is not warranted or does not offer additional insight, merely that for certain applications, generalizations can in fact be made for a wide variety of patients without taking into account infinite levels of detail.

The composition of the restenotic lesion (fig. 5-04) is interesting in that it seems to indicate the presence of two distinct processes, one inside the 'crescent' and another inside the 'annulus'. The 'crescent' process is asymmetric, fibrin rich and relatively smooth muscle cell poor. It has a much sparser cell distribution and substantially more extra cellular matrix. In contrast, the 'annulus' process is relatively uniform, smooth muscle cell rich and fibrin poor. This region is tightly packed with smooth muscle cells

and has a more healthy/normal appearance similar to what one would see in a normal media. One possibility is that the properties of the 'crescent' region are those that are determined by boundary layer separation, while those of the 'annulus' are a uniform 'healing response' that occurs as a result of vascular injury regardless of the pattern of flow. A further investigation of these differences is warranted, but is beyond the scope of this work.

The occlusion or lack thereof of the side branch in the bifurcation had a profound effect on the extent and geometric pattern of hyperplasia in the main branch. Occlusion of the side branch essentially eliminated the adverse effect that the bifurcation has on the extent of hyperplasia, reducing it instead to what one would expect to see in a normal non-bifurcating vessel (see fig. 5-07, bottom). From the point of view of neo-intimal area, neo-intima to media ratio and luminal area (figs. 5-09 – 5-11), side branch occlusion served in a protective role with respect to main branch restenosis. The difference between the two cases behaves in the same manner as the difference between them in flow disturbance, thus providing a mechanistic basis for these observations. Furthermore, the difference between the side branch patent and the side branch occluded case is axially variable and tends to zero at the distal end. This strongly suggests that the difference between the two cases is indeed from a localized flow disturbance in the side branch patent case, as opposed to a modulation of the total rate of flow (see fig. 5-05).

Analysis of the data for side branch occlusion in the absence of main branch remodeling (figs. 5-13 & 5-14) shows that in the absence of main branch remodeling the differences between the side branch patent and the side branch occluded cases become random and insignificant. Thus, chronic main branch remodeling seems to play a critical role in the 'protective' nature of side branch occlusion. The precise nature of this remodeling has not been demonstrated here. Whether these are geometric changes, functional cellular changes other factors or some combination of all these cannot be shown based on these data, however this is a powerful demonstration of the concept discussed previously i.e. that once side branch occlusion has been present for many years, one can never 'return the system to its original state'.

6. Acute Response

The bench-top models have shown the physical stimuli that occur in bifurcations and how those physical stimuli are modulated with modulations of the geometry of the vessels. At the other end of the spectrum, the chronic *in-vivo* experiments have shown the ultimate result of these initial physical stimuli. This last section deals with the link between the chronic response and acute stimulus – the acute response.

The acute response phase of restenosis is thought to be primarily an inflammatory process. The early adhesion of neutrophils is followed by the recruitment and infiltration of circulating monocytes into the arterial wall where they become activated tissue macrophages. The macrophages themselves make up a non-negligible portion of the bulk of the ultimate lesion. In addition, their primary effect is the secretion of chemotactic and pro-proliferative factors leading to ultimate smooth muscle cell proliferation. We were thus interested in looking at the pattern of inflammatory cell adhesion with respect to the asymmetric geometry of the bifurcation, and how this pattern would be modulated by changes in the neighboring vessel.

6.1. Geometric Pattern of Leukocyte Distribution

6.1.1. Early Adhesion

Immediately after vascular injury, leukocytes begin to adhere to the vessel wall. The process of adhesion contains several phases:

1. Since blood leukocytes do not have the capability to 'steer' themselves, recruitment must begin through the passive collision between the leukocyte and the vessel wall. These collisions are dictated by the geometry of the vessel and the blood flow pattern, and are presumably independant of the presence of vascular wall injury.

2. A 'rolling adhesion' phase during which the leukocyte is only lightly bound to the vessel wall. This stage is thought to be primarily supported by the Selectin family of molecules including those that interact with platelets (P-type), leukocytes (L-type) and endothelial (E-type) Selectins.

3. Finally, a firm adhesion process occurs, during which the leukocyte becomes transfixed to the vessel wall through specific integrins expressed on the leukocyte as well as the wall itself including MAC-1, ICAM-1 and VCAM-1.

Thus, the early pattern of leukocyte distribution may reflect any one of:

a) The rate of passive leukocyte arrival at any specific location.
b) The state of binding molecule expression at the specific location.
c) Forces that act on the leukocyte and the vessel wall during the binding process.

To elucidate this early pattern of adhesion, the main branch of the femoral bifurcation of pigs was stented as previously described. The animals were then sacrificed at an early time-point (48 hours) and the arteries excised, processed and stained for CD45+ cells (macrophages) while noting the circumferential distribution as previously described.

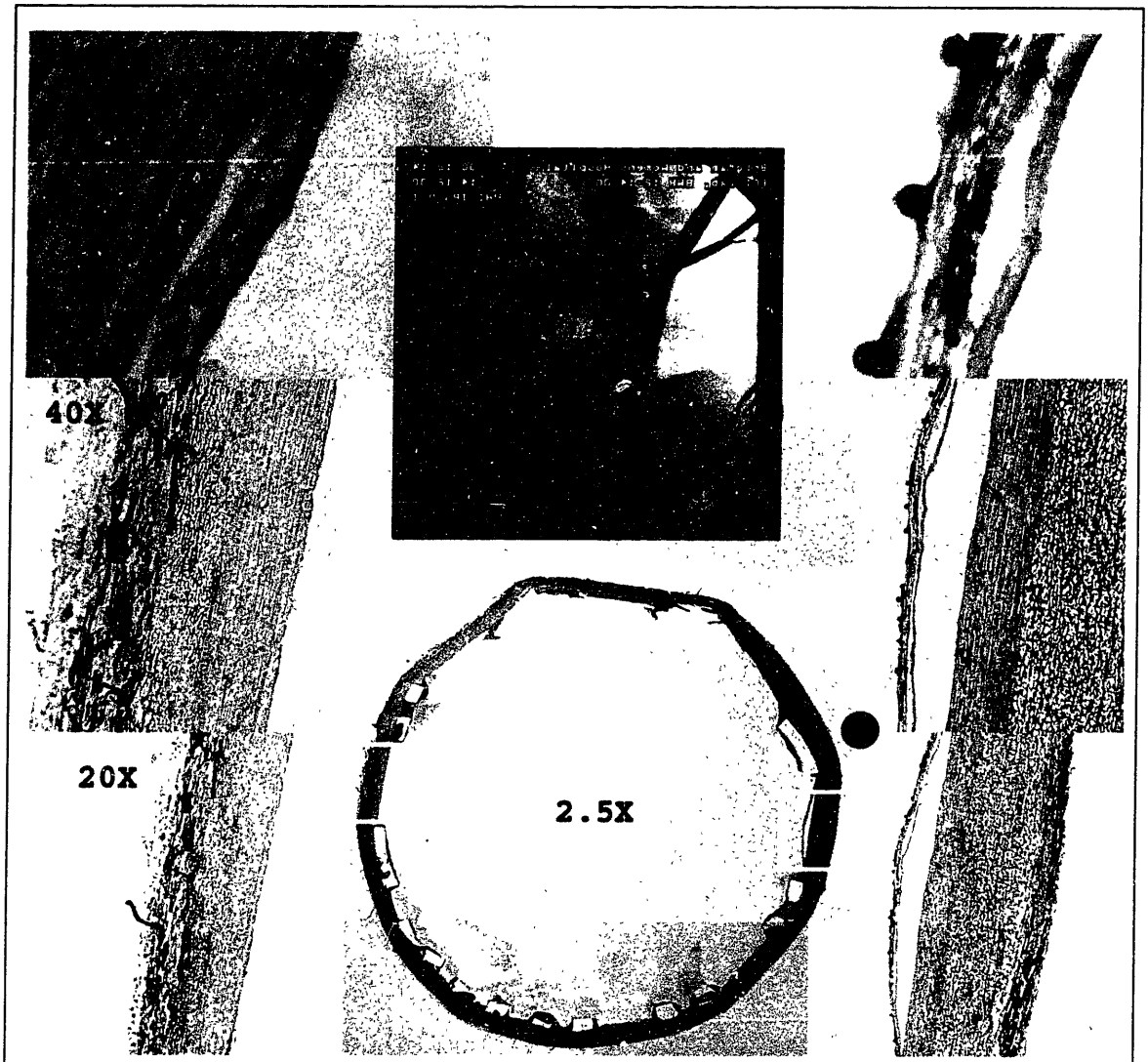

Figure 6-01: Acute Monocyte Adhesion. CD45 immunostain of artery stented with Palmaz P-108 stent at 48 hours. The central top panel shows an angiogram of the original bifurcation in-vivo. The red line on the angiogram denotes the longitudinal level at which the section was taken. The central bottom panel shows the entire cross-section. The blue dot represents the lateral wall. The yellow boxes denote the two regions of interest at the lateral (right) and the flow divider (left) walls. The panels on the right and left show successive magnifications of the regions of interest. Note the carpeting of adherent monocytes on the lateral wall in comparison to the complete absence of monocytes on the flow divider wall at this early stage.

A representative section (fig. 6-01) shows the resulting asymmetric pattern of leukocyte adhesion. The lateral wall shows a dense 'carpeting' of macrophages.

individually adherent to the vessel wall. As the angular orientation shows, this region of leukocyte concentration correlates to the region of boundary layer separation noted in the models. In contrast, the flow divider wall, which exhibits a region of high shear stress in the models, is completely spared of macrophage adhesion at this early stage.

6.1.2. Accumulation

As more time progresses after initial injury, leukocytes continue to accumulate on the vessel wall. Eventually, the entire surface of the vessel wall is coated by leukocytes (primarily macrophages). This initial neo-intimal layer begins to express extra-cellular components such as collagen and fibrin. As this happens, additional leukocytes are accumulated by adhesion either to the extra-cellular matrix itself or to the leukocytes already there. This self-amplifying process is strictly pathological i.e. it would not occur in the absence of injury. The accumulating leukocytes express and secrete chemotactic as well as growth factors that eventually lead to the migration, activation and proliferation of smooth muscle cells that make up most of the bulk of the restenotic lesion.

To demonstrate the relation between this cumulative process and the flow pattern, the main branch of the femoral bifurcation of pigs was stented as previously described. The animals were then sacrificed at 72 hours and the arteries excised, processed and stained using Gill's H&E stain. Microscopic analysis of these animals' arteries (fig. 6-02) shows that at this early time point, the only cellular components of the neo-intima are macrophages, which make up the vast majority of cells and a small percentage of neutrophils. There is also a significant component of extra-cellular matrix.

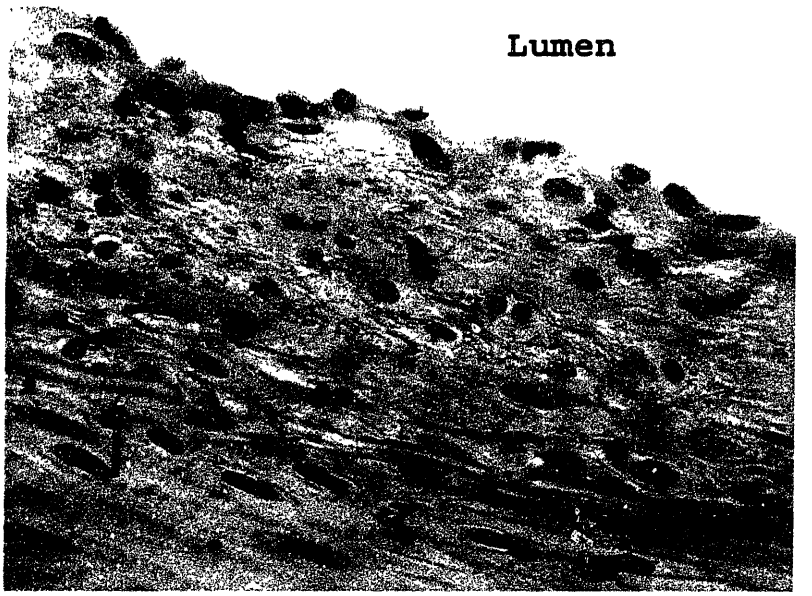

Figure 6-02: Acute Neo-Intima. Hemotoxylin and Eosin stain of acute accumulation of leukocytes. Animal was stented and then sacrificed at 72 hours. All cells in the neo-intimal layer are leukocytes based on morphology. Note the extensive presence of extra-cellular matrix. Black arrow points to the internal elastic lamina.

The thickness of the neo-intimal layer at this time point is variable. Regions immediately adjacent to the stent struts exhibit a local 'flame' of inflammation, most likely reflective of the local flow disturbance as well as the excessive injury. In contrast, the regions in between the stent struts exhibit a more uniform layer of leukocyte adhesion. Thus, for purposes of comparison between the lateral and the flow-divider walls, the regions in between the struts were analyzed on both sides (fig. 6-03).

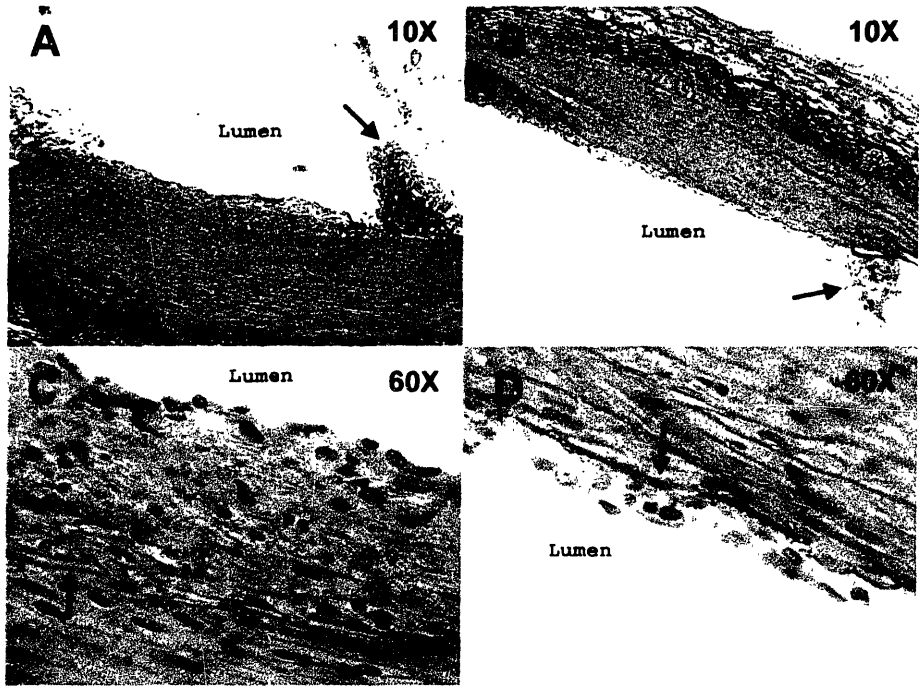

Figure 6-03: Accumulation On Opposite Walls. Accumulation of leukocytes at 72 hours on the lateral wall (A&C) and the flow divider wall (B&D). Edges on the 10X images show the localized 'flame' (arrows) of inflammation around the stent struts. Arrows on the 60X images point to the internal elastic lamina. Note the significant difference in accumulation between the lateral wall (C) and the flow divider wall (D).

Thus, on a single-section basis there is a large discrepancy between the accumulation on the lateral wall and the flow divider. The lateral wall is covered by a multiple-cell layer of macrophages, rich in extra-cellular matrix. The flow divider wall, on the other hand, is only covered by a single or double cell layer that is loosely adherent to the original vessel wall.

To quantify the entire three dimensional structure of this early process, the number of inflammatory cells per high power field was counted on each wall. As this number is somewhat subjective, the operation was performed in triplicate for each wall, with the number of cells averaged and then compared to the opposite wall (fig. 6-04).

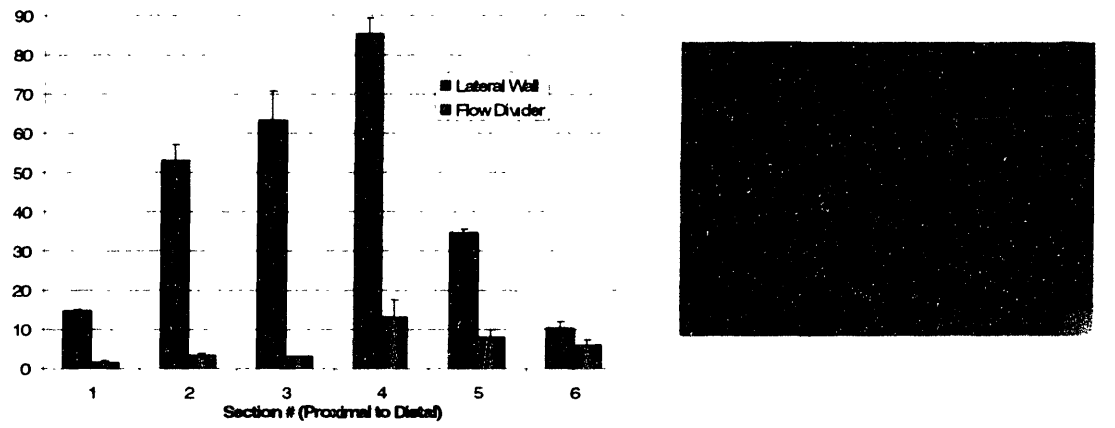

Figure 6-04: Inflammatory Cell Count. Panel on the left shows the number of inflammatory cells per high power field of the lateral wall and the flow divider of a single animal. Panel on the right shows the original bifurcation ex-vivo, marked with the location of the six sections from proximal to distal. Note the difference between the lateral wall and the flow divider as a function of position along the stent. The difference starts out small, grows with distance along the stent, and ultimately shrinks back as one proceeds away from the bifurcation.

The qualitative pattern of accumulation (see fig. 6-04) is conserved both in the circumferential and the longitudinal dimension for nearly all individual animals. For each animal, the lateral wall accumulated significantly higher numbers of leukocytes. For each animal, this difference grew towards the middle of the stent and then decreased as one moved distally away from the bifurcation. The absolute numbers of cells however, show inter-animal variability. Thus, to produce an averaged pattern for multiple animals, it was necessary to devise a scheme for normalization of the leukocyte count. In a separate part of this experiment (discussed below), the side branch of the contra-lateral bifurcation was occluded. As will be shown, this procedure effectively reduces the main branch to the equivalent of a normal non-bifurcating vessel with uniform leukocyte accumulation. This (side branch occluded) bifurcation then allows for normalization of both bifurcations for the baseline level of accumulation in the following manner:

a) The number of leukocytes on both walls (lateral and flow divider) of the SB-occluded bifurcation was averaged along the entire length of the stent. This number is characteristic of the level of response typical for that individual animal

b) The number of leukocytes for each section (1-7) on both walls was counted in triplicate, averaged and then normalized by the number produced in step (a).
c) The individual, normalized section counts were averaged for all animals to produce an overall picture of the leukocyte accumulation.

The average pattern of leukocyte accumulation (fig. 6-05) bears the same qualitative characteristics as the individual patterns, with the exception of the first section. This is likely from the difficulty in precise positioning of the stent on the resolution of a single section. This results in a large degree of variability in the location of the first section with some stents beginning within the bifurcation itself and others slightly distally. The averaged data show opposite trends for the lateral wall and the flow divider. The lateral wall accumulations start low, increase towards the middle of the stent and then decrease towards the distal end. In contrast, the normalized average flow divider accumulations for the proximal sections are significantly less than one, and increase towards one as one moves distally.

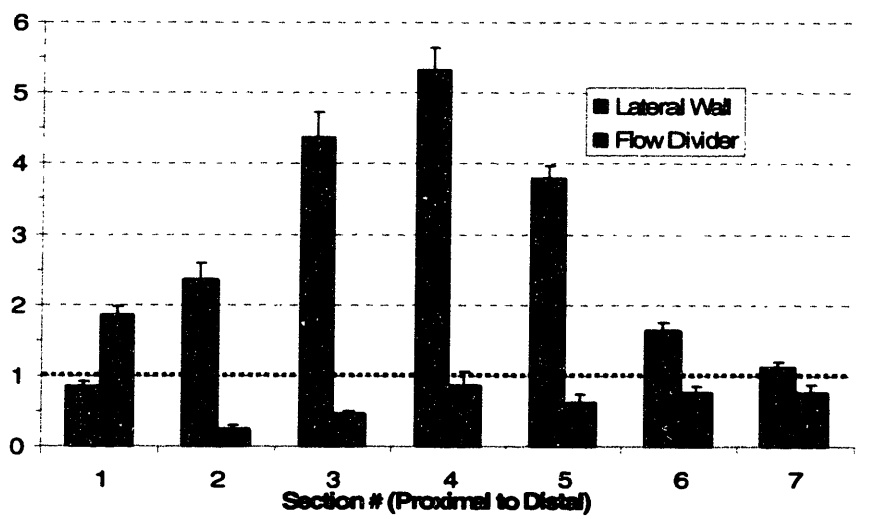

Figure 6-05: Average Leukocyte Accumulation. Normalized number of inflammatory cells per high power field averaged across all animals (n=3). Note the opposite patterns for the lateral wall vs. the flow divider. The large number of leukocytes on the flow divider at section number one is most likely a result of variability in stent positioning. Note also that values for the flow divider start at considerably less than one.

6.2. Side Branch Occlusion

To see how side branch flow affects the early neo-intima, the side branch of the femoral bifurcation of pigs was occluded as previously described. The side branch on the right side was occluded, whereas the one on the left side was left patent so that the two states could be compared to each other. The animal was then followed for 28 days to allow remodeling of the bifurcation on the right side to occur. After 28 days, the main branches of both bifurcations were stented using identical copper contaminated stents as previously described. Animals were then sacrificed 3 days after stenting and the bifurcations processed as previously described and stained using Gill's H&E stain. Two types of analyses were performed to quantify the neo-intima:

1) Adherent leukocyte count: The number of surface adherent inflammatory cells were counted, normalized and averaged as described above. Briefly, the leukocyte count on the right side (the one with the occluded side branch) was averaged for each animal and used to normalize both the right and the left sides. The ratio between the number of cells on the lateral wall and the number of cells on the flow divider was then calculated for each section along the length of the stent. The ratios were then compared between the right (side branch occluded) and the left (side branch unoccluded) case.
2) Neo-intimal thickness: The thickness of the neo-intima is determined by the number leukocytes present, and the amount of extra-cellular matrix. The thickness (lumen to internal elastic lamina) was measured for each slide at the lateral and the flow divider wall (performed in triplicate for each location). All thicknesses for each animal were normalized by the thickness of the flow divider wall of the third section on the right side.

The average number of leukocytes (fig. 6-06) is dramatically affected by side branch occlusion. The number of leukocytes on the left (side branch unoccluded) side increases dramatically towards the middle of the stent, only to shrink back as one moves away from the flow disturbance. In contrast, the number of leukocytes on the right (side branch occluded) side remains fairly constant along the entire length of the stent.

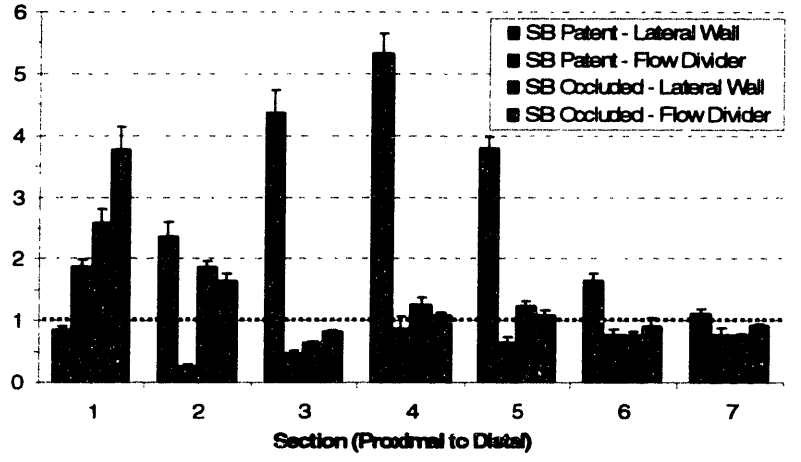

Figure 6-06: Effect of Side Branch Occlusion on Average Leukocyte Count. Leukocyte count per high power field on the side branch unoccluded side increases as one moves distally from opposite the ostium of the side branch, followed by a decrease towards the distal edge of the stent. In contrast, the side branch occluded side exhibits a relatively constant rate of leukocyte accumulation along the length of the stent. The abnormal results in the most proximal section are most likely a result of the inaccuracy of stent deployment at this location.

Another important difference in leukocyte accumulation between the side branch occluded and unoccluded sides is the degree of asymmetry between the lateral and the flow divider walls. As demonstrated in fig. 6-06, the side branch unoccluded side is highly asymmetric with the lateral wall exhibiting high numbers of leukocytes and the flow divider wall exhibiting much lower numbers. The number of leukocytes on the flow divider wall is lower than that at both walls on the side branch occluded side, a fact that shall be discussed later. The flow divider wall, on the other hand, has a very symmetric pattern of accumulation with very similar numbers of leukocytes adherent to the lateral and the flow divider walls. To highlight this difference in asymmetry, it is instructive to plot the ratio between the number of leukocytes on the lateral and the flow divider wall for both the occluded and the unoccluded side branch case. This plot (fig. 6-07) shows that the maximal degree of asymmetry on the left (side branch unoccluded) side occurs immediately distal to the proximal end of the stent, and then gradually decreases as one moves distally. On the right side, the ratio between the accumulations on the lateral and the flow divider walls is very close to unity throughout the length of the stent.

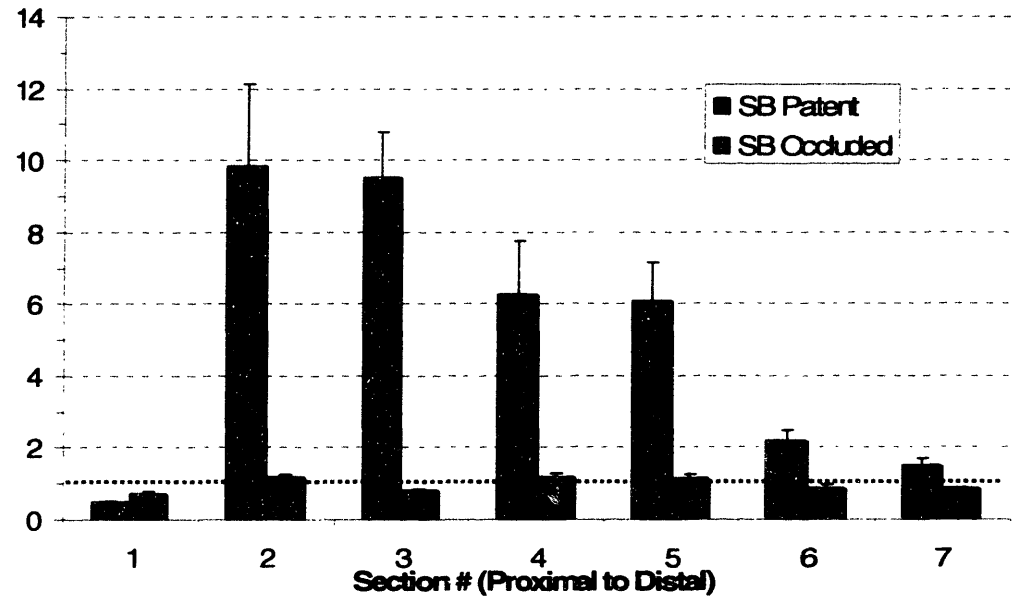

Figure 6-07: Effect of Side Branch Occlusion on Leukocyte Asymmetry. Patterns of leukocyte accumulation asymmetry are vastly different on the side branch occluded and unoccluded sides. On the unoccluded side, the asymmetry is maximal at the proximal end and decreases distally. On the side branch occluded side, there is very little asymmetry on any section along the length of the stent. The orange line denotes unity.

The average acute neo-intimal thickness (fig. 6-08) displays similar characteristics to that of the average leukocyte count. On the left (side branch unoccluded) side, the thickness on the lateral wall peaks early close to the proximal end of the stent and decays towards as one moves distally. On the flow divider wall, the thickness is uniform along the length of the stent at a value that is very similar to that of the thickness on the right side.

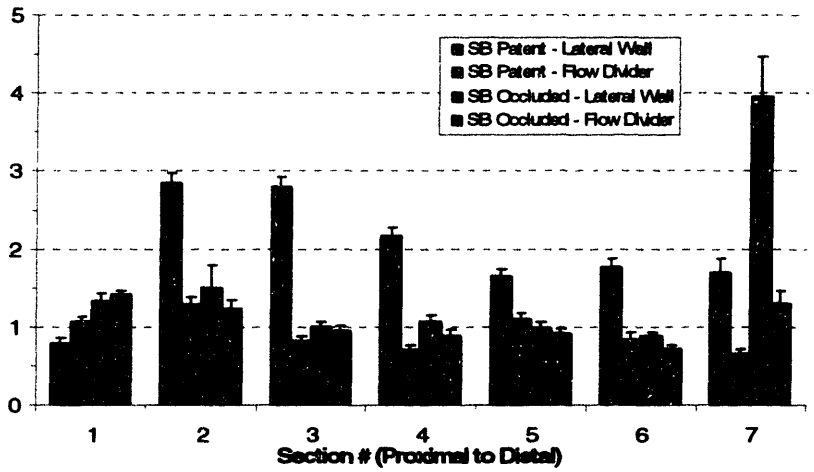

Figure 6-08: Effect of Side Branch Occlusion on Acute Neo-Intimal Thickness. Occlusion of the side branch (right side) modulates the pattern of neo-intimal thickness on the main branch stent at 72 hours post implantation. On the right side, the neo-intima is uniform along the length of the stent (the large peak on section #7 is likely due to the distal end of the stent protruding into the next bifurcation downstream). On the left side, the flow divider wall has a similar response to that on the right side. The lateral wall however, has significantly more neo-intimal hyperplasia which peaks proximally and attenuates distally.

Similar to the pattern of leukocyte accumulation, we can obtain an index of asymmetry by dividing the neo-intimal thickness on the lateral wall by that of the flow divider for each section (fig. 6-09). Once again, this shows that the process on the right (side branch occluded) side is fairly symmetric. On the left side, the asymmetry is greatest at the middle of the stent and roughly diminishes as one moves distally.

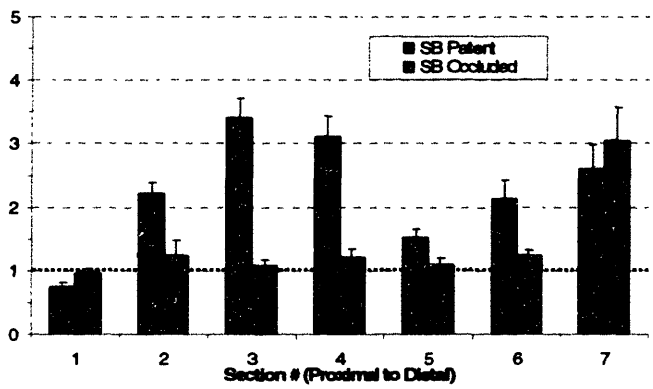

Figure 6-09: Effect of Side Branch Occlusion on Acute Neo-Intimal Asymmetry. Ratios of neo-intimal thicknesses at the lateral wall vs. the flow divider for the left (side branch unoccluded) and the right (side branch occluded) sides. The orange line denotes unity.

6.3. Discussion

The spatial pattern of leukocyte adhesion along the length of the stented segment soon after vascular intervention reflects the rate of passive leukocyte arrival, the state of binding molecule expression and the forces that act on the leukocyte as well as the vessel wall during the binding process. All of these can be related to the global flow pattern in general and to regions of boundary layer separation in particular. The flow models demonstrate vastly divergent conditions occurring at the lateral wall and the flow divider of the main branch of a (patent side branch) bifurcation. Flow at the lateral wall is dominated by a region of boundary layer separation with the associated re-circulating flow and relatively low shear stress. The flow divider, on the other hand, is characterized by generally high shear stress relative to anywhere else in the bifurcation as well as other sites proximal and distal to the bifurcation.

The region of re-circulating flow is in no way completely isolated from the main body of flow. Indeed, not only is there significant mass transfer in and out of the re-circulating region, but the region of re-circulation itself moves, grows and shrinks in size during each pulse cycle. That said, the residence times for all blood cells, including leukocytes, in this region are clearly longer than in other regions of the bifurcation and the arterial tree. Thus, the odds and the time spans of leukocytes coming in contact with the arterial wall in this region would be expected to be elevated. This increased probability of contact between the passive leukocyte and the arterial wall would be expected to enhance the rate of early adhesion.

A detailed discussion of the effects of low shear stress on the expression of surface binding molecules on the arterial wall is beyond the scope of this work. Briefly, previous works have established a primary role for shear stress in modulating the level and activation of a host of cell-surface adhesion molecules. Abnormally low shear stress has been shown to greatly increase the number of such binding sites and through this the rate of leukocyte adhesion. This type of effect has been implicated in the original localization of atherogenesis, and its extension to intimal-hyperplastic response post stenting is all but obvious. Once again, the difference in shear stress between the two walls of the main branch is profound with the lateral wall and the flow divider experiencing decreased and increased shear stress respectively.

Irrespective of the probability of contact and the state of binding molecule expression, firm adhesion and ultimately extravazation of leukocytes to the arterial wall is not a foregone conclusion. Between the initial contact and light rolling adhesion, and the ultimate tight adhesion, the leukocyte is subject to forces imposed on it by the flowing blood on one hand and binding molecules on the other (fig. 6-10). As the force exerted

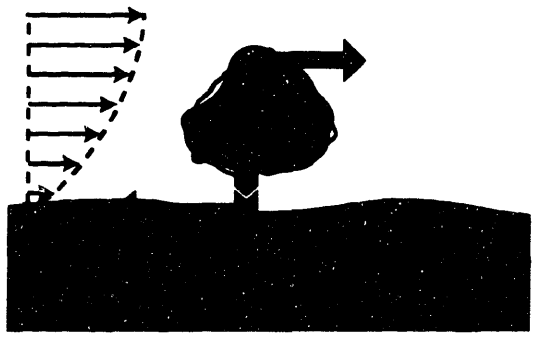

Figure 6-10: Forces on Leukocyte During Adhesion. A leukocyte (green) initially binds to the arterial wall (brown) through a set of integrins (purple). During this time, it is subject to forces exerted on it by the flowing blood (red) which are proportional to the shear stress at its location. If these forces exceed the maximal force that can be sustained by the integrin binding (blue), the leukocyte will be torn away and adhesion will not occur.

by the blood is proportional to the shear stress at the leukocyte's position, shear stress directly affects whether the cell will ultimately become tightly tethered to the vessel wall or be washed away downstream. This too then provides a mechanism for a higher initial rate of leukocyte adhesion on the lateral wall of the main branch vs. the flow divider.

The pattern of sub-acute leukocyte accumulation follows the same spatial pattern that favors the lateral wall vs. flow divider as does the pattern of early adhesion and likely the same reasons. The accumulation of these cells allows examination of the distribution in the longitudinal as well as the circumferential plane. On the lateral wall, the number of cells per high power field increases steadily towards the middle of the stent. This is in good agreement with the thickness of the separated boundary layer as shown by the bench-top models. As one moves further distally in the models, this thickness begins to diminish as do the leukocyte accumulations. The flow divider, on the other hand, exhibits very low rates of accumulation, in agreement with the region of very high shear

stress seen in the models. These rates then increase as one moves distally along the stent until they reach what are presumably 'baseline' values.
The pattern of accumulation is re-capitulated whether one looks at any individual animal, or at the normalized average values (compare fig. 6-04 and fig. 6-05). This constancy of the observed effect not just in the statistical sense, but rather in each and every individual case is not coincidental. Rather, it is an indication of the fundamental nature of this phenomenon i.e. it is so dominant that it occurs every single time and in every single animal.

Side branch occlusion clearly modulates the early pattern of leukocyte adhesion and accumulation in the main branch of the bifurcation. This is demonstrated in both the number of leukocytes present and the total neo-intimal thickness which is affected by the production of extra-cellular matrix as well (figs.6-06 &6-08). In general, side branch occlusion takes the bifurcation pattern discussed above for a side-branch-open state and reduces it to that which would be expected to occur in a non-bifurcating vessel. The total average leukocyte numbers in the side branch occluded side are substantially lower than in the side branch patent side. This difference arises entirely from the higher rates of accumulation in the lateral wall caused by the region of boundary layer separation. On the flow divider wall, the number of leukocytes in the side branch patent case is lower than on either wall of the side branch occluded case. This effect occurs because the shear stress on the flow divider in the patent side branch is not only elevated relative to its own lateral wall but also relative to 'baseline' i.e. the side branch occluded case.
The ratio of accumulation on the lateral wall vs. the flow divider in the side branch occluded case (figs.6-07 &6-09) is close to unity. This symmetry re-affirms that the behavior of the side branch occluded case is essentially that of a non-bifurcating vessel. In contrast, the large ratios of lateral wall vs. flow divider accumulations in the side branch patent are an indication of the dominance of flow pattern and flow-mediated stimuli in determining the cellular processes at the vessel wall at least at this early stage in the process.
The discrepancy in symmetry provides further evidence relating to the question of the relative contribution of the reduction in flow disturbance vs. an increase in total flow. If

the increase in total flow is dominant, one would expect the degree of asymmetry to be similar in the side branch occluded and side branch patent cases. In practice, not only is the total accumulation higher in the side branch patent case, but so is the degree of asymmetry. The difference between the two cases can be explained by the presence of (asymmetric) flow disturbance in the one as opposed to the (symmetric) total flow increase in the other. Note also that the degree of asymmetry in the side branch patent case tends to the side branch occluded case as one moves towards the distal end of the stent.

7. Conclusions

Many different approaches can be used to model the circulation, indeed most phenomena in the body. One could model the anatomy, physiology and/or pathology of the relevant tissues or organs. The approach taken here is different in that the focus was mechanistic. Rigorous control of the model configuration with an eye towards specific parametric regulation enabled us to obtain this mechanistic insight. Models that are more faithful to the anatomy, physiology or the pathology cannot provide this perspective and in our view never really approach actual physical modeling. One can understand the systems involved and the mechanisms that affect them by transcending the specific scenarios at hand, and without the limits of attempting to produce an accurate description of a biological system.

7.1. Inertance Dominated Flow

Previous work has provided some evidence to support the idea that arterial compliance plays only a secondary role in the determination of flow patterns[52]. The establishment of the flow regime presented here provides rigorous mathematical support for this view. That flow in the isolated region of the vascular bed at the level of a bifurcation was shown to be inertance dominated, had profound implications for physical and mathematical modeling of bifurcated vascular beds. Physical models can be constructed with less precise consideration of potentially complex stress-strain relationships, greatly simplifying the task of building a meaningful model. Similarly, if arterial compliance can be disregarded mathematical models can be greatly simplified. The number of free parameters is reduced. This allows for a more meaningful fit for the two free parameters that remain, resistance and inertance, and makes it possible to apply the fit obtained for these parameters to a description of the properties of flow, in particular the changes in resistance from flow separation. It is important to note that this does not mean that the compliance of the arterial wall plays no role in flow within a bifurcation. Indeed, certain phenomenon, such as the temporal distribution of flow between the two branches and the damping of the waveforms to name just two, would not exist were it not for the existence of compliance. However, to a first order approximation, the mere fact that the model is

compliant and that this compliance is within the general range of the prototype system, as observed by the approximate distension of the flow channels with each cycle, is enough to ensure that these important effects will exist in the model in the same qualitative way that they do *in-vivo*.

7.2. Mathematical Modeling

It is possible to provide a relatively simple lumped parameter mathematical model that describes the flow system very well, as was demonstrated by the excellent fit of the predicted to the measured waveforms. This model can then be applied to obtain information regarding the properties of flow within the model system. Specifically, this can be used to describe changes the resistance of the vessels. The value of the resistance carries physical significance in and of itself as it determines the workload for perfusing a tissue segment through the relevant arteries. Additionally, changes in the resistance can be used to infer changes in the flow patterns within the arteries, e.g. the extent of flow separation. In this context, we have demonstrated the ability to describe changes in the resistance of a vessel segment that arise entirely from shifts in the flow patterns, without any change in the physical properties or the geometry of the vessel itself. Since these changes are brought about by alterations of a neighboring vessel, we can then describe the interactions that exist between one site in the arterial tree and another. The interactions observed here and their effect on the resistance fit with the theoretical predictions made previously regarding the effects of geometric alterations in one vessel on another.

The ability to quantify resistive effects in this way and to accurately deduce the local variations in the patterns of flow is however limited by the manner in which differential pressure measurements are performed. Using an external differential pressure sensor results in an *a-priori* limit on the signal-to-noise ratio and hence the accuracy and reliability with which these measurements and deductions can be made. To produce more accurate results, pressure wires can be used instead of the differential pressure sensor, offering the advantage of potential insertion into the silicone segment of interest itself. By locating one pressure wire immediately proximal to the region of flow separation, and a second pressure wire immediately distal to the region of flow

separation, a measurement that only the segment of interest can be made. However, the sensitivity of the pressure wires is much lower than that which can be achieved by the differential pressure sensor. This is a direct consequence of the fact that the pressure wire is a clinical tool designed to measure pressures in the range of 80-120 mmHg. As discussed previously, the pressure drops that can be expected within the model due to subtle differences in flow separation are on the order of 0.1-0.01mmHg and are thus not picked up by the pressure wires. It should be noted however that for the *in-vivo* situation, the expected pressure drop from flow separation increases to an order of several mmHg. It is therefore likely that this same effect could be measured in the clinical setting, or if smaller models were built to investigate this technique specifically. One could argue that even a disturbance-induced pressure drop on the order of 1mmHg is insignificant relative to the drop in the distal arterial bed of approx. 40-80mmgHg. However, clinical practice shows that significant lesions with cross-sectional occlusions of 80% or more can have pressure drops of anywhere from 40 to as little as 5mmHg[56,57]. As these lesions are routinely dilated with an associated substantial improvement in symptoms, we may conclude that under certain diseased conditions, even the elimination (or addition) of a numerically small resistance can have vast clinical implications.

A further limitation of this analysis arises from the assumption of constant inertance. This assumption was required to increase the stability of the fit for the resistance. In practice however, as the flow pattern changes, so does the inertance. While these changes can be expected to be small relative to the total inertance, as discussed above, the changes in the resistance are small as well. Given these difficulties, it is impossible to give a precise quantitative value for the resistance in any one of the stages in question. Furthermore, even the relative changes in resistance from one stage to the other must be considered semi-quantitative at best. Thus, the value of this analysis is primarily as a qualitative demonstration of the fact that arterial resistance can change significantly as a result of changes in flow pattern even in the absence of geometric changes in the arterial wall.

Nonetheless, even this qualitative demonstration carries important clinical implications. One of these relates to the use of one of the most modern interventional devices – drug eluting stents (DES). The anti-hyperplastic action of DES uncouples the fluid mechanic

stimulus from the biological vascular response. Thus, large regions of boundary layer separation can exist without leading to vessel occlusion in the long term. However, the resistance to flow can change dramatically from these flow disturbances, whether the vessel wall itself changes geometry or not. In the past, these regions of disturbance would have ultimately led to development of intimal hyperplasia which would have been detectable on angiography or IVUS. Through DES, it is possible to have angiographicaly 'silent' and yet clinically significant disturbances within these stents which would lead to increased resistance and thus decreased flow. While this is not a disadvantage of DES *per-se*, it does raise several interesting questions:

a. What role does angiography play in era of DES? Have DES reduced the relevance of angiography as a clinical surrogate for flow?

b. Is it possible that some of the outstanding angiographic and/or IVUS results seen in DES trials (in particular in DES bifurcation trials) are misleading in that they do not necessarily lead to a resistance and hence perfusion benefit to the patient?

7.3. Flow Visualization

In general, the methods used here have proven to be useful in describing the expected flow phenomena within the experimental geometries. PIV and streamline analysis, in combination with the waveform analysis were complementary and capable of demonstrating subtle flow effects. In general, all cases of the experimental model demonstrated and localized regions of flow separation, regions of low and high shear, accelerations and decelerations as predicted from basic principles. The location and extent of these flow phenomena had a cyclical temporal course that was dependent upon different parts of the model geometry over the course of an entire cycle. The detailed changes in flow patterns from one case of the experiment to the other, representing either the course of progression of atherosclerotic disease, compensation by the arterial system or the effect of mechanical intervention were dealt with in chapter 3. We shall review here the general trends of major importance.

Taper in the mother vessel had a significant effect on the flow pattern. In geometries where separation in the main branch occurred, namely those with significant side branch

flow, a gradual taper in the main branch removed the region of flow separation almost entirely. This is not a surprise when one considers the fact that native arterial geometry almost always tapers at the site of significant bifurcations; the bifurcation of the left main coronary artery into the left anterior and circumflex arteries is an excellent example of this phenomena. Yet the impact of tapering on flow separation carries significant implications when considering the optimal course of intervention in clinical scenarios that include dilation of a lesion at this location.

The pattern of flow in the main branch was directly affected by alterations in the side branch alone. Gradual occlusion of the side branch reduced the region of flow separation opposite the ostium of the side branch. At high levels of side branch occlusion, non-separated flow was achieved in the main branch even without the introduction of taper. Since the removal of taper, in the absence of flow separation, physically increases the vessel diameter lowering resistance to flow, it seems reasonable that the adaptive arterial bed would develop in this direction, i.e. compensatory dilation of the distal portion of the main branch in response to occlusion of the side branch. This potential observation remains to be shown *in-vivo*. Dilation of the side branch on the other hand, re-established a significant region of separation in the main branch. In some instances, for example where significant collateral flow was present, this new region of separation can be substantially more prominent than the one that existed in the same location before occlusion of the side branch. Further analysis is required to identify other adaptive changes, e.g. alterations in downstream resistance to flow, which could affect the extent of the new region of separation in the main branch. This sort of analysis could have important clinical implications when considering the optimal approach to dilation of lesions in a side branch.

The flow in a geometry that includes a lesion in the main branch had important characteristics that were related to the geometry of the lesion present. The length of the lesion in the mother branch affected the flow separation in the daughter branch. A long lesion reduced the area of flow separation in the ostium of the daughter branch and in this sense was "protective" of side branch. Since occlusion of flow in the side branch reduced the extent of separation in the main branch, as was discussed previously, this protective aspect of a bifurcation can be seen to work bilaterally, at least in the case examined of a

branch cross-sectional ratio of 1:1. Short lesions in the mother branch which have the same geometry of the space taken up previously by the side branch induced flow separation, induced little-to-no further flow disturbances. On the other hand, a long lesion was associated with a region of flow separation that begins at the apex of the lesion and extends distally. This is consistent with the clinical observation that these lesions grow in the distal direction.

7.4. Geometric Pattern of Hyperplasia at a Bifurcation

The novel techniques described here enable good three-dimensional geometric histological description of an atherosclerotic lesion. Further work needs to be done to suit these techniques better to immunohistochemistry as well as the ability to describe complex three dimensional structures, not just tubular ones. Previous work has demonstrated correlations between flow patterns and lesion localization. We believe that these techniques enable one to go one step further in that it is now possible to begin to examine the potential correlation between flow patterns and the actual geometry of the resultant lesions.

The correlation between the regions of boundary layer separation in the models and the observed geometries of chronic *in-vivo* lesions provides validation for the utility of these models while at the same time makes several important points: First that the localization and geometry of stent restenosis is likely affected by flow disturbance in the same way as *de-novo* atherosclerotic disease. Further, that these areas of flow disturbance play a dominant role even in the presence of such confounding factors as the presence of a permanent implant. Lastly, that while the intricacies of the precise flow pattern are affected by the level of detail of the model and its similarity to the prototype vessel, the generalized, primary flow pattern is sufficient to provide significant insight into the ultimate chronic lesion.

The composition of a lesion at a bifurcation in one of these regions of boundary layer separation was shown to be complex and non-uniform. Distinct regions ('crescent' and 'annulus') could be identified within this larger lesion, differing in morphologic appearance, cellular density and extra-cellular matrix content. The differences between these regions seem to imply the presence of temporally and geometrically distinct

processes at work in the creation of the lesion. We have postulated that some of these processes might be flow-dependant while others may reflect flow-independent responses to arterial injury. A further, more detailed investigation of these different processes at higher resolution and using more advanced immunohistological techniques is warranted.

7.5. Effect of Side Branch Flow

The animal model developed for these studies allows *in-vivo* observation of the effects of flow modulation on vascular biology. The side by side comparison in each animal enables the use of internal controls to normalize for the many confounding factors associated with individual animal biological response. In this set of experiments, we have concentrated on the biological end-point of development of neo-intimal hyperplasia in response to vascular stenting. The ability to use this very same model to test the *in-vivo* effect of flow modulation on other biological markers such as endothelial dysfunction, surface adhesion molecule production, gene expression, etc. has not escaped us.

Side branch patency was shown to have a profound effect on main branch neo-intimal hyperplasia both by qualitative analysis and when measured as neo-intimal area, intima to media ratio or luminal area. This effect was consistent with the predictions based on the flow model. Far from trivial, this correlation between bench top model and animal had important implications in that the general, qualitative pattern held true not just in the composite and statistical sense but rather when examined in each individual animal.

The experiments were designed in such a way as to effectively rule out two possible trivial explanations for the observed difference – that based on an excess of arterial injury in a bifurcation and that based on total flow rather than boundary layer separation. Thus, we can say with a high degree of certainty that it is indeed the dilation (or lack of occlusion in this case) of the side branch that introduces a region of boundary layer separation into an otherwise disturbance-free main branch. This region of separation then leads as was demonstrated in the model validation and the chronic *in-vivo* experiments to the deterministic development of a restenotic lesion of specific geometry.

The inability to precisely quantify *in-vivo* flow prevented a more quantitative investigation of the nature of this interaction. For example, the degree of side branch

flow reduction and its correlation to the effect on main branch neo-intimal hyperplasia is an important parameter of clinical applicability. In the future, when more precise flow measurement is available one could ask whether side branch total occlusion/dilation is necessary for the observed protective/detrimental effect to occur.

Remodeling was shown to play an important role in the effects observed. The same experiment preformed with or without allowing the time for remodeling to occur produced vastly different results, in good agreement with the hypothetical and bench top model predictions. We have proposed at least one type of remodeling that might occur and would explain the observed effect – main branch outward remodeling in response to increased shear stress as a result of side branch occlusion. While certainly providing evidence for the feasibility of our remodeling-based hypothesis, this study does not provide direct proof that this indeed occurs, nor does it rule out other forms of remodeling that could take place over the same period of time. Further study, using high resolution intra-vascular ultrasound for example, may very well demonstrate and perhaps even quantify the extent to which main branch remodeling occurs.

7.6. Acute Response

The acute response as demonstrated in the animals sacrificed at 72 hours provides a mechanistic link between the flow patterns demonstrated in the flow models and the chronic tissue response demonstrated in the animal model. The data presented here indicate that the effect of flow pattern modulation is mediated by the action of leukocytes. Leukocyte adhesion, followed by accumulation was directly affected by modulation of the flow pattern in a predictable manner. Previous work has shown that monocyte number is the most powerful predictor of final intimal area[58]. Thus, the increase in intimal area observed late is very likely a result of the increase in accumulation early.

We have suggested several different mechanisms by which this differential accumulation of leukocytes could occur including higher rates of passive particle accumulations, lower opposing forces and primary endothelial cell dysfunction. The relative contribution of each one of these factors has not been investigated here. Detailed immunohistological analysis, time course studies and possibly even genetic sampling could all be used to

decipher which of these factors is working at any point in time. The precise mechanism by which this localization occurs is critical to the development of pharmacologic approaches aimed at alleviating this phenomenon.

7.7. Clinical Implications

Though the bifurcation is a preferred site for the generation of atherosclerotic diseases, lesions in this site are difficult to discern and to intervene upon. The clinical literature is now replete with investigations questioning whether bifurcation lesions should be treated[59-61], and the possible technologies[62-65], strategies[66-77] and long-term effects[73,75-81] of different treatment options. Despite an increase in such interventions, comparative studies have shown little or no long-term benefit to stenting of both branches of a bifurcation in place of stenting of the main branch (MB) alone and angioplasty of the side branch (SB)[80,82,83]. These results raise the question: If stenting is generally superior to angioplasty why is stenting of both vessels not always superior to stenting of one segment alone?

An inherent difficulty in treating bifurcations is the uncertainty regarding which acute interventional result will ensure an optimal effect in the long term. Even if the optimal acute geometric result is obtained there is no proof, moreover any reason to believe that it would ensure the optimal chronic result that is more relevant to patient care. It has been suggested that the complexity of the bifurcation lesion predisposes to a sub-optimal geometric result[73], or that in obtaining an optimal result a larger amount of mechanical injury must be imposed. We believe that both of these explanations are technical difficulties that will eventually be overcome. Furthermore, we have controlled for these types of considerations in both our bench top and our *in-vivo* experiments thus demonstrating that resolution of these technical difficulties would not address the fundamental underlying problem.

The data presented here suggest that atherosclerotic lesions in bifurcated arterial segments cannot be considered simply as independent side-by-side arterial obstructions. Occlusion of a SB is protective of the MB by greatly reducing the extent of boundary layer separation opposite the ostium. Conversely, the re-introduction of flow into the SB has a deleterious effect on the flow conditions within the MB. It is worthwhile noting

that this reintroduced flow instability is qualitatively different from the flow separation that was observed with the initial lesion in that the arterial system is now perturbed over a time course several orders of magnitude shorter than the original slow progression of atherosclerotic disease. Under these conditions, it is not surprising that the compensatory mechanisms involved would function far from optimally.

It is felt that these factors should be taken into account when considering the optimal course of action in treating a bifurcation lesion. The potential benefit in perfusion of dilating both branches on the one hand, should be weighed against the increased risk of re-occlusion of the MB on the other. This potential risk is exacerbated by the fact that often times the MB is larger and perfuses a greater amount of distal tissue and is thus functionally significantly more important than the SB. Hence, keeping the MB patent in the long term might outweigh the transient benefit of having both branches dilated.

It should be noted that this study has concentrated on the bifurcation in the narrow sense i.e. occlusion of side branches immediately distal to the bifurcation itself. Preliminary data from the bench top models however, indicate that the effect on the main branch is not mediated by precise side branch geometry but rather by total side branch flow. Further studies are needed to demonstrate this for more configurations. If, however, this observation holds true for a large variety of bifurcations and especially if partial occlusion followed by dilation is sufficient to effect adverse changes in the main branch, then one must assume that the implications of this work would extend beyond just the immediate bifurcation. As an example, this work could be applied to the effect that dilating the proximal first diagonal coronary branch would have on the LAD in the narrow sense, but would also apply to the effect that dilating the mid circumflex would have on the left main bifurcation in the broader sense.

This concept brings us back to the basic premise of this work – interactions at a distance between different sites in the arterial tree. The immediate bifurcation was used here as a simple model to demonstrate that these interactions could exist and to demonstrate the potential for clinically relevant consequences. Having done so, we believe that this concept can be extended to other arterial geometries. The current clinical mindset which focuses on individual lesions and arteries as independent entities needs to be developed into a more global approach. A more realistic understanding of the interplay between

different sites in the arterial tree and the implications of intervening in one site on another needs to be developed. It is particularly crucial to identify those situations whereby local and global optimizations are at odds with each other. Through this knowledge, one can begin to develop global strategies for optimization of blood flow to entire arterial beds.

8. References

1. Texon, M. A Hemodynamic Concept of Atherosclerosis, with Particular Reference to Coronary Occlusion. *A.M.A. Archives of Internal Medicine* **99**, 418-427 (1957).
2. Roach, M. R. The effects of bifurcations and stenoses on arterial disease. pp. 489-539. *In: Hwang NH, Normann NA, ed. Cardiovascular flow dynamics and measurements. Baltimore, Univ Park Press,* (1977).
3. Giddens, D. P., Zarins, C. K. & Glagov, S. The role of fluid mechanics in the localization and detection of atherosclerosis. *J Biomech Eng* **115**, 588-94 (1993).
4. Krams, R. et al. Evaluation of endothelial shear stress and 3D geometry as factors determining the development of atherosclerosis and remodeling in human coronary arteries in vivo. Combining 3D reconstruction from angiography and IVUS (ANGUS) with computational fluid dynamics. *Arterioscler Thromb Vasc Biol* **17**, 2061-5 (1997).
5. Caro, C. G., Fitz-Gerald, J. M. & Schroter, R. C. Arterial wall shear and distribution of early atheroma in man. *Nature* **223**, 1159-60 (1969).
6. Friedman, M. H., Bargeron, C. B., Deters, O. J., Hutchins, G. M. & Mark, F. F. Correlation between wall shear and intimal thickness at a coronary artery branch. *Atherosclerosis* **68**, 27-33 (1987).
7. Sabbah, H. N. et al. Relation of atherosclerosis to arterial wall shear in the left anterior descending coronary artery of man. *Am Heart J* **112**, 453-8 (1986).
8. Nagel, T., Resnick, N., Dewey, C. F., Jr. & Gimbrone, M. A., Jr. Vascular endothelial cells respond to spatial gradients in fluid shear stress by enhanced activation of transcription factors. *Arterioscler Thromb Vasc Biol* **19**, 1825-34 (1999).
9. Fry, D. L. Acute vascular endothelial changes associated with increased blood velocity gradients. *Circ Res* **22**, 165-97 (1968).
10. Davies, P. F. Multiple signaling pathways in flow-mediated endothelial mechanotransduction: PYK-ing the right location. *Arterioscler Thromb Vasc Biol* **22**, 1755-7 (2002).
11. Davies, P. F. Flow-mediated endothelial mechanotransduction. *Physiol Rev* **75**, 519-60 (1995).
12. Dull, R. O., Tarbell, J. M. & Davies, P. F. Mechanisms of flow-mediated signal transduction in endothelial cells: kinetics of ATP surface concentrations. *J Vasc Res* **29**, 410-9 (1992).
13. Davies, P. F., Remuzzi, A., Gordon, E. J., Dewey, C. F., Jr. & Gimbrone, M. A., Jr. Turbulent fluid shear stress induces vascular endothelial cell turnover in vitro. *Proc Natl Acad Sci U S A* **83**, 2114-7 (1986).
14. Fergusson, G. G. & Roach, M. R. in *Carsiovascular Fluid Dynamics.* (ed. Bergel, D. H.) 141-157 (Academic Press Inc., Orlando., 1976).

15. Gutstein, W. H., Farrell, G. A. & Armellini, C. Blood flow disturbance and endothelial cell injury in preatherosclerotic swine. *Lab Invest* **29**, 134-49 (1973).
16. Glagov, S., Zarins, C., Giddens, D. P. & Ku, D. N. Hemodynamics and atherosclerosis. Insights and perspectives gained from studies of human arteries. *Arch Pathol Lab Med* **112**, 1018-31 (1988).
17. Friedman, M. H., Deters, O. J., Bargeron, C. B., Hutchins, G. M. & Mark, F. F. Shear-dependent thickening of the human arterial intima. *Atherosclerosis* **60**, 161-71 (1986).
18. Sabbah, H. N., Khaja, F., Brymer, J. F., Hawkins, E. T. & Stein, P. D. Blood velocity in the right coronary artery: relation to the distribution of atherosclerotic lesions. *Am J Cardiol* **53**, 1008-12 (1984).
19. Gibson, C. M. et al. Relation of vessel wall shear stress to atherosclerosis progression in human coronary arteries. *Arterioscler Thromb* **13**, 310-5 (1993).
20. Davies, P. F. Mechanisms involved in endothelial responses to hemodynamic forces. *Atherosclerosis* **131 Suppl**, S15-7 (1997).
21. DePaola, N., Gimbrone, M. A., Jr., Davies, P. F. & Dewey, C. F., Jr. Vascular endothelium responds to fluid shear stress gradients [published erratum appears in Arterioscler Thromb 1993 Mar;13(3):465]. *Arterioscler Thromb* **12**, 1254-7 (1992).
22. Fernandez, R. C., De Witt, K. J. & Botwin, M. R. Pulsatile flow through a bifurcation with applications to arterial disease. *J Biomech* **9**, 575-80 (1976).
23. Fox, J. A. & Hugh, A. E. Localization of atheroma: a theory based on boundary layer separation. *Br Heart J* **28**, 388-99 (1966).
24. Moore, J. E., Jr., Xu, C., Glagov, S., Zarins, C. K. & Ku, D. N. Fluid wall shear stress measurements in a model of the human abdominal aorta: oscillatory behavior and relationship to atherosclerosis. *Atherosclerosis* **110**, 225-40 (1994).
25. Ross, R. Atherosclerosis is an inflammatory disease. *Am Heart J* **138**, S419-20 (1999).
26. Pritchard, W. F. et al. Effects of wall shear stress and fluid recirculation on the localization of circulating monocytes in a three-dimensional flow model. *J Biomech* **28**, 1459-69 (1995).
27. Fry, D. L. in *Atherogenesis: Initiating Factors* 93-121 (Assosciated Science Publishers, 1973).
28. Asakura, T. & Karino, T. Flow patterns and spatial distribution of atherosclerotic lesions in human coronary arteries. *Circ Res* **66**, 1045-66 (1990).
29. Pedley, T. J. High Reynolds number flow in tubes of complex geometry with application to wall shear stress in arteries. *Symp Soc Exp Biol* **49**, 219-41 (1995).
30. Perktold, K. et al. Validated computation of physiologic flow in a realistic coronary artery branch. *J Biomech* **31**, 217-28 (1998).

31. Zamir, M. & Roach, M. R. Blood flow downstream of a two-dimensional bifurcation. *J Theor Biol* **42**, 33-48 (1973).
32. He, X. & Ku, D. N. Pulsatile flow in the human left coronary artery bifurcation: average conditions. *J Biomech Eng* **118**, 74-82 (1996).
33. Rindt, C. C. & Steenhoven, A. A. Unsteady flow in a rigid 3-D model of the carotid artery bifurcation. *J Biomech Eng* **118**, 90-6 (1996).
34. He, X., Ku, D. N. & Moore, J. E., Jr. Simple calculation of the velocity profiles for pulsatile flow in a blood vessel using Mathematica [published erratum appears in Ann Biomed Eng 1993 Sep-Oct;21(5):557-8]. *Ann Biomed Eng* **21**, 45-9 (1993).
35. Malcolm, A. D. (University of Western Ontario, 1975).
36. Friedman, M. H., Kuban, B. D., Schmalbrock, P., Smith, K. & Altan, T. Fabrication of vascular replicas from magnetic resonance images. *J Biomech Eng* **117**, 364-6 (1995).
37. Bharadvaj, B. K., Mabon, R. F. & Giddens, D. P. Steady flow in a model of the human carotid bifurcation. Part I--flow visualization. *J Biomech* **15**, 349-62 (1982).
38. Kuban, B. D. & Friedman, M. H. The effect of pulsatile frequency on wall shear in a compliant cast of a human aortic bifurcation. *J Biomech Eng* **117**, 219-23 (1995).
39. Yoganathan, A. P. et al. Steady flow velocity measurements in a pulmonary artery model with varying degrees of pulmonic stenosis. *J Biomech* **19**, 129-46 (1986).
40. Moore, J. E., Jr. et al. Preliminary analysis of the effects of blood vessel movement on blood flow patterns in the coronary arteries. *J Biomech Eng* **116**, 302-6 (1994).
41. Brownlee, R. D. & Langille, B. L. Arterial adaptations to altered blood flow. *Can J Physiol Pharmacol* **69**, 978-83 (1991).
42. Schlichting, H. *Boundary - Layer Theory* (ed. Vesper, K. H.) (McGraw - Hill, 1968).
43. Langille, B. L. Arterial remodeling: relation to hemodynamics. *Can J Physiol Pharmacol* **74**, 834-41 (1996).
44. Di Mario, C., Kern, M. J. & Serruys, P. W. in *Textbook of Interventional Cardiology* (ed. Topol, E. J.) (W.B. Saunders, Philadelphia, 1994).
45. Di Mario, C. et al. Limitations of the zero crossing detector in the analysis of intracoronary Doppler: a comparison with fast Fourier transform analysis of basal, hyperemic, and transstenotic blood flow velocity measurements in patients with coronary artery disease. *Cathet Cardiovasc Diagn* **28**, 56-64 (1993).
46. Wells, M. K., Winter, D. C., Nelson, A. W. & McCarthy, T. C. Blood Velocity Patterns in Coronary Arteries. *Journal of Biomechanical Engineering*, 26-31 (1977).
47. Di Mario, C. et al. Maximal blood flow velocity in severe coronary stenoses measured with a Doppler guidewire. Limitations for the application of the continuity equation in the assessment of stenosis severity. *Am J Cardiol* **71**, 54D-61D (1993).

48. Rieu, R., Friggi, A. & Pelissier, R. Velocity distribution along an elastic model of human arterial tree. *J Biomech* **18**, 703-15 (1985).
49. Sabbah, H. N., Hawkins, E. T. & Stein, P. D. Flow separation in the renal arteries. *Arteriosclerosis* **4**, 28-33 (1984).
50. Fung, Y. C. in *Biodynamics. Circulation.* 100-104 (Springer-Verlang, New York, 1984).
51. Wood, N. B. Aspects of fluid dynamics applied to the larger arteries. *J Theor Biol* **199**, 137-61 (1999).
52. Friedman, M. H., Bargeron, C. B., Duncan, D. D., Hutchins, G. M. & Mark, F. F. Effects of arterial compliance and non-Newtonian rheology on correlations between intimal thickness and wall shear. *J Biomech Eng* **114**, 317-20 (1992).
53. Hart, D. P. Super-Resolution PIV by Recursive Local-Correlation. *Journal of Visualization* **10** (1999).
54. Ward, M. R. et al. Low blood flow after angioplasty augments mechanisms of restenosis: inward vessel remodeling, cell migration, and activity of genes regulating migration. *Arterioscler Thromb Vasc Biol* **21**, 208-13 (2001).
55. Wentzel, J. J. et al. Relationship between neointimal thickness and shear stress after Wallstent implantation in human coronary arteries. *Circulation* **103**, 1740-5. (2001).
56. Di Mario, C. et al. Intracoronary blood flow velocity and transstenotic pressure gradient using sensor-tip pressure and Doppler guidewires: a new technology for the assessment of stenosis severity in the catheterization laboratory. *Cathet Cardiovasc Diagn* **28**, 311-9 (1993).
57. Serruys, P. W. et al. Intracoronary pressure and flow velocity with sensor-tip guidewires: a new methodologic approach for assessment of coronary hemodynamics before and after coronary interventions. *Am J Cardiol* **71**, 41D-53D (1993).
58. Rogers, C., Welt, F. G., Karnovsky, M. J. & Edelman, E. R. Monocyte recruitment and neointimal hyperplasia in rabbits. Coupled inhibitory effects of heparin. *Arterioscler Thromb Vasc Biol* **16**, 1312-8 (1996).
59. Baim, D. Is Bifurcation Stenting the Answer? *Catheterization and Cardiovascular Diagnosis*, 314-316 (1996).
60. Oesterle, S. N. Coronary interventions at a crossroads: the bifurcation stenosis [editorial; comment]. *J Am Coll Cardiol* **32**, 1853-4 (1998).
61. Satler, L. F., Mintz, G. S., Pichard, A. D. & Kont, K. M. Bifurcation disease: to treat or not to treat [comment] [editorial]. *Catheter Cardiovasc Interv* **50**, 411-2 (2000).
62. Carlier, S. G. et al. Stenting with a true bifurcated stent: acute and mid-term follow-up results. *Catheter Cardiovasc Interv* **47**, 361-96 (1999).
63. Dauerman, H. L. et al. Mechanical debulking versus balloon angioplasty for the treatment of true bifurcation lesions. *J Am Coll Cardiol* **32**, 1845-52 (1998).
64. Cho, G. Y. et al. Effects of stent design on side branch occlusion after coronary stent placement. *Catheter Cardiovasc Interv* **52**, 18-23 (2001).

65. Cervinka, P. et al. Coronary bifurcation stenting using dedicated bifurcation stents. *Catheter Cardiovasc Interv* **49**, 105-11 (2000).
66. Chevalier, B., Glatt, B., Royer, T. & Guyon, P. Placement of coronary stents in bifurcation lesions by the "culotte" technique. *Am J Cardiol* **82**, 943-9 (1998).
67. Carrie, D. et al. Coronary stenting of bifurcation lesions using "T" or "reverse Y" configuration with Wiktor stent. *Am J Cardiol* **82**, 1418-21, A8 (1998).
68. Ho, D. S., Chen, W. H. & Woo, C. Stenting of a renal artery bifurcation stenosis. *Cathet Cardiovasc Diagn* **45**, 445-9 (1998).
69. Pan, M. et al. Simple and complex stent strategies for bifurcated coronary arterial stenosis involving the side branch origin. *Am J Cardiol* **83**, 1320-5 (1999).
70. Pan, M. et al. A stepwise strategy for the stent treatment of bifurcated coronary lesions. *Catheter Cardiovasc Interv* **55**, 50-7 (2002).
71. Carrie, D., Karouny, E., Chouairi, S. & Puel, J. "T"-shaped stent placement: a technique for the treatment of dissected bifurcation lesions. *Cathet Cardiovasc Diagn* **37**, 311-3 (1996).
72. Kobayashi, Y. et al. Modified "T" stenting: a technique for kissing stents in bifurcational coronary lesion. *Cathet Cardiovasc Diagn* **43**, 323-6 (1998).
73. Lefevre, T. et al. Stenting of bifurcation lesions: classification, treatments, and results [see comments]. *Catheter Cardiovasc Interv* **49**, 274-83 (2000).
74. Cohen, D. J. & Baim, D. S. Considerations in managing side branches "jailed" by coronary stenting: insights from in vitro studies [editorial; comment]. *Catheter Cardiovasc Interv* **48**, 235-6 (1999).
75. Aliabadi, D. et al. Incidence and angiographic predictors of side branch occlusion following high-pressure intracoronary stenting. *Am J Cardiol* **80**, 994-7 (1997).
76. Brueck, M., Scheinert, D., Flachskampf, F. A., Daniel, W. G. & Ludwig, J. Sequential vs. kissing balloon angioplasty for stenting of bifurcation coronary lesions. *Catheter Cardiovasc Interv* **55**, 461-6 (2002).
77. Karvouni, E. et al. Directional atherectomy prior to stenting in bifurcation lesions: a matched comparison study with stenting alone. *Catheter Cardiovasc Interv* **53**, 12-20 (2001).
78. Sheiban, I. et al. Immediate and long-term results of "T" stenting for bifurcation coronary lesions. *Am J Cardiol* **85**, 1141-4, A9 (2000).
79. Fischman, D. L. et al. Fate of lesion-related side branches after coronary artery stenting. *J Am Coll Cardiol* **22**, 1641-6 (1993).
80. Al Suwaidi, J. et al. Immediate and long-term outcome of intracoronary stent implantation for true bifurcation lesions. *J Am Coll Cardiol* **35**, 929-36 (2000).
81. Al Suwaidi, J. et al. Immediate and one-year outcome in patients with coronary bifurcation lesions in the modern era (NHLBI dynamic registry). *Am J Cardiol* **87**, 1139-44 (2001).

82. Yamashita, T. et al. Bifurcation lesions: two stents versus one stent--immediate and follow-up results. *J Am Coll Cardiol* **35**, 1145-51 (2000).
83. Bhargava, B. et al. Clinical outcomes of compromised side branch (stent jail) after coronary stenting with the NIR stent. *Catheter Cardiovasc Interv* **54**, 295-300 (2001).

Appendix A: Design and Operation of Sensors

Differential pressure sensor:

1. Parts:
   1.1. Motorola MPX10DP – Differential pressure sensor.
   1.2. 324 Quad Op-Amp chip.
   1.3. Analog devices AD624BD – Instrumentation amplifier.
2. See circuit diagram on next page.
3. Gain settings:

Gain	100						200						500						1000					
Dipswitch	1	2	3	4	5	6	1	2	3	4	5	6	1	2	3	4	5	6	1	2	3	4	5	6
On		x				x			x			x				x		x		x		x	x	x
Off	x		x	x	x		x	x		x	x		x	x	x		x		x		x			

4. Zero adjustment:
   4.1. Coarse: using 1K potentiometer on –15V source.
   4.2. Fine: using 10K potentiometer on 624.
5. External terminals:
   5.1. Blue: Ground
   5.2. Green: +15
   5.3. Yellow: -15
   5.4. Red: +5
   5.5. Orange: V_{out}
   5.6. Brown: Output common (can be grounded).

Amplification circuit for differential pressure sensor:

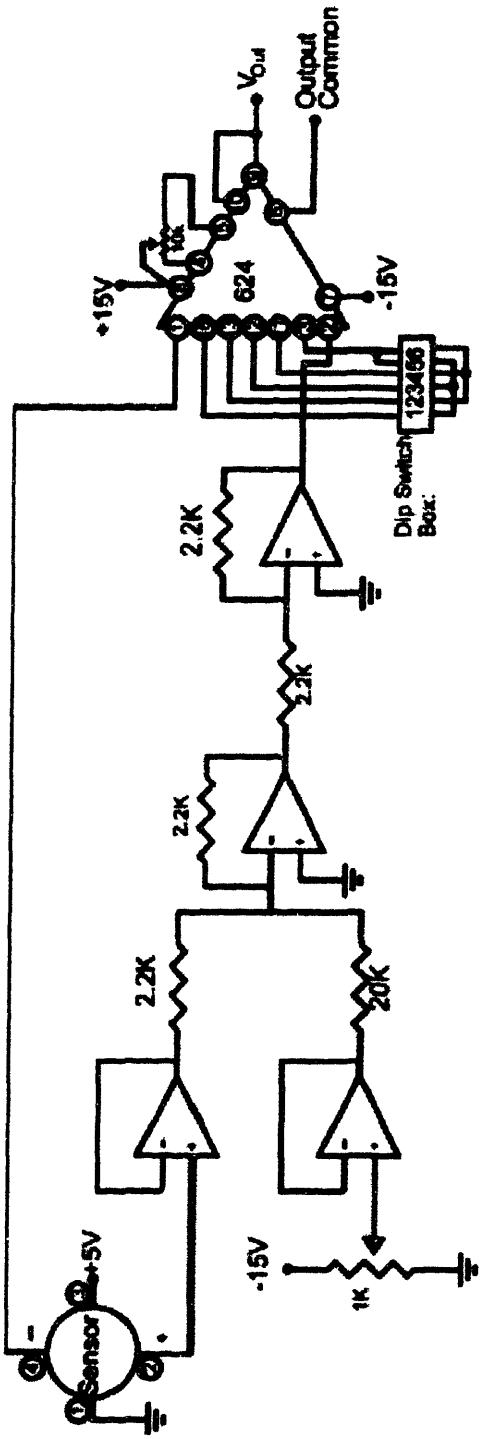

Amplification circuit for pressure wire:

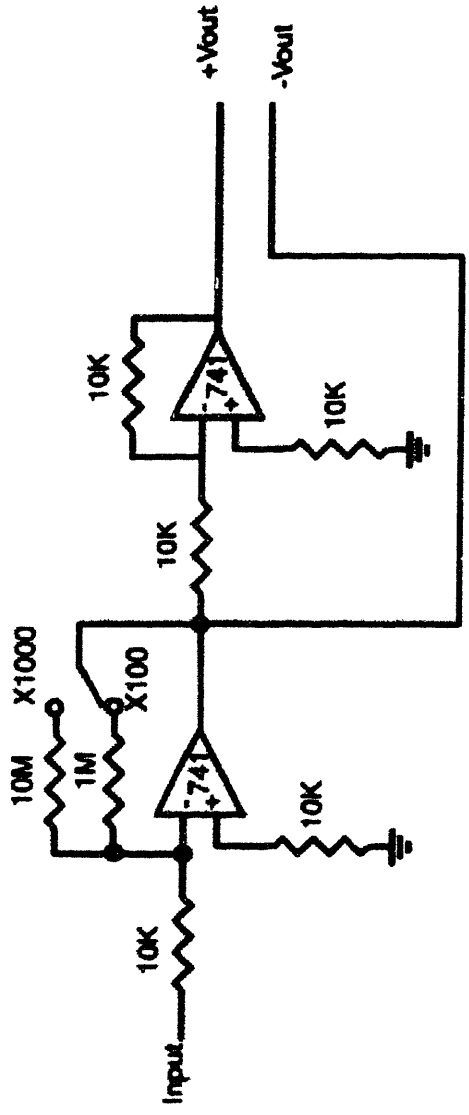

Appendix B: Code

All data analysis was performed using MATLAB V.5.3 by Math Works. The code for the few non-trivial operations is given below:

Filtering of waveforms

Use:

This was performed for low-pass filtering of pressure or flow waveforms. The filter order used throughout this thesis was 512, the cutoff frequency was for the most part 1Hz or 2Hz. which allows at least the first 10 or 20 harmonics of the fundamental frequency of the pump to pass unfiltered.

Code:

```
myfilter = fir1(filter_order,cutoff_frequency*2/sampling_frequency);
filtered_signal = filtfilt(myfilter,1,unfiltered_signal);
```

Difference function for inertance and resistance

Use:

This function takes as inputs a value for the inertance and resistance as well as the flow and differential pressure waveforms. The function calculates the predicted differential pressure waveform based on the theoretical model and the measured flow waveform. The output is the integral of the absolute value of the difference between the predicted and measured differential pressure waveforms.

Code:

```
function z=difference(LR,dpressure,flow)
L=LR(1);
R=LR(2);
Factor=1;
derived_wave=filter([R+L -L],(1/Factor),flow);
temp=derived_wave(80:length(derived_wave));
temp(length(temp)+1:length(derived_wave))=derived_wave(length(temp)+1:l
ength(derived_wave));
derived_wave=temp;
difference_wave=abs(derived_wave-dpressure);
z=sum(difference_wave);
```

Difference function for resistance

Use:

This function is similar to the one above. It differs only in that it assumes a known value for the inertance.

Code:

```
function z=difference_R(R,L,dpressure,flow)
Factor=1;
derived_wave=filter([R+L -L],(1/Factor),flow);
temp=derived_wave(80:length(derived_wave));
temp(length(temp)+1:length(derived_wave))=derived_wave(length(temp)+1:l
ength(derived_wave));
derived_wave=temp;
difference_wave=abs(derived_wave-dpressure);
z=sum(difference_wave);
```

Optimization function for resistance

Use:

The function uses the Nelder-Mead simplex algorithm to find the optimal value of the resistance. Optimum is determined as that which minimizes the above given difference function for resistance based on an arbitrary inertance value.

Code:

```
R=fmins('difference_R',R0,foptions,[],L0,pressure_wave,flow wave)
```

Prediction function

Use:

This function uses the resistance generated by the optimization function, the inertance value and the measured flow waveform to generate a predicted pressure waveform according to the theoretical model.

Code:

```
predicted_dP=filter([R+L0 -L0],1,flow_waveform);
```

THESIS PROCESSING SLIP

FIXED FIELD: ill. _____ name _____

index _____ biblio _____

▶ **COPIES:** (Archives) Aero Dewey Barker Hum

Lindgren Music Rotch Science (Sche-Plough

TITLE VARIES: ▶ ☐ _____

_____

_____

NAME VARIES: ▶ ☐ _____

_____

IMPRINT: **(COPYRIGHT)** _____

_____

▶ **COLLATION:** _____

_____

▶ **ADD: DEGREE:** _____ ▶ **DEPT.:** _____

▶ **ADD: DEGREE:** _____ ▶ **DEPT.:** _____

SUPERVISORS: _____

_____

NOTES:

fiche to Science

cat'r: date:

page: ▶ J43

▶ **DEPT:** IIST

▶ **YEAR:** 2003 ▶ **DEGREE:** Ph.D.

▶ **NAME:** RICHTER, Yoram

_____